Numerical study on the hydrodynamic background in coastal aquaculture dominated regions and corresponding interactions in the Yellow Sea

Fan Lin

Thesis for the degree of Philosophiae Doctor (PhD)
University of Bergen, Norway
2022

UNIVERSITY OF BERGEN

Numerical study on the hydrodynamic background in coastal aquaculture dominated regions and corresponding interactions in the Yellow Sea

Fan Lin

Thesis for the degree of Philosophiae Doctor (PhD)
at the University of Bergen

Date of defense: 07.01.2022

Year: 2022

Title: Numerical study on the hydrodynamic background in coastal aquaculture dominated regions and corresponding interactions in the Yellow Sea

Name: Fan Lin

Print: Skipnes Kommunikasjon / University of Bergen

Table of Contents

Scientific environment

Institute of Marine Research, Norway

Yellow Sea Fisheries Research Institute, Chinese Academy of Fishery Science, China

Tianjin University, China

The Research Council of Norway

Acknowledgements

First, I want to thank the Institute of Marine Research (IMR) and Geophysical Institute for granting me the opportunity to pursue this Ph.D. Furthermore, I also want to thank the Yellow Sea Fisheries Research Institute (YSFRI) for providing the funding and support for this scientific project.

Appreciation to my supervisors for their professional suggestions, optimistic guidance, and positive feedbacks, respectively. A special thanks to my principal supervisor, Lars Asplin, your positive attitude towards life and expertise is the robust backing that supports me in going this far in this project. Thanks to prof. Knut Barthel and prof. Hao Wei with their encouragement in both academics and administration. I also want to thank Øivind Strand at IMR, and prof. Jianguang Fang from YSFRI, who grant me the chance to work in the field of aquaculture related physical oceanography. Also, I would like to express my gratitude for the Environmental and Aquaculture Governance (EAG) project, which is granted from the Norwegian Embassy in China, for the support during this project.

I am also highly grateful for all my colleagues at both YSFRI and IMR. Thanks to Dr. Zengjie Jiang and Dr. Yuze Mao for their support during this slightly off-topic research in a fishery research institute; to Dr. Jinghui Fang, Dr. Weiwei Jiang for their fantastic work in the physiological studies; and to Dr. Xueliang Nan, who contributes a lot in our cruise on the wavy Yellow Sea; and to all my great friends at the Oceanography& Climate group at IMR, for their enthusiasm during my stay at Bergen.

Thanks to my parents for their tolerance and support at no conditions. I owe my biggest thanks to my wife, Siqi, for your support and dedication to our family. To put up with my bad tempers and give the warmest encouragement when I am down, so that I can go this far. I am looking forward hug the following adventures accompanied by you for the rest of my life.

Abstract

The Yellow Sea is an important region for aquaculture in China as the main production area for shellfish and seaweed. The aquaculture organisms sometimes can be the major group in a local ecosystem. e.g., in the Sanggou bay where about 84,500 tonnes of kelp (dry weight) and 100,000 tonnes of shellfish (wet weight) are produced annually from a surface area of ~144 km^2 (Zhang et al., 2009; Mao et al., 2018). To maintain the development of the aquaculture industry at such scales and to minimize the negative impact on the natural ecosystem, the knowledge of the biological processes at different scales is necessary for decision-makers in the formulation of policy and management strategies. However, a comprehensive description of the biogeochemical process in the aquaculture-affected regions can be highly complicated. Observations are often limited in time and space to fully describe the environmental variations in the aquaculture areas. Numerical models are capable of resolving the ecosystem processes at an often sufficient spatial and temporal scale, but with an increasing complexity from current models describing the physical environment to ecosystem models trying to describe complicated and often less known processes.

In this thesis, we have implemented a hydrodynamic model based on the Regional Ocean Modelling system (ROMS) to provide the background physical information for aquaculture related applications, the Yellow Sea Model. We have collected various observations to validate the model, and the results do reproduce reasonably well the ambient environment in aquaculture areas. The tide is the dominating current component in the Yellow Sea, moving the water back and forth continuously. The tide also provides energy on the shallow shelves creating usually well mixed water masses. In the summer, a tidal mixing front is established around the 20-50 m isobaths bordering on the Yellow Sea bottom cold water mass below the seasonal thermocline in the central Yellow Sea. An associated frontal jet flows along the tidal mixed front, transporting water masses along the shelf breaks. The tidal current also make the tidal mixing front oscillate laterally creating temporal temperature variations in the farm regions of bottom cultured scallops. The assessment index derived from these temperature oscillations is correlated to a massive scallop mortality found in the past years.

Our model results are also applied to study the baroclinic tides in the northern Yellow Sea, with a semi-diurnal internal tide being present in the stratified waters in the tidal mixing front region. The baroclinic flow associated with this internal tide contributes to enhance the total current in the bottom layer, thus potentially being important for material transportation to farmed scallops. The baroclinic signals are mostly coherent with the barotropic tides, indicating a local generation and a rapid dissipation.

Finally, we have established an ecosystem model for the integrated culture of Pacific oyster *Crassostrea gigas* and kelp *Saccharina japonica* in Sanggou bay based on a box model concept. The growth of oysters and kelp is simulated at the individual level based on the dynamic energy budget theory. The hydrodynamic information is included as forcing data to compute volume transportation and nutrient exchange. The model is validated with individual growth data recorded in the aquaculture field and water quality data for nutrients from cruises and mooring devices. The model results show that the intensive aquaculture of these low-trophic species is dominant in the local ecosystem and dramatically impacts the phytoplankton population and nutrient flux. The bay acts as a nitrogen sink during the rapid growth stage of kelp from early spring until the harvest in May. The model enables a stocking density adjustment of the culture organisms, thus providing a tool to predict the dynamic process under different scenarios. The model results support that the actual aquaculture stock density, with 50 oyster ind./m^2 and 4 kelp ind./m^2, is a balanced choice of production and cost based on decades of practical experience.

List of Publications

Fan Lin, Lars Asplin, Paul Budgell, Hao Wei, Jianguang Fang (2019): "Currents on the Northern Shelf of the Yellow Sea", *Regional Studies in Marine Science,* 32, 100821. https://dx.doi.org/10.1016/j.rsma.2019.100821

Fan Lin, Lars Asplin, Hao Wei: "Summertime M_2 Internal Tide in the Northern Yellow Sea". *Frontiers in Marine Science, (accepted)*

Asplin L., *Lin F*, Budgell WP, Strand Ø (2021): "Rapid temperature variations of the water at the Northern Shelf of the Yellow Sea and implications for sea ranching", *Aquaculture Environment Interaction*, 13: 111-119. https://doi.org/10.3354/aei00394

Lin, F., Du, M., Liu, H., Fang, J., Asplin, L., Jiang, Z. (2020): "A physical-biological coupled ecosystem model for integrated aquaculture of bivalve and seaweed in Sanggou Bay", *Ecological Modelling, 431, 109181.* https://dx.doi.org/10.1016/j.ecolmodel.2020.109181

1 Introduction

General Background

As reported by "The State of World Fisheries and Aquaculture 2020", the world aquaculture production attained another record high of 114.5 million tonnes (live weight) in 2018, with a total sale value of $263.6 billion. China is the leading global aquaculture producer, with 47.6 million tonnes of cultured animals (60.3% of global total) and 18.6 million tonnes of cultivated aquatic plants (57% of global total) in 2018 (Figure 1). Although the growth rate of the culture production started to slow down in 2017, China has maintained the position of the world's largest producer since 2001 (FAO. 2020).

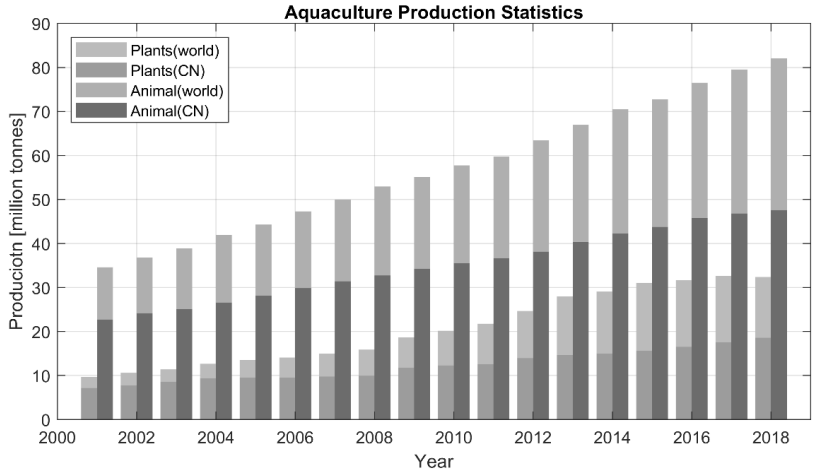

Figure 1 The aquaculture production for animals and aquatic plants from China and at a global view. Data from FAO Fishery Yearbook (2012, 2020).

If we focus on the marine aquaculture production (20 million tonnes) in China in 2018, about 71% of the production is filter-feeding bivalves and about 11% is seaweed. The top three cultured bivalves are oysters, clams, and scallops, and more than half of them are harvested from the Yellow Sea and the Bohai Sea (Figure 2). Besides the bivalves, the total mariculture production around the Yellow Sea and Bohai Sea (from Tianjin, Hebei, Liaoning, and Shandong provinces) summed up to about 9 million tonnes, which is about 44% of the domestic mariculture production in 2018.

Figure 2 Top three cultured shellfish in China, the summed production (fresh weight) of oyster (5 million tonnes), clam (4 million tonnes), and scallop (2 million tonnes) accounted for 77% of the total mariculture shellfish production (14.4 million tonnes) in 2018. Data from the <China Fishery Statistical Yearbook 2019>. Photos from unsplash.com

The vast aquaculture production in China is supported by several factors, including a favorable natural environment and social & economic demand. The mariculture in China is characterized by low-trophic species cultured with long-line rafts, and the culture method requires a large sea surface area and massive labor input during the process. An accumulated sea surface area of 13,782 km^2 (3% of the total) was used by mariculture on the Chinese side in the Yellow Sea in 2018 (China Fishery Statistical Yearbook 2019). About 4.9 million people rely on fishery and aquaculture for their livelihood in China (FAO. 2018).

The mariculture in the Yellow Sea is concentrated around coastal bays or islands, and most of these areas are intensively cultured (Figure 3). The aquaculture activities with massive artificially cultured biomass and extensively spatial occupation have already become a non-negligible component in the local ecosystem. The impact on the regional ecosystem in the Yellow Sea at different temporal-spatial scales has drawn more concern recently (Yuan et al. 2010; Li et al. 2018; Zhao et al. 2019; Liu et al. 2021). For the sustainable development of the aquaculture industry, it is essential to understand the aquaculture involved ecosystem processes at different scales, establish methods for the carrying capacity estimation of cultured organisms within the local environment, and provide suggestions for mariculture spatial planning with sufficient scientific evidence.

Figure 3 The Integrated-Multi Trophic Aquaculture in Sanggou Bay, the primary culture species are kelp and oyster. Daily management is being conducted for the inspection of the culture organism conditions. Photo provided by Fang Jianguang.

The two major objectives of my PhD project are: (1) To establish and validate a high-resolution numerical current model which can provide physical information to the aquaculture-dominated ecosystems in the Yellow Sea and particularly on the northern shelf where previous knowledge has been limited, and (2) to apply the current model results to explain environmental interactions on aquaculture as well as providing input to biological models. To achieve these objectives, the Yellow Sea Model (YSM) model has been implemented from the NorKyst800 current model operating along the Norwegian coast (Asplin et al. 2020). The hydrodynamic results have been applied to study the hydrological features including the summertime thermal front jet and the internal tidal dynamics on the northern shelf of the Yellow Sea, which can be barely found in literatures. In addition to the oceanographic studies, the model results were also used to investigate the potential reason for recently massive mortality of bottom cultured scallops and correlated the event with ambient water temperature variations. An ecosystem model was set up for the large-scale multi-trophic aquaculture in Sanggou

bay to quantify the aquaculture-environmental interactions, with hydrodynamic information supplied as boundary conditions. The output tends to suggest that the model can be a useful tool for carrying capacity estimation and provide supportive information for aquaculture management. China and Norway have been collaborating scientifically for 40 years in the Bei Dou project and in the past years this collaboration has mostly focused on aquaculture related issues. We want to eventually establish the scientific framework and construct essential tools to support the sustainable aquaculture management along the coast of the Yellow Sea, which can be universally applied to aquaculture productions with different species, culture methods, or culture environment.

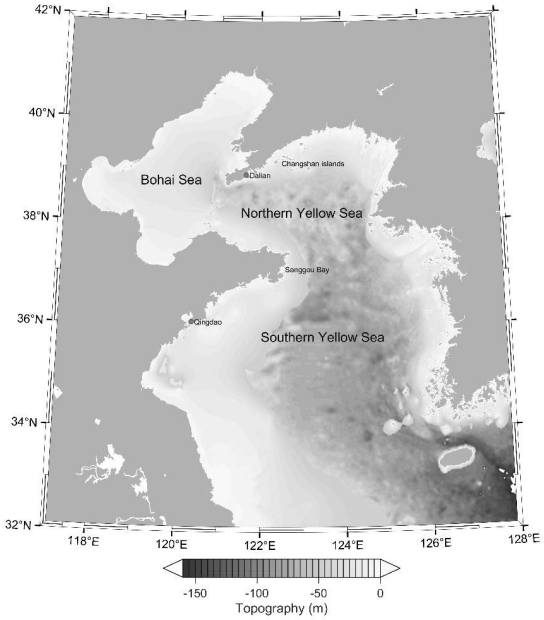

Figure 4 Location and topography (Etopo1) of the Yellow Sea and Bohai Sea. This phD project focused on two aquaculture areas: (1) The Integrated Multi-Tropic Aquaculture (IMTA) in Sanggou bay, and (2) the bottom aquaculture around Changshan islands.

The Yellow Sea

The Yellow Sea is a semi-enclosed marginal sea located between the mainland of China and the Korean Peninsula and adjacent to the West Pacific through the East China Sea. It covers approximately 458,000 km^2 with an average depth of about 44 m (Wei et al. 2010). The topography of the Yellow Sea is shown in Figure 4, with a trough located in the center and surrounded by a gradually sloping bottom towards the coast. The innermost part of the Yellow Sea is separated by the strait between the Shandong Peninsula and the Liaodong Peninsula, named the Bohai Sea, with an average depth of only 18 m. The second longest river in China, the Yellow River, flows directly into the Bohai Sea bringing sand and silt. A recently reported annual sediment load of 0.3 Gt/yr. is given (Wang et al. 2007), which is a large reduction from a previous estimate of 1.05 Gt/yr. (Milliman and Meade. 1983). It is still "one of the largest sources of sediment load from upland sources in the world" (Hwang et al. 2014). A fraction of this sediment load is resuspended and being transported as far as 700 km from the river mouth and reaches the southern part of the Yellow Sea, contributing to the formation of the intertidal flat along the Chinese coast. The boundary between the Yellow Sea and the East China Sea connects the Yangtze River mouth and the Jeju island with the southwestern tip of the Korea Peninsula. The total freshwater discharge of the five major rivers (Yellow, Yangtze, Geum, Han, Amarok) is estimated to be 1.031×10^{12} m^3/year, from which the Yangtze River has accounted for more than 89% playing a vital role in the biogeochemical process in the southern part of the Yellow Sea.

A defining feature of the Yellow Sea hydrodynamics is the macro-tidal energy input, especially along the coast. The tides in the Yellow Sea have been extensively studied with observations and numerical simulations. The tidal wave travels cyclonically in the Yellow Sea and loses energy due to the bottom friction (Kang. 1984). Co-tidal and co-range charts of semi-diurnal and diurnal constituents (Yanagi and Inoue. 1994) show four amphidromic points for the semi-diurnal constituents formed by reflecting waves. For the diurnal constituents, there are two amphidromic points in this region. The tidal range decreases northward along the Korean coast, especially for the M_2 tide. The maximum tidal amplitudes will approach 10 meters in the Gyeonggi bay (on the north-western part of the Korean coast) during perigean spring tides due to the resonant oscillation caused by the local bathymetry (Choi and Kim. 2006). The total tidal currents exceed 1.0 m/s near the coast and get gradually weaker offshore (Larsen et al. 1985). The residual currents are relatively weak and reported to be 0.02-0.08 m/s (Yanagi and

Inoue. 1994).

The climate in the Yellow Sea is controlled by the East Asian monsoon system (Hwang et al. 2014). The monsoon is caused by the temperature and humidity difference between the interior landmass and the West Pacific. Typically, there are four distinct seasons in this temperate zone, but the winter (December-February) and summer (June-August) govern the Yellow Sea's hydrodynamics. The precipitation over the Yellow Sea and the East China Sea from 1979 to 2007 is reported with monthly mean daily rates around 1.1 mm/day in December and 5.5 mm/day in July, and the annual daily mean rate ranging from 2.9 to 3.8 mm/day (Hwang et al. 2014). The annual mean air temperature reported for the Korean side of the Yellow Sea ranges between 10°C -16 °C. In winter, the mean January temperatures range from -5°C to 5°C, while in the summertime, the mean air temperature can be from 20°C to 26°C during August (UNEP, 2005). The monsoon wind regime leads to opposite winds in winter and summer. During winter, strong northerly winds and a negative surface heat flux contribute to the vertical mixing and adds to the continuous tidal mixing. This homogenized cold-water column lasts until spring. In the summer, the south-southeasterly wind is much weaker, and the solar radiation leads to well-defined stratified water in the central Yellow Sea. Tidal mixing dominates the coastal regions, resulting in homogeneous waters being separated from the interior by a tidal mixed front (Simpson & Hunter. 1971). Remnant cold water from last winter will stay below the seasonal thermocline throughout the summer season, known as the Yellow Sea Bottom Cold Water (YSBCW). The temporal evolution of the bottom water temperature of the Yellow Sea and Bohai Sea is demonstrated with the model result shown in Figure 5, and the associated vertical temperature structure of the selected section is presented in Figure 6.

The seasonal circulation in the Yellow Sea is the combination of tidal currents, seasonal wind-driven currents, and large-scale geostrophic flow. In winter, the strong winds and the cold air jointly contribute to forming a well-mixed water column. Episodic northerly winds with a speed of more than 10 m/s force a southward surface current. A bottom compensation flow transports warm and saline Pacific water into the central Yellow Sea, known as the Yellow Sea warm current (Lie et al. 2001). Both the Chinese coastal current and the Korean coastal current flow southward along the thermohaline front between the cold Yellow Sea water and the warm water from the West Pacific near Jeju island (Yuan et al. 2008; Yuan and Hsueh. 1998; Lie et al. 2013). The Yangtze River's freshwater discharge is minor

during winter and flows southward along the Chinese coast, reaching the Taiwan strait.

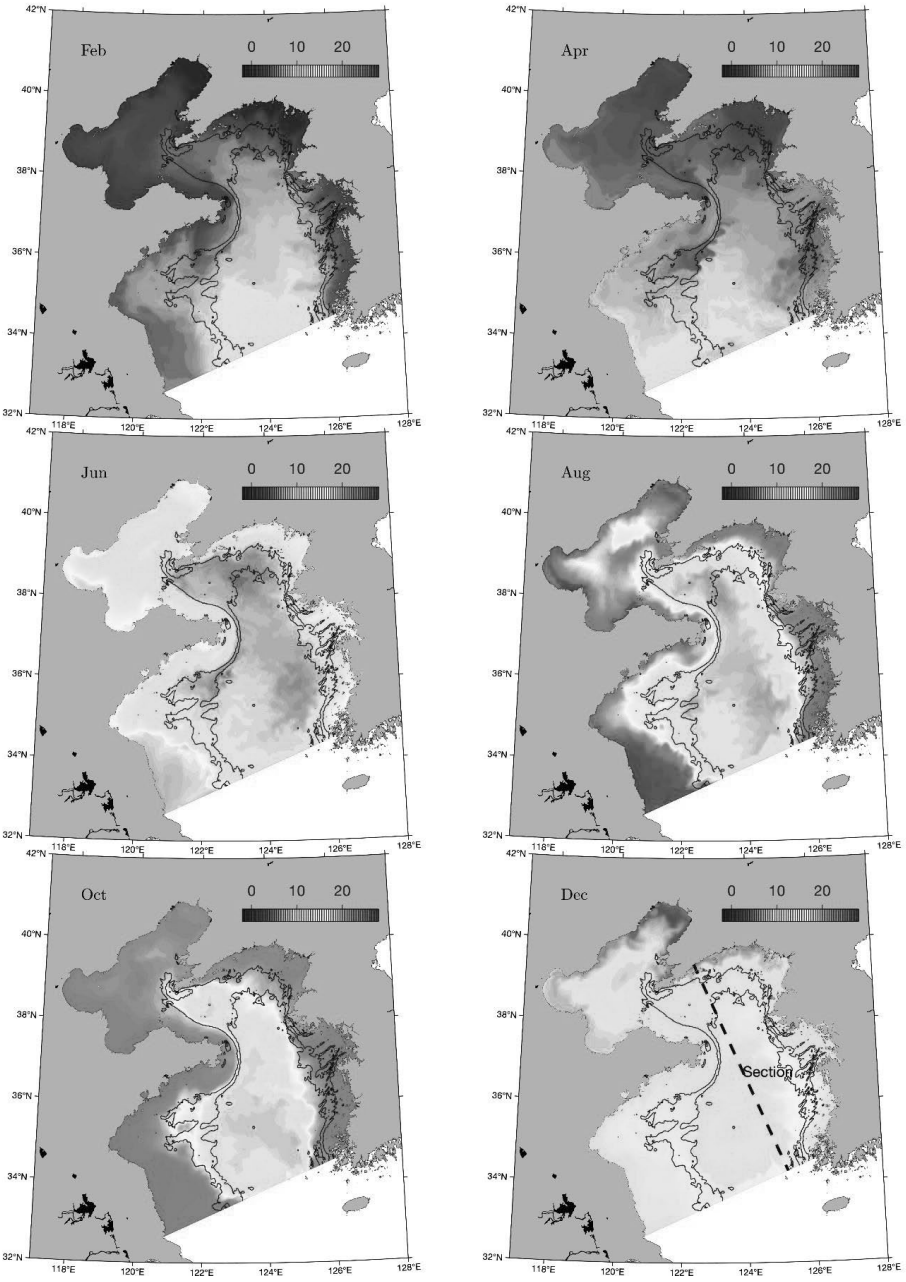

Figure 5 Bottom water temperature distribution from YSM results for different months. The section in Dec is where the vertical temperature will be presented in the next figure. The black contours represent the 40 m and 60 m isobaths.

The summertime is characterized by the YSBCW in the central basin below the seasonal thermocline, about 10-20 meters under the warm surface water. This cold-water mass is often surrounded by the tidal mixing front, where cooler surface patches can be observed from satellite images. This relatively shallow region is maintained by a balance between the tidal mixing power and the buoyancy force from solar radiation. The tidal mixing front forms roughly between the 20-50 m isobaths and separate the coastal mixed warm water and the central stratified water. The circulation in summer turns to flow cyclonically along the mixing front. The Korean coastal current flows northward, and the Chinese coastal current flows southward (Yuan et al. 2008; Isobe. 2008; Ichikawa and Beardsley. 2002). This cyclonic gyre has been identified from satellite-tracked drifter data (Beardsley et al. 1992; Pang et al. 2004). Unlike winter, the Yangtze River has maximum freshwater discharge in summer, the momentum drives the diluted water to disperse eastward, affecting the southern Yellow Sea.

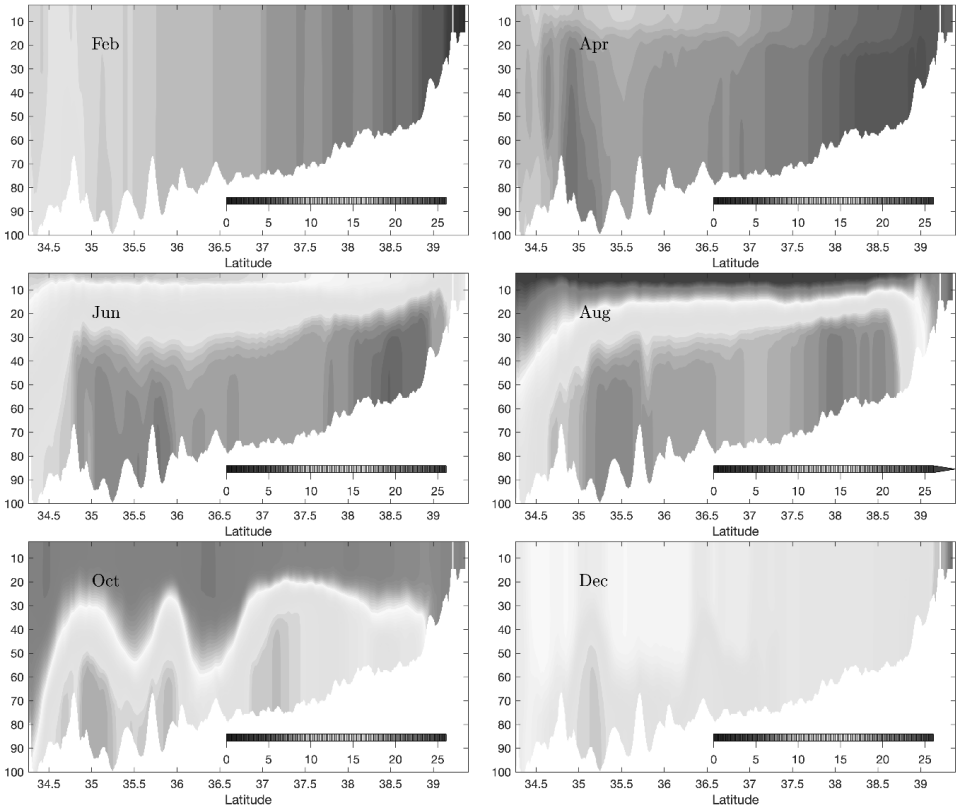

Figure 6 Vertical temperature structure for the section labeled in the previous figure for each month presented. Unit for the

vertical axis is meter and positive downward.

The Yellow Sea has been studied extensively from a variety of disciplines, and most hydrodynamic mechanisms of the Yellow Sea have been well explained with *in-situ* observations, floaters, satellite data, and numerical model results (Larsen et al. 1985; Yanagi and Inoue. 1994; Lie et al. 2001; Yuan et al. 2008). Li and Yuan (1992) described the formation and maintenance mechanisms of the YSBCW with theoretical models and made a comparison with observed temperature patterns. Su and Huang (1995) employed numerical models to study the vertical circulations within the YSBCW, predicting a two-layer circulation structure separated by the thermocline. Xia et al. (2006) described the summertime circulation structure with a three-dimensional hydrodynamic model in the Yellow Sea, illustrating the basin-scale circulation. Ichikawa and Beardsley (2002) have reviewed the studies regarding the general circulation in the Yellow Sea and the East China Sea, highlighting the issues remained to be solved including the mechanisms of Yellow Sea warm current and the Chinese coastal current. Wang et al. (2014) studied the seasonal southward migration of the YSBCW with a particle dispersion method. The thermal fronts on the shelves are of particular interest. These are commented in e.g., Liang et al. (2018) illustrating that they can have a significant effect on the phytoplankton growth and biological production (Li et al. 2006; Chen. 2009; Sun & Cho. 2011; Xin et al. 2015).

Besides the large-scale and relatively "periodical" mechanisms, there are also studies on the internal waves in the Yellow Sea (Hsu et al. 2000; Liu et al. 2009; Liu et al. 2019). The stratified water bodies in the YSBCW and the tidal mixing front provide conditions for the generation and propagation of internal waves. Internal solitary waves (ISW) have been detected from synthetic aperture radar images propagating within the southern Yellow Sea and along the coast (Alpers et al. 2005; He et al. 2008; Hsu et al. 2000; Teixeira et al. 2006; Warn-Varnas et al. 2005; Zhao et al. 2014). Liu et al. (2019) have studied the M_2 internal tide in the Yellow Sea with a numerical model, estimated the energy contribution of the M_2 internal tide to be about 0.8% of total tidal dissipation, which is negligible on the scale of the entire Yellow Sea. Compared to those studies in the South China Sea, the internal waves in the northern Yellow Sea have received less attention because of the seasonality of the stratification and minor contribution to ocean mixing in this shallow sea. However, in aquaculture areas on the northern shelf, where internal tides are generated locally around the islands, the impact on local hydrodynamics still needs to be clarified.

Part of this thesis (**papers I and II**) addresses especially tidal dynamics in the northern Yellow Sea to fill gaps in the knowledge of hydrodynamic processes of importance for aquaculture.

Aquaculture Environmental Interaction

The geographic location and environmental characteristics of the Yellow Sea makes it important in East Asia. It supports a wide variety of marine living resources, and a total of 113 families (321 species) of fish have been recorded (Liu and Ning. 2011). The human population density around the Yellow Sea is more than 200 inhabitants/km^2 (FAO, 2018). Besides the global environmental change, anthropogenic activities impose pressure on the Yellow Sea large marine ecosystem (Zhang et al. 2019). The environmental impact and sustainable development of mariculture in China have become more in focus during recent years. Although non-fed species such as seaweed have been identified to remove nutrients from Chinese coastal waters (Xiao et al. 2017), the anthropogenically introduced biomass may lead to a cumulative effect on the marine ecosystem at a large scale. Several ecosystem problems have been reported in the Yellow Sea, including a change in abundance and species composition, an increased frequency of harmful algal blooms, and loss of habitats (Zhang et al. 2019).

There is a trend of the dominant algae turning from diatoms to dinoflagellates in recent years, potentially resulted from the increased eutrophication and decreased ratio of Si:N (Zhang et al. 2019). The change in the biomass and composition of phytoplankton and zooplankton may lead to further problems as they are fundamental groups in the marine food chain (Zhang et al. 2019). There are also reports on the miniaturization of planktons in the Yellow Sea, the decrease of zooplankton with size larger than 505 μm and phytoplankton larger than 77 μm were detected on the Chinese side of Yellow Sea (Zhang et al. 2019), which can potentially be connected to the intensive shellfish aquaculture. With field observations, Li et al. (2017) have drawn the conclusion that intensive aquaculture is 'likely' to have a negative impact on the local environment around Weihai coastal areas besides eutrophication and ocean acidification. The results-oriented analysis provides a good scientific hypothesis and motivates researchers to understand the mechanisms of the observed phenomenon.

We usually focus on the cultured organism growth and their interaction with the environment in

aquaculture systems that can be manipulated with management strategies. Regarding this aspect, carrying capacity (CC) is a fundamental concept with a broadly description as “the maximum level of use an area can tolerate before unacceptable degradation occurs” (Weitzman and Filgueira. 2020). Typically, carrying capacity can be measured as a function of different aquaculture related parameters depending both on the relevant carrying capacity type and/or the management objectives. According to different management objectives, a comprehensive and widely accepted four-pillar approach has been applied defining the carrying capacity into four categories (Inglis et al. 2000; McKindsey et al. 2006), namely physical, production, ecological, and social carrying capacities.

The physical carrying capacity of a site is often represented as the geographic area that is both available and suitable for aquaculture (Whitzman and Filgueira. 2020). Instead of providing the evaluation of “physically limited production numbers”, it is useful in determining the area availability and suitability for aquaculture activities. The physical carrying capacity is measured largely by the physical factors (water depth, temperature, salinity, flow condition, substrate type, and oxygen concentration) which drives the suitability to satisfy the specific requirement of the cultured species (McKindsey et al. 2006). It is usually the basic component in site selection for the early stage of aquaculture planning.

The definition of production carrying capacity is straightforward as it mostly describes the stocking density at which production biomass is maximized (McKindsey et al. 2006). As a practical application of carrying capacity, the production carrying capacity has been well-studied and most relevant for economic evaluation and farm management (Ross et al. 2013). The stocking density automatically served as the basic parameter for the evaluation of production CC, and it is highly linked to the hydrodynamics, food supply, and physiological characteristics of the culture organisms (Ferreira et al. 2013).

The ecological carrying capacity describes the maximum density of cultured species that does not cause unacceptable impacts on the natural environment (McKindsey. 2013). The ecological CC requires the knowledge and information on ecosystem processes at different production stages, which naturally make the evaluation of ecological CC at the ecosystem scale and requires to resolve the aquaculture-environmental interaction (including physical, chemical, and biological process) at different spatial and temporal scales. Ecosystem models integrating physical, chemical, and physiological processes with

many spatial-temporal scales are necessary tools for ecological carrying capacity estimations. However, regarding the systematic complexity, the actual estimation of ecological CC is usually based on models with limited interaction processes and essential assumptions and simplifications (Filgueira et al. 2013).

The social carrying capacity, which falls into the category of social sciences, does not have an agreed-upon definition yet (Weitzman and Filgueira. 2020). Dalton et al. (2017) argues the definition of social carrying capacity as "the level of aquaculture beyond which environmental and social impacts exceed acceptable levels, measured by community or stakeholder satisfaction, desirability, or preferences". However, the definition is kind of ambiguous as the quantification of social impacts can be extremely difficult, and the relevant scale of the social carrying capacity will be highly dependent on the objectives and system characteristics specific to each case. Social carrying capacity for aquaculture gained popularity just recently and the relevant models or tools are poorly developed (Weitzman and Filgueira. 2020). Generally, assessing the social carrying capacity of an area requires addressing the interests of all stakeholders (McKindsey et al. 2006; Byron & Costa-Pierce. 2013). Although the social CC is the least well-studied carrying capacity component, it still can be considered as most critical for the aquaculture management (Weitzman and Filgueira. 2020). It is reported by Banta & Gibbs (2009) that social impacts and conflicts are limiting factors in development scenarios. Additionally, the diversity in social systems also adds complexity in social CC evaluation.

From the description above, we see that the physical, production, ecological, and social carrying capacities are defined with progressive complexity. The assessment or application of either capacity often needs to be determined by objectives and stakeholder expectations of the aquaculture scenarios. Although the carrying capacity assessment is highly customized regarding each specific case, the universal steps can be common. We first need to identify the indicators according to the scenarios of the local ecosystem or social system, as to measure the impact from aquaculture activities. And the critical conditions which defines the carrying capacity should be determined. Then the relationship between the aquaculture activity and the indicators needs to be quantified with proper methods, e.g., *in-situ* observations or ecosystem models, etc. The final step is to estimate the carrying capacity with expressible aquaculture parameters (stocking density, harvestable biomass, number of fish cages, etc.) within the acceptable threshold determined by the critical conditions (Weitzman and Filgueira. 2020).

The aquaculture in China usually covers a large area of the sea surface and the biomass of culture organisms are overwhelmed in the local environment (illustrated in Figure 3). Management tools are essential for aquaculture sustainability when the farming activity defines the local ecosystem at a bay scale. Previously, several studies on aquaculture-environmental interactions have been conducted along the coast of the Yellow Sea based on numerical simulations. Shi et al. (2011) have parameterized the kelp growth and hydrodynamic drag from aquaculture facilities and established a three-dimensional physical-biological coupled model to seek an optimal culture density in Sanggou Bay. Xuan et al. (2019) examined the impact of intensive surface aquaculture facilities on the local circulation in the same bay. They found a reduced surface flow and intensified bottom flow at the open boundary of the bay. Zhao et al. (2019) have evaluated effluents from fish farms with numerical hydrodynamic modelling along the coast of Qingdao and claimed that there is a negligible sedimentation. Another example is the occasionally harmful algal blooms of *Ulva prolifera* happening in the Yellow Sea originating from the seaweed *Porphyra yezoensis* aquaculture in the East China Sea. Through a complex biogeochemical process, these blooms cause an ecosystem disaster that cost $100 million to repair (Hu et al. 2010).

Part of the thesis (**papers III and IV**) addresses environmental interaction and carrying capacity within the Yellow Sea. Based on results from the Yellow Sea Model an estimation of environmental stress on bottom cultured scallops has been developed, as well as developing an ecosystem model for the aquaculture suitability assessment and production carrying capacity estimation in Sanggou bay.

Synthesis Layout

The purpose of the work has been to both understand and provide detailed information of the hydrodynamics of particularly the northern Yellow Sea and to investigate interactions between the environment and aquaculture. Thus, this dissertation is organized into two parts.

The first part (**papers I and II**) establishes the numerical model of the Yellow Sea and Bohai Sea and investigates the hydrodynamic features that may have a particular impact on aquaculture. The Regional Ocean Model system (ROMS) is implemented for the Yellow Sea and the Bohai Sea to provide hydrodynamic information with realistic forcing. The model results are validated at the northern shelf of the Yellow Sea against various observations. The hydrological and thermohaline dynamics are

presented from the model results (**paper I**). Details on the current structure induced by the barotropic tide and the dynamics of the thermal front jet has been firstly described with high-resolution hydrodynamic simulations together with *in-situ* observations on the northern shelf of the Yellow Sea. Also, the internal tidal pattern and dynamics are investigated in **paper II**. The existence of the YSBCW and the tidal mixing front allows the propagation of internal waves, from which the internal tide can be captured by the model setup. We have reconstructed the internal tide generation and propagation pattern in the weakly stratified tidal mixing front in the northern Yellow Sea and evaluated its short-term impact on the local current system. We have demonstrated the importance of the current modification from the internal tides on the local flow field with up to 30% of the magnitude, which hasn't been previously described.

The second part (**papers III and IV**) focuses on applying the hydrodynamic results on aquaculture. There are two cases presented, one for the bottom culture of Japanese scallops in the open sea, and the other for the suspended Integrated Multi-Trophic Aquaculture (IMTA) covering a coastal bay. For the bottom culture case (**paper III**), the environmental conditions are essential since the organisms rely on food being brought to their locations with a favorable surrounding water quality. Recently, several reports of massive mortality events have aroused public attention on the suitability of the bottom culture method regarding the physiological features of the Japanese scallops. Our results are the first attempt to construct a spatial-temporal variability map of the ambient water temperature for cultured scallops, which can be utilized for selection of sites in tidal mixing front areas (risk assessment and physical carrying capacity). For the IMTA case (**paper IV**), an ecosystem model is established incorporating hydrodynamic data, individually based models, and population dynamics for Sanggou bay. The culture organism growth and their interaction with the local environment is assessed. The carrying capacity estimation method is discussed with the model results. The application of the high-resolution current model results as a boundary condition for the ecosystem modelling regarding integrated multi-trophic aquaculture to discuss the aquaculture-environmental interaction process hasn't been presented before.

2 Summary of the papers

Paper I: Currents on the northern shelf of the Yellow Sea

The Regional Ocean Model System (ROMS) is implemented for the Yellow Sea and the Bohai Sea (hereafter YSM). The model has 787×826 horizontal grid nodes with a resolution of approximately 1 km, and there are 40 vertical σ levels with an enhanced resolution near the surface and the bottom. Realistic forcing, including the tides, the atmospheric forcing, and the ocean current & water properties, are applied to the model. Various observations, including satellite data and *in-situ* moorings, are used for model validation, and our first objective was to quantify the quality of the model results. The comparison of the current time series and bottom temperature evolution shows good agreement between model and observation. The averaged root-mean-square error for the measured and simulated current speed is about 0.08 m/s at the calculation depths, 13% of the average current magnitude. The simulated bottom temperature resembles the observed values quite well during the warming and cooling process of the water body at the mooring locations.

Results from the study agree with previous reports in the literature. Details on the tidal current, seasonality of water temperature, wind-driven current, and particle dispersion results are discussed. Seasonal dynamics occur in the Yellow Sea as the East Asian monsoon system dominates the regional climate. The winds continually change in the model domain, creating episodic currents in the upper part of the sea lasting from hours to a couple of days in all seasons. The barotropic tide is the dominant current component throughout the year and provides a continuous source for vertical mixing in the shallow region. A seasonal thermocline is formed during summer at a depth around 15~20 m in the central part of the Yellow Sea, resulting from the balance between the solar radiation induced buoyancy flux and tidal mixing. The remnant cold water from the previous winter stays below the seasonal thermocline, known as the Yellow Sea bottom cold water (YSBCW). This cold-water mass is horizontally separated by the tidal mixing front, typically around the 20-60 m isobaths. The thermal front associated current, formed from the balance between horizontal density induced pressure gradient and the Coriolis force, is vital for the westward transport in the frontal region during summer. The physical information from the YSM is used for ecological studies. Model improvements should be sought to produce even more realistic results. Testing internal model formulations as turbulence sub-models and the vertical grid arrangement can make the model perform better.

Paper II: Summertime M_2 internal tides in the northern Yellow Sea

The summertime Yellow Sea bottom cold water (YSBCW) is a typical thermal structure of this marginal sea with a central trough. YSBCW is surrounded by the tidal mixing front, which locates between the 20 - 60 m isobaths with relatively homogeneous water inshore and stratified water offshore. The stratified waters then enable the generation and propagation of baroclinic waves, including the internal tides. In this paper, we combined results from the YSM and the observations to investigate the dynamics of the internal tides in the Yellow Sea and focused on the dominating M_2 component. During the summer of 2017, an RDI ADCP was moored at the bottom on the northern shelf of the Yellow Sea near the Changshan islands. The vertical pattern of a mode-1, semi-diurnal internal tide is captured by the moored ADCP as well as the simulation results. With further analysis of the observation and model results, we present the internal tidal dynamics and energetics in the northern Yellow Sea and discuss how these physical processes may potentially affect the local ecosystem by enhanced or reduced water transport being about 30% of the external semi-diurnal tidal flow component.

Our results demonstrate that the internal tide is mostly locally generated with a rapid decay away from its source. The most substantial generation area for the semi-diurnal internal tide is along the Korean coast. The Changshan islands are also an area with internal tide generation, although with less energy than further east, but with evident potential influence on the bottom aquaculture.

Paper III: Rapid water temperature variations at the northern shelf of the Yellow Sea

The northern shelf of the Yellow Sea is an important area for the bottom aquaculture of Japanese scallops *Patinopecten yessoensis* with economic importance (Zhou. 2012). The Japanese scallops grow from juveniles to market size during a regular 3-year culture period, in which various environmental changes may occur. The high mortality of the bottom culture scallops reported recently relates to the bottom water temperature variability in summer (Zhao et al. 2019). The YSM results are applied to this

region for the short-temporal-scale temperature variations and the potential impact on cultured bivalves to support risk assessment and sustainable management of scallop sea ranching.

The research focuses on the scallop bottom culture area near Zhangzidao island. The time series of modelled bottom temperature is extracted and analyzed within the region. The water temperature from another intensive aquaculture region in Sanggou Bay is also presented for comparison. A simulation with tidal forcing only is conducted to illustrate the contribution from tidal currents to the bottom temperature variation. The temperature difference can typically be larger than ~10 ^{o}C in the seasonal thermal front region in late summer. Current oscillations from the semi-diurnal tide (mainly the M_2 constituent), with an additional oscillation of an around two-week period and a current magnitude of only 0.01-0.02 m/s, move the thermal front back and forth in the scallop culture area, exposing the organisms for a relatively large temperature variation.

The spatial influence of these bottom temperature oscillations was quantified with an index by multiplying the temperature difference between the maximum temperature and minimum temperature of the first half of the wave period with the time between the two in days and then adding up these values at each grid square in the numerical model domain, thus representing the aggregated effect of the local temperature variation. The geographical distribution of this index identifies “critical areas” and discusses the impact of the rapid temperature oscillation on the sea ranching of scallops. A high index value was found in 2014 within the bottom culture area when high scallop mortality was reported. The hydrodynamic data can provide essential information for developing sustainable scallop bottom aquaculture within the region when combined with scallop physiology studies.

Paper IV: A physical-biological coupled ecosystem model for integrated aquaculture of bivalve and seaweed in Sanggou Bay

In this paper, our study region is in the Sanggou bay, where oyster and seaweed aquaculture cover about two-thirds of the bay area during the production seasons. The nutrient cycle and individual growth of the integrated-cultured bivalves and seaweed (IMTA) are studied with an ecosystem model, coupling individual-based models and the local hydrodynamic information. The individual growth model of

Pacific oysters *Crassostrea gigas* is implemented with the dynamic energy budget (DEB) theory. The individual model of kelp *Saccharina japonica* is based on a typical exponential growth formula with local validation. The model is computed based on a box model concept, where we assume that the physical properties are homogeneous within each box. The hydrodynamic model provides the external water mass and nutrient content (nitrogen) exchange with water quality modules. The growth of oysters and kelp are simulated under different aquaculture density combinations, and the feedback to the local nutrient conditions is also discussed.

Validated with several observations, including organism growth, phytoplankton biomass, and dissolved inorganic nitrogen concentration, the ecosystem model reproduces the seasonal circulation and general spatial patterns well. Different aquaculture arrangements are represented with species combination and culture density adjustment in each box of the model. The interaction between the integrated aquaculture system and the local environment in Sanggou bay can be evaluated with the model-defined ecological dynamics. A present combination of 50 oysters/m^2 and 4 kelp/m^2 based on decades of aquaculture practice seems to be a balanced optimal choice of ecological impact and economic demand.

3 Prospects

China has been the world's leading seafood producer for many years, and domestic aquaculture production has exceeded the capture production since 1993 (FAO FishStat). Obviously, the need for a healthy and sustainable aquaculture in China is absolutely necessary to keep up with an increasing need for food supply. As an important shellfish producing area, the Yellow Sea and Bohai Sea will continue to contribute a considerable amount of bivalve biomass to the consumers. The high aquaculture yield has brought increased concerns of the pressure on the coastal ecosystem and sustainability worldwide (Milewski. 2001; Cao et al. 2007; Ferreira et al. 2007; Whitmarsh and Palmieri. 2008; Galparsoro et al. 2020). Although the Chinese aquaculture consists primarily of low-trophic species, especially bivalves and seaweed, the overwhelming biomass produced may still affect the ecosystem at the population level, e.g., a phytoplankton abundance decline, a biodiversity loss, or an occurrence of ecological disasters

such as harmful algal blooms (Hu et al. 2010; Zhang et al. 2019). Therefore, policymakers and aquaculture practitioners need solid science-based information and comprehensive knowledge of the ecosystem at different scales to apply sound management strategies. The Chinese government has already committed to regional legislations for aquaculture functional zoning to seek sustainable development. Therefore, the aquaculture industries are facing challenges from both the requirement on ecosystem sustainability and the pressure of government policies. For instance, the massive mortality of bottom cultured scallops in the northern Yellow Sea was firstly reported in 2014, and the occurrence of such event became more frequent in recent years (Zhao et al. 2019), which greatly affected the development of the related aquaculture companies. In Sanggou bay, with respect to the environmental regulations, the long-line rafts within 2 km from the coast have been removed since 2018, providing more coastal space for the public. To achieve a sustainable development of aquaculture in balance with the demand from different stakeholders (industry, individual, government, etc.), we need a long-term input from scientific-research, enterprise participation, and policy support.

Sustainable development of aquaculture can be different from area to area by many reasons, e.g., difference in geographical conditions, hydrological conditions, culture method, market demands, or the legislative systems. The general framework to achieve sustainability is still similar, namely, to conduct the aquaculture development and management under the limits of the various carrying capacity indexes. Sanggou bay has been an experimental field for low-trophic aquaculture studies with participation from researchers globally (Hawkins et al. 2002; Nunes et al. 2003; Duarte et al. 2003; Zheng et al. 2012) and is suitable for demonstrating a sustainable aquaculture system and what activities are needed to monitor this. Aquaculture have been practiced in Sanggou bay for decades and has witnessed a change from monoculture to polyculture. Ever since the first carrying capacity related project was conducted in the bay (Fang et al. 1996), the integrated multi-trophic aquaculture (IMTA) has become the major aquaculture method and continues to improve with the progress of various scientific studies (Shi et al. 2013; Lu et al. 2015; Zeng et al. 2015; Xuan et al. 2019). The recent adoption of the “MOM” system in Sanggou bay monitoring the sediments (Zhang et al. 2020) showed a similar good status as 10 years ago (Zhang et al. 2009), indicating that the aquaculture in the bay is sustainable regarding this. Currently, the “eco-farming” method has been demonstrated and promoted in the bay (Mao et al., 2019), implying a reduced stocking-density that achieves better individual quality and a higher economic profit and

serves as an excellent example of a fruitful collaboration between science and industry.

Our work contributes to the scientific part under the big scope of sustainable development of aquaculture, focusing on providing effective model results. Application of the hydrodynamic models within this thesis helped to clarify the background environmental conditions at specific aquaculture regions in the northern Yellow Sea. The temperature index derived with the simulation results impelled the stakeholders to reconsider the risk-assessment and site-selection for bottom scallop sea-ranching during the planning stage. The stock-density and production relation presented from the ecosystem model of the low-trophic multi-culture in Sanggou bay also caused some thoughts on harvestable biomass and individual product quality for large-scale aquaculture, which contributes to the demonstration of "eco-farming" method. Local stakeholders including aquaculture industries and the local government are strongly interested in the simulation results with higher spatial resolution and more detailed biological process, which requires the input for both model optimization, experimental study, environmental monitoring effort, and continuous production records.

To further contribute to the sustainable development of aquaculture around the Yellow Sea, more effort is required to improve the model capabilities and strengthen the cooperation with physiological and ecological studies. Both the hydrodynamic and ecosystem model need further validation and improvements to support the general aquaculture management. The performance of model application greatly depends on the model construction, e.g., the theoretical basis, the rationality of model assumptions, the spatial-temporal resolution, etc. Processes or dynamics that are not included in the model setup or equations will not be revealed in the model results, especially for the deterministic models. Therefore, the major objectives of specific applications should be clarified prior to the model construction to make sure the necessary components and processes are included.

A better resolving of the ecological processes regarding the culture organisms will be important for the ecosystem modelling. The individual based models (IBM) which can better describe detailed feedbacks of culture organisms facing environmental variations are expected. This requires the further development and involvement of the individual growth theory based on the physiological and ecological studies in the laboratory or in the field. We also need a proper introduction of the population dynamics to enhance the model performance. The reasonable parameterization of the intra-species competition

helps to better predict the distribution of individual qualities. The correlation of the massive mortality event of bottom cultured scallops and the ambient water temperature variation motives the clarification of the corresponding physiological mechanisms. Which may eventually provide useful information for the mitigation management with developing regional suitability assessment index incorporating the scallop physiological knowledge, feed availability, and environmental variation. Mortality of the culture organisms is another key parameter that requires optimized expression, it covers various factors including starvation, unsuitable environmental, predator feeding, etc. and determines the population size as harvestable individuals. Data from physiological laboratory experiments, field experiments, and actual production are necessary to formulate expressions for the population dynamics.

Further concerns will also be laid on the environmental feedback to the large-scale and regular aquaculture around the Yellow Sea. The aquaculture facilities and high yield at regional scale, e.g., Sanggou bay, may affect both the hydrodynamics and the ecosystem composition. The intensive shellfish aquaculture farms distributed along the Yellow Sea coast may result in a top-down controlled ecosystem at regional scale, with support from previous reports on the miniaturization of planktonic groups (Zhang et al. 2019). In addition to the physiological knowledge attained from experiments, the ecosystem scale evaluation from modelling systems, we will also work on the setup and maintenance of long-term monitoring system in the aquaculture environment for the efficient supplement of observation data.

The work done in this thesis will be the foundation of our future work, we expect the follow-on research projects can provide solid multi-disciplinary scientific support for the sustainable aquaculture development & management and related legislation in China.

Reference

Albretsen, J., Aure, J., Sætre, R., & Danielssen, D. S., 2012. **Climatic variability in the Skagerrak and coastal waters of Norway.** *ICES Journal of Marine Science*, *69*(5), 758-763.

Asplin, L., Johnsen, I.A., Sandvik, A.D., Albretsen, J., Sundfjord, V., Aure, J., Boxaspen, K.K., 2013. **Dispersion of salmon lice in the Hardangerfjord.** *Marine Biology Research, 10*, 216–225. doi:10.1080/17451000.2013.810755

Asplin L, Albretsen J, Johnsen IA, Sandvik AD (2020) **The hydrodynamic foundation for salmon lice dispersion along the Norwegian coast.** *Ocean Dyn.* https://doi.org/10.1007/s10236-020-01378-0.

Banta W, Gibbs M (2009) **Factors controlling the development of the aquaculture industry in New Zealand: legislative reform and social carrying capacity.** *Coastal Management* 37: 170– 196.

Becker, J. J., Sandwell, D. T., Smith, W. H. F., Braud, J., Binder, B., Depner, J. L., ... & Ladner, R., 2009. **Global bathymetry and elevation data at 30 arc seconds resolution: SRTM30_PLUS.** *Marine Geodesy*, *32*(4), 355-371.

Broell F, McCain JSP, Taggart CT (2017) **Thermal time explains size-at-age variation in molluscs.** *Mar Ecol Prog Ser*, 573: 157-165.

Budgell WP (1982) **The influence of the spring-neap tidal cycle upon vertical stratification in Chesterfield Inlet, Hudson Bay.** *Nat Can*, 109(3): 709-718.

Bleck R. 2002 **An oceanic general circulation model framed in hybrid isopycnic-Cartesian coordinates** *Ocean. Model.* 4 55–88. https://doi.org/10.1016/S1463-5003(01)00012-9

Byron CJ, Costa-Pierce BA (2013) **Carrying capacity tools for use in the implementation of an ecosystem's approach to aquaculture.** In: Ross LG, Telfer TC, Falconer L, Soto D, Aguilar-Manjarrez J (eds) Site Selection and Carrying Capacities for Inland and Coastal Aquaculture, pp. 87–101. *FAO*, Rome, Italy.

Cai, B., Zhu, C., Liu, H., Chang, L., Xiao, L., Sun, Q., Lin, F. (2018). **Model Simulated growth of kelp Saccharina japonica in Sanggou Bay.** *Progress in Fishery Science,* 40 (3). https://dx.doi.org/10.19663/j.issn2095-9869.20180419001 (in Chinese with English abstract)

Cao, L., Wang, W., Yang, Y., Yang, C., Yuan, Z., Xiong, S., & Diana, J. (2007). **Environmental impact of aquaculture and countermeasures to aquaculture pollution in China.** *Environmental Science and Pollution Research-International*, *14*(7), 452-462. https://doi.org/10.1065/espr2007.05.426

Caperon, J., Meyer, J. (1972). **Nitrogen-limited growth of marine phytoplankton—I. changes in population characteristics with steady-state growth rate** *Deep Sea Research and Oceanographic Abstracts* 19(9), 601-618. https://dx.doi.org/10.1016/0011-7471(72)90089-7

Chen, C., R.C. Beardsley, and G. Cowles. 2006. **An unstructured grid, finite-volume coastal ocean model (FVCOM) system**. *Oceanography* 19(1):78–89, https://doi.org/10.5670/oceanog.2006.92.

Chopin, T., Buschmann, A., Halling, C., Troell, M., Kautsky, N., Neori, A., Kraemer, G., Zertuche-González, J., Yarish, C., Neefus, C. (2001). **Integrating Seaweeds into Marine Aquaculture Systems: a Key toward Sustainability** *Journal of Phycology* 37(6), 975-986. https://dx.doi.org/10.1046/j.1529-8817.2001.01137.x

Chen, C. T. A., 2009,. **Chemical and physical fronts in the Bohai, Yellow and East China seas.** *Journal of Marine Systems*, *78*(3), 394-410.

Dalton T, Jin D, Thompson R, Katzanek A (2017) **Using normative evaluations to plan for and manage shellfish aquaculture development in Rhode Island coastal waters.** *Marine Policy* 83: 194–203.

Dee, D. P., 1995. **On-line estimation of error covariance parameters for atmospheric data assimilation.** *Monthly weather review*, *123*(4), 1128-1145.

Dee, D. P., Uppala, S. M., Simmons, A. J., Berrisford, P., Poli, P., Kobayashi, S., ... Bechtold, P., 2011. **The ERA-Interim reanalysis: Configuration and performance of the data assimilation system.** *Quarterly Journal of the royal meteorological society*, *137*(656), 553-597.

Duarte, P., Meneses, R., Hawkins, A., Zhu, M., Fang, J., Grant, J. (2003). **Mathematical modelling to assess the carrying capacity for multi-species culture within coastal waters** *Ecological Modelling* 168(1-2), 109 143. https://dx.doi.org/10.1016/s0304-3800(03)00205-9

Egbert G. D. and Erofeeva S. Y. 2002 **Efficient inverse modeling of barotropic ocean tides** J. *Atmos. Ocean. Tech.* 19183–204. https://doi.org/10.1175/1520-0426(2002)019%3C0183:EIMOBO%3E2.0.CO;2

EPA (Environmental Protection Agency, USA). **Rates, constants, and kinetics. Formulations in surface water quality modeling: 2nd Edition**, 1985:455

FAO (2018)**. Fishery and Aquaculture Statistics 2016/FAO annuaire. Statistiques des pêches et de l'aquaculture 2016/ FAO anuario. Estadísticas de pesca y acuicultura 2016.** Rome/Roma. 104pp.

Fang, J.-G & Sun, H.-L & Kuang, S.-H. (1996). **Assessing the carrying capacity of Sanggou Bay for culture of kelp Laminaria japonica.** *Marine Fisheries Research.* 17. 7-17. (in Chinese with English abstract)

Ferreira, J. G., Hawkins, A. J. S., & Bricker, S. B. (2007). **Management of productivity, environmental effects and profitability of shellfish aquaculture—the Farm Aquaculture Resource Management (FARM) model**. *Aquaculture*, 264(1-4), 160-174. https://doi.org/10.1016/j.aquaculture.2006.12.017Get rights and content

Filgueira, R., Grant, J., Strand, Ø. (2014). **Implementation of marine spatial planning in shellfish aquaculture management: modeling studies in a Norwegian fjord** *Ecological Applications* 24(4), 832 843. https://dx.doi.org/10.1890/13-0479.1

Filgueira, R., Guyondet, T., Bacher, C., Comeau, L. (2015). **Informing Marine Spatial Planning (MSP) with numerical modelling: A case-study on shellfish aquaculture in Malpeque Bay (Eastern Canada)** *Marine Pollution Bulletin* 100(1), 200-216. https://dx.doi.org/10.1016/j.marpolbul.2015.08.048

Fairall, C. W., Bradley, E. F., Rogers, D. P., Edson, J. B., & Young, G. S., 1996. **Bulk parameterization of air-sea fluxes for tropical ocean-global atmosphere coupled-ocean atmosphere response experiment**. *Journal of Geophysical Research: Oceans*, *101*(C2), 3747-3764.

Gao G, Zhang J, Li M, Ma S, Guo X, Jiang W, Lv X (2017) **Effects of temperature fluctuation on physiological and immune parameters of scallop (*Patinopecten yessoensis*)**,*Prog Fish Sci*, 38 (3) 148–154 (In Chinese).

Godin G (1972) **The Analysis of Tides**, *University of Toronto Press*, Toronto, 264 p.

Gill, A.E., 1982. **Atmosphere-Ocean Dynamics.** *Academic Press*, New York, 662 pages.

Haidvogel, D. B., Arango, H., Budgell, W. P., Cornuelle, B. D., Curchitser, E., Di Lorenzo, E., ... & Levin, J., 2008. **Ocean forecasting in terrain-following coordinates: Formulation and skill assessment of the Regional Ocean Modeling System**. *Journal of Computational Physics*, *227*(7), 3595-3624.

Hongmei Li, Xiaomin Li, Qiang Li, Ying Liu, Jide Song, Yongyu Zhang, 2017. **Environmental response to long-term mariculture activities in the Weihai coastal area, China,** Science of The Total Environment,Volumes 601–602 ,Pages 22-31, ISSN 0048-9697, https://doi.org/10.1016/j.scitotenv.2017.05.167.

Galparsoro, I., Murillas, A., Pinarbasi, K., Sequeira, A. M., Stelzenmüller, V., Borja, Á., ... & Gimpel, A.(2020) **Global stakeholder vision for ecosystem-based marine aquaculture expansion from coastal to offshore areas**. *Reviews in Aquaculture*. https://doi.org/10.1111/raq.12422

Gangnery, A., Bacher, C., Boyd, A., Liu, H., You, J. & Strand, Ø. (2021). **Web-based public decision support tool for integrated planning and management in aquaculture.** *Ocean & Coastal Management*, 203, 105447. https://doi.org/10.1016/j.ocecoaman.2020.105447

Grant, J., Bacher, C. (2001). **A numerical model of flow modification induced by suspended aquaculture in a Chinese bay** *Canadian Journal of Fisheries and Aquatic Sciences* 58(5), 1003 1011. https://dx.doi.org/10.1139/f01-027

Grant, J., Curran, K., Guyondet, T., Tita, G., Bacher, C., Koutitonsky, V., Dowd, M. (2007). **A box model of carrying capacity for suspended mussel aquaculture in Lagune de la Grande-Entrée, Iles-de-la-Madeleine, Québec** *Ecological Modelling* 200(1-2), 193 206. https://dx.doi.org/10.1016/j.ecolmodel.2006.07.026

Guyondet, T., Roy, S., Koutitonsky, V., Grant, J., Tita, G. (2010). **Integrating multiple spatial scales in the carrying capacity assessment of a coastal ecosystem for bivalve aquaculture** *Journal of Sea Research* 64(3), 341 359. https://dx.doi.org/10.1016/j.seares.2010.05.003

Haas LW (1977) **The effect of the spring-neap tidal cycle on the vertical salinity structure of the**

James, York and Rappahannock Rivers, Virginia, U.S.A. *Estuar Coast Mar Sci*, 5(4), 485-496.

Haidvogel DB, Arango H, Budgell WP, Cornuelle BD, Curchitser E, Di Lorenzo E, ... & Levin J (2008) **Ocean forecasting in terrain-following coordinates: Formulation and skill assessment of the Regional Ocean Modeling System.** *J Comput Phys*, 227(7), 3595-3624.

Hill AE, Brown J, Fernand L, Holt J, Horsburgh KJ, Proctor R, Raine R, Turrell WR (2008) **Thermohaline circulation of shallow tidal seas.** *Geophys Res Lett*, 35, 105–5. https://doi.org/10.1029/2008GL033459.

Holling, C. S. (July 1959). **"Some characteristics of simple types of predation and parasitism"**. *The Canadian Entomologist*. 91 (7). pp.385–98.doi:10.4039/Ent91385-7

Hawkins, A. J. S., Duarte, P., Fang, J. G., Pascoe, P. L., Zhang, J. H., Zhang, X. L. & Zhu, M. Y. (2002). **A functional model of responsive suspension-feeding and growth in bivalve shellfish, configured and validated for the scallop Chlamys farreri during culture in China.** Journal of *Experimental Marine Biology and Ecology,* 281(1–2), 13 40. https://doi.org/10.1016/s0022-0981(02)00408-2

Hwang, J. H., Van, S. P., Choi, B. J., Chang, Y. S., & Kim, Y. H., 2014. **The physical processes in the Yellow Sea.** *Ocean & coastal management*, *102*, 449-457.

Ichikawa, H., & Beardsley, R. C., 2002. **The current system in the Yellow and East China Seas.** *Journal of Oceanography*, *58*(1), 77-92.

Inglis, G.J., Hayden, B.J., Ross, A.H., 2000. **An overview of factors affecting the carrying capacity of coastal embayments for mussel culture.** *NIWA Client Report CHC00/69*, Christchurch, New Zealand.

IPCC, 2014: Climate change 2014: Impacts, Adaption, and Vulnerability. Part B: Regional Aspects. Contribution of Working Group II to the Fifth Assessment Reoport of the Intergovernmental Panel on Climate Change [Barros, et al. (eds.)]. *Cambridge University Press, Cambridge, United Kingdom and New York, NY, USA, 688 pp.*

Jiang W, Li JQ, Gao YP, Mao YZ, Jiang ZJ, Du MR, Zhang Y, Fang JG (2016) **Effects of temperature change on physiological and biochemical responses of Yesso scallop, *Patinopecten yessoensis***. *Aquaculture*, 451, 463–472. https://doi.org/10.1016/j.aquaculture.2015.10.012.

Jiang W, Lin F, Fang J, Gao Y, Du M, Fang J, Li W, Jiang Z (2018a) **Transcriptome analysis of the Yesso scallop, *Patinopecten yessoensis* gills in response to water temperature fluctuations.** *Fish Shellf Immun,* 80, 133–140.

Jiang W, Du M, Fang J, Gao Y, Mao Y, Chen Q, Lin F, Jiang Z (2018b) **Response of Yesso scallop *Patinopecten yessoensis* to acute temperature challenge: physiological and biochemical parameters.** *J Oceanology Limnol.* https://doi.org/10.1007/s00343-019-7245-7.

Johnsen, I.A., Fiksen, Ø., Sandvik, A.D., Asplin, L., 2014. **Vertical salmon lice behaviour as a response to environmental conditions and its influence on regional dispersion in a fjord system.** *Aquacult. Environ. Interact. 5*, 127–141. doi:10.3354/aei00098

Kluger LC, Filgueira R, Byron CJ (2019) **Using media analysis to scope priorities in social carrying capacity assessments: a global perspective.** *Marine Policy* 99: 252–261.

Lentz, S.J., 1992. **The surface boundary layer in coastal upwelling regions.** *Journal of Physical Oceanography*, 22, 1517-1539.

Li, C. L., & Zhai, W. D., 2018. **Decomposing monthly declines in subsurface-water pH and aragonite saturation state from spring to autumn in the North Yellow Sea.** *Continental Shelf Research.*

Li, H., and Y. Yuan, 1992: **On the formation and maintenance mechanisms of the cold water mass of the Yellow Sea.** *Chinese Journal of Oceanology and Limonology*,**10**(2), 97–106.

Li, H., Xiao, T., Ding, T., & Lü, R., 2006. **Effect of the Yellow Sea Cold Water Mass (YSCWM) on distribution of bacterioplankton.** *Acta Ecologica Sinica*, *26*(4), 1012-1019.

Li M, Zhong L (2009) **Flood–ebb and spring–neap variations of mixing, stratification and circulation in Chesapeake Bay,** *Cont Shelf Res*,15: 4-14.

Liang, X.S., Huang, M., Wu, H., Wang, Y., 2018. **The Yellow Sea Surface Cold Patches in Warm Seasons. In: Liang, X.S., Zhang, Y. (eds)** *Coastal Environment, Disaster, and Infrastructure: A Case Study of China's Coastline,* 27-45, http://dx.doi.org/10.5772/intechopen.80732

Lin F, Asplin L, Budgell WP, Wei H, Fang J (2019) **Currents on the northern shelf of the Yellow Sea.** *Reg Stud Mar Sci,* 32, 100821. https://doi.org/10.1016/j.rsma.2019.100821.

Liu Jinlin, Xia Jing, Zhuang Minmin, He Peimin, Sun Yuqing, Tong Yichao, Zhao Shuang, Zhang Jianheng, 2021. **Golden seaweed tides accumulated in Pyropia aquaculture areas are becoming a normal phenomenon in the Yellow Sea of China,** *Science of The Total Environment*, 2021, 145726, ISSN 0048-9697, https://doi.org/10.1016/j.scitotenv.2021.145726.

Lu, J., Huang, L., Xiao, T., Jiang, Z. & Zhang, W. (2015). **The effects of Zhikong scallop (Chlamys farreri) on the microbial food web in a phosphorus-deficient mariculture system in Sanggou Bay, China.** *Aquaculture*, 448(C), 341 349. https://doi.org/10.1016/j.aquaculture.2015.06.021

Madsen, O.S., 1977. **A realistic model, of the wind-induced Ekman boundary layer.** *Journal of Physical Oceanography*, 7, 248-255.

Mao, Y., Lin, F., Fang, J., Fang, J., Li, J., Du, M., 2019. **Bivalve Production in China.** In: Smaal A., Ferreira J., Grant J., Petersen J., Strand Ø. (eds) *Goods and Services of Marine Bivalves*. Springer.

McKindsey, C.W., Thetmeyer H., Landry, T., Silver,t W. (2006) **Review of recent carrying capacity models for bivalve culture and recommendations for research and management.** *Aquaculture* 261(2): 451–462.

McKindsey, C.W. (2013) **Carrying capacity for sustainable bivalve aquaculture.** In: Christou P, Savin R, Costa-Pierce B, Misztal I, Whitelaw B (eds) **Sustainable Food Production**, pp. 449–466. Springer, New York, NY.

Milewski, I. (2001). **Impacts of salmon aquaculture on the coastal environment: a review**. In MF Tlusty, DA Bengston, HO Halvorson, SD Oktay, JB, Pearce and RB Rheault Jr.,(eds). Marine aquaculture and the environment: A meeting for stakeholders in the Northeast. Cape Cod Press, Falmouth, MA (pp. 166-197).

NACA. 1989. **Integrated Fish Farming in China. NACA Technical Manual 7**. A World Food Day Publication of the Network of Aquaculture Centres in Asia and the Pacific, Bangkok, Thailand. 278 pp.

Nunes, J. P., Ferreira, J. G., Gazeau, F., Lencart-Silva, J., Zhang, X. L., Zhu, M. Y. & Fang, J. G. (2003). **A model for sustainable management of shellfish polyculture in coastal bays.** *Aquaculture*, 219(1–4), 257 277. https://doi.org/10.1016/s0044-8486(02)00398-8

Pollard, R.T., Rhines, P.B., Thompson, R.O.R.Y, 1973. **The deepening of the wind-mixed layer.** *Geophysical Fluid Dynamics*, 4, 381-404.

Pouvreau, S., Bourles, Y., Lefebvre, S., Gangnery, A., Alunno-Bruscia, M. (2006). **Application of a dynamic energy budget model to the Pacific oyster, Crassostrea gigas, reared under various environmental conditions** *Journal of Sea Research* 56(2), 156-167. https://dx.doi.org/10.1016/j.seares.2006.03.007

Qi, J., Guo,C., Yang,D., Xu, Z., Yin, B., 2013. **3-D Numerical Simulation of tidal field near Zhangzi island, NE China.** *Oceanologia et Limnologia Sinica*, 44(6), 1469-1478. (in Chinese with English abstract).

Radach G, and Moll A. **Estimation of the variability of production by simulating annual cycles of phytoplankton in the central North Sea.** *Prog. Oceanog.* 1993.31: 339-419. https://doi.org/10.1016/0079-6611(93)90001-T.

Reid, G., Lefebvre, S., Filgueira, R., Robinson, S., Broch, O., Dumas, A., Chopin, T. (2018). **Performance measures and models for open-water integrated multi-trophic aquaculture** *Reviews in Aquaculture* 293(357), 211 30. https://dx.doi.org/10.1111/raq.12304

Ren, J., Stenton-Dozey, J., Plew, D., Fang, J., Gall, M. (2012). **An ecosystem model for optimising production in integrated multitrophic aquaculture systems** *Ecological Modelling* 246(), 34 46. https://dx.doi.org/10.1016/j.ecolmodel.2012.07.020

Ren, J., Schiel, D. (2008). **A dynamic energy budget model: parameterisation and application to the Pacific oyster Crassostrea gigas in New Zealand waters** *Journal of Experimental Marine Biology and Ecology* 361(1), 42 48. https://dx.doi.org/10.1016/j.jembe.2008.04.012

Rongjun, W. U., Xuelei, Z., Mingyuan, Z., & Youfei, Z.. (2009). **A model for the growth of haidai(laminaria japonica) in aquaculture**. *Marine Science Bulletin.* 28(02):34-40.(in Chinese with English abstract)

Robertson, R., Hartlipp, P., 2017. **Surface wind mixing in the Regional Ocean Modeling System (ROMS).** *Geoscience Letters*, 4:24. DOI: 10.1186/s40562-017-0090-7.

Ross LG, Telfer TC, Falconer L, Soto D, Aguilar-Manjarrez J, Asmah R et al. (2013) **Carrying capacities and site selection within the ecosystem approach to aquaculture.** In: Ross LG, Telfer TC, Falconer L, Soto D, Aguilar-Manjarrez J (eds) Site Selection and Carrying Capacities for Inland and Coastal Aquaculture, pp. 19–46. *FAO*, Rome, Italy.

S. A. L. M. Kooijman. **Dynamic Energy Budget theory for metabolic organisation.** *Cambridge*

University Press, 2010. https://doi.org/10.1017/CBO9780511805400

Sandvik, A.D., Skagseth, Ø., Skogen, M.D., 2016. **Model validation: Issues regarding comparisons of point measurements and high-resolution modeling results.** *Ocean Modelling 106*, 68–73. doi:10.1016/j.ocemod.2016.09.007

Shchepetkin, A. F., & McWilliams, J. C., 2005. **The regional oceanic modeling system (ROMS): a split-explicit, free-surface, topography-following-coordinate oceanic model.** *Ocean modelling*, *9*(4), 347-404.

Shi, J., Wei, H., Zhao, L., Yuan, Y., Fang, J., Zhang, J. (2011). **A physical–biological coupled aquaculture model for a suspended aquaculture area of China** *Aquaculture* 318(3-4), 412 424. https://dx.doi.org/10.1016/j.aquaculture.2011.05.048

Shi, F., Luo, Y., Rong, Z., 2016. **A numerical study of the summer circulation in the southwestern Yellow Sea.** *Acta Oceanol. Sin. 35*, 1–8. doi:10.1007/s13131-016-0943-5

Shi, H., Zheng, W., Zhang, X., Zhu, M. & Ding, D. (2013). **Ecological–economic assessment of monoculture and integrated multi-trophic aquaculture in Sanggou Bay of China.** *Aquaculture*, 410, 172–178. https://doi.org/10.1016/j.aquaculture.2013.06.033

Shumway S.E., Parsons G.J. (2016) (Editors) **Scallops: Biology, Ecology, Aquaculture and Fisheries**, 3rd ed. *Developments in Aquaculture and Fisheries Science*, Elsevier Science. Oxford.

Simpson JH, Hunter JR (1974) **Fronts in the Irish Sea.** *Nature*, 250, 404–406. https://doi.org/10.1038/250404a0.

Simpson, J.H., Crisp, D.J., Hearn, C., 1981. **The Shelf-Sea Fronts: Implications of their Existence and Behaviour [and Discussion].** *Philosophical Transactions of the Royal Society A: Mathematical, Physical and Engineering Sciences 302*, 531–546. doi:10.1098/rsta.1981.0181

Steele, J. H., (2003) **ENVIRONMENTAL CONTROL OF PHOTOSYNTHESIS IN THE SEA.** *Limnology and Oceanography*, **7, doi:** https://doi.org/10.4319/lo.1962.7.2.0137.

Steeves LE, Filgueira R, Guyondet T, Chassé J, Comeau L. (2018) **Past, present, and future: performance of two bivalve species under changing environmental conditions.** Front. Mar. Sci. 5:184.

Strand Ø, Brynjeldsen E (2003) **On the relationship between low winter temperatures and mortality of juvenile scallops, *Pecten maximus* L., cultured in western Norway**. *Aquacult Res*, 34: 1417-1422.

Su, J., and D. Huang (1995), **On the current field associated with the Yellow Sea Cold Water Mass,** *Oceanol. Limnol. Sin.*, 26, suppl., 1– 7.

Sun, Y. J., & Cho, Y. K., 2010. **Tidal front and its relation to the biological process in coastal water.** *Ocean Science Journal*, *45*(4), 243-251.

Sun, Ke., Zhang, Jihong., Lin, Fan, Jeffrey S Ren, Zhao, Yunxia, Wu, wenguang, Liu, Yi. (2020). **Evaluating the influences of integrated culture on pelagic ecosystem by a numerical approach: A case study of Sungo Bay, China.** *Ecol Model* **415**, 108860 (2020).

Tak, Y. J., Cho, Y. K., Seo, G. H., & Choi, B. J., (2016). **Evolution of wind-driven flows in the Yellow Sea during winter.** *Journal of Geophysical Research: Oceans*, *121*(3), 1970-1983.

Tett P, Portilla E, Gillibrand PA, Inall M (2011) **Carrying and assimilative capacities: the ACExR-LESV model for sea-loch aquaculture.** *Aquaculture Research* 42(1): 51–67.

UNEP (2005). Teng, S.K., Yu, H., Tang, Y., Tong, L., Choi, C.I., Kang, D., Liu, H., Chun, Y., Juliano, R.O., Rautalahti-Miettinen, E. and D. Daler. **Yellow Sea, GIWA Regional assessment 34**. University of Kalmar,Kalmar, Sweden.

Wang, B., Hirose, N., Kang, B., & Takayama, K., 2014. **Seasonal migration of the Yellow Sea bottom cold water.** *Journal of Geophysical Research: Oceans*, *119*(7), 4430-4443.

Warner, J. C., Sherwood, C. R., Arango, H. G., & Signell, R. P. (2005). **Performance of four turbulence closure models implemented using a generic length scale method.** *Ocean Modelling*, *8*(1-2), 81-113.

Wei, H., Shi, J., Lu, Y., & Peng, Y., 2010. **Interannual and long-term hydrographic changes in the Yellow Sea during 1977–1998.** *Deep Sea Research Part II: Topical Studies in Oceanography*, *57*(11-12), 1025-1034.

Wei, H., Shi, J., Lu, Y. & Peng, Y. **Interannual and long-term hydrographic changes in the Yellow Sea during 1977–1998.** *Deep Sea Res Part Ii Top Stud Oceanogr* 57, 1025 1034 (2010).

Weitzman, J. & Filgueira, R. (2020). **The evolution and application of carrying capacity in aquaculture: towards a research agenda.** *Reviews in Aquaculture*, 12(3), 1297–1322. https://doi.org/10.1111/raq.12383

Whitmarsh D., Palmieri M.G. (2008) **Aquaculture in the Coastal Zone: Pressures, Interactions and Externalities.** In: Holmer M., Black K., Duarte C.M., Marbà N., Karakassis I. (eds) *Aquaculture in the Ecosystem*. Springer, Dordrecht https://doi.org/10.1007/978-1-4020-6810-2_8

Wu, X., Cahl, D., Voulgaris, G., 2018. **Effects of Wind Stress and Surface Cooling on Cross-Shore Exchange.** *Journal of Physical Oceanography,* 48, 2627-2647. DOI:10.1175/JPO-D-17-0216.1

Warner JC, Sherwood CR, Arango HG, Signell RP (2005) **Performance of four turbulence closure models implemented using a generic length scale method.** *Ocean Model*, 8(1-2), 81-113.

Xia, C., F. Qiao, M. Zhang, Y. Yang, and Y. Yuan (2004a), **Simulation of double cold cores of the 35°N section in the Yellow Sea with a wave-tide-circulation coupled model**, *Chin. J. Oceanol. Limnol.*, 22, 292– 298.

Xia, C., Qiao, F., Yang, Y., Ma, J., Yuan, Y., 2006. **Three-dimensional structure of the summertime circulation in the Yellow Sea from a wave-tide-circulation coupled model.** *Journal of Geophysical Research: Oceans 111*, 297. doi:10.1029/2005JC003218

Xiao J, Ford S, Yang H, Zhang G, Zhang F, Guo X (2005) **Studies on mass summer mortality of cultured zhikong scallops (*Chlamys farreri* Jones et Preston) in China.** *Aquaculture*, 250(3-4), 602-615. https://doi.org/10.1016/j.aquaculture.2005.05.002.

Xin, M., Ma, D., & Wang, B., 2015. **Chemicohydrographic characteristics of the Yellow Sea cold water mass.** *Acta Oceanologica Sinica*, *34*(6), 5-11.

Xinyou, L., Xiao-Hai, Y., Yuwu, J., Zhenchang, Z., 2016. **Performance assessment for an operational ocean model of the Taiwan Strait.** *Ocean Modelling 102*, 27–44. doi:10.1016/j.ocemod. 2016.04.006

Xuan, J., He, Y., Zhou, F., Tang, C., Zheng, X., Liu, H., Yu, L., Chen, J. (2019). **Aquaculture-induced boundary circulation and its impact on coastal frontal circulation** *Environmental Research Communications* 1(5), 051001. https://dx.doi.org/10.1088/2515-7620/ab22cd

Yuze, Mao., Jiaqi, Li., Suyan, Xue., Fan, Lin., Zengjie, Jiang., Jianguang, Fang., Qisheng, Tang. (2018). **Ecological functions of the kelp Saccharina japonicain integrated multi-trophic aquaculture, Sanggou Bay, China** *Acta Ecologica Sinica* 38(9), 1 8. https://dx.doi.org/10.5846/stxb201703160444

Yuan Xiutang, Zhang Mingjun, Liang Yubo, Liu Dan, Guan Daoming, 2010. **Self-pollutant loading from a suspension aquaculture system of Japanese scallop (Patinopecten yessoensis) in the Changhai sea area, Northern Yellow Sea of China**, *Aquaculture*, Volume 304, Issues 1–4, 2010, Pages 79-87, ISSN 0044-8486, https://doi.org/10.1016/j.aquaculture.2010.03.026.

Zeng, D., Huang, D., Qiao, X., He, Y. & Zhang, T. (2015). **Effect of suspended kelp culture on water exchange as estimated by in situ current measurement in Sanggou Bay, China.** *Journal of Marine Systems,* 149(C), 14 24. https://doi.org/10.1016/j.jmarsys.2015.04.002

Zhao, Y., Zhang, J., Lin, F., Ren, J. S., Sun, K., Liu, Y., ... & Wang, W., 2019. An ecosystem model for estimating shellfish production carrying capacity in bottom culture systems. Ecological Modelling, 393, 1-11.

Zhu, J., Shi, J., Guo, X., Gao, H., & Yao, X., 2018. **Air-sea heat flux control on the Yellow Sea Cold Water Mass intensity and implications for its prediction.** *Continental Shelf Research*, *152*, 14-26.

Zhuang, Y., Liu, Z. Z., & Zhai, F. G., 2017. **Analysis on continuous current observation in the northern Yellow Sea.** *Oceanologia et Limnologia Sinica*, *48*(4), 703-711.

Zhang, Jihong & Hansen, Pia & Fang, Jianguang & Wang, Wei & Jiang, Zengjie. (2009). **Assessment of the local environnemental impact of intensive marine shellfish and seaweed farming—Application of the MOM system in the Sungo Bay, China.** *Aquaculture.* 287. 304-310. 10.1016/j.aquaculture.2008.10.008.

Zhang, J., Wu, W., Ren, J., Lin, F. (2016). **A model for the growth of mariculture kelp Saccharina japonica in Sanggou Bay, China** *Aquaculture Environment Interactions* 8(), 273 283. https://dx.doi.org/10.3354/aei00171

Zhao, J. & S.L., Zhou & J.G., Fang. (1996). **Research on Sanggou Bay aquaculture hydro-environment.** *Mar. Fish. Res.* 17. 68-79. (in Chinese with English abstract)

Zhao, Y., Zhang, J., Lin, F., Ren, J., Sun, K., Liu, Y., Wu, W., Wang, W. (2019). **An ecosystem model for estimating shellfish production carrying capacity in bottom culture systems** *Ecological*

Modelling 393(Aquat. Living Resour. 16 1 2003), 1-11. https://dx.doi.org/10.1016/j.ecolmodel.2018.12.005

Jihong Zhang, Pia Kupka Hansen, Jianguang Fang, Wei Wang, Zengjie Jiang. (2009) **Assessment of the local environmental impact of intensive marine shellfish and seaweed farming—Application of the MOM system in the Sungo Bay, China** *Aquaculture*, Volume 287, Issues 3–4, https://doi.org/10.1016/j.aquaculture.2008.10.008

Zhang, J., Hansen, P. K., Wu, W., Liu, Y., Sun, ke, Zhao, Y. & Li, Y. (2020). **Sediment-focused environmental impact of long-term large- scale marine bivalve and seaweed farming in Sungo Bay, China.** *Aquaculture*, 528, 735561. https://doi.org/10.1016/j.aquaculture.2020.735561

Zhaohui Zhang, Fangyuan Qu, Shouqiang Wang. (2019) **Sustainable development of the Yellow Sea Large Marine Ecosystem**, *Deep Sea Research Part II: Topical Studies in Oceanography*,Volume 163,2019, Pages 102-107,ISSN 0967-0645, https://doi.org/10.1016/j.dsr2.2018.08.009.

Zheng, W., Shi, H., Fang, G., Hu, L., Peng, S. & Zhu, M. (2012). **Global sensitivity analysis of a marine ecosystem dynamic model of the Sanggou Bay**. *Ecological Modelling,* 247, 83 94. https://doi.org/10.1016/j.ecolmodel.2012.08.003

Zhou JH (2012) **Preliminary Study on Structure and Characteristic of Yesso Scallop Industry in LiaoNing.** *The Ocean University of China Master dissertation (in Chinese).*

Ziegeler, S.B., Dykes, J.D., Shriver, J.F., 2012. **Spatial Error Metrics for Oceanographic Model Verification.** *Journal of Atmospheric and Oceanic Technology* 29, 260–266. doi:10.1175/JTECH-D-11-00109.1

Regional Studies in Marine Science 32 (2019) 100821

Contents lists available at ScienceDirect

Regional Studies in Marine Science

journal homepage: www.elsevier.com/locate/rsma

Currents on the northern shelf of the Yellow Sea

Fan Lin [a,b,d], Lars Asplin [c,*], W. Paul Budgell [c], Hao Wei [e], Jianguang Fang [a,b]

[a] Yellow Sea Fisheries Research Institute, CAFS, Qingdao, China
[b] Laboratory for Marine Fisheries Science and Food Production Processes, Qingdao National Laboratory for Marine Science and Technology, China
[c] Institute of Marine Research, Norway
[d] Geophysical Institute, University of Bergen, Norway
[e] School of Marine Science and Technology, Tianjin University, Tianjin, China

ARTICLE INFO

Article history:
Received 21 August 2018
Received in revised form 19 July 2019
Accepted 30 August 2019
Available online 5 September 2019

Keywords:
Northern Yellow Sea shelf
Tide
Wind driven current
Thermal front
Front jet

ABSTRACT

The currents of the northern shelf of the Yellow Sea are investigated using observations of current and hydrography and numerical current model results. The Regional Ocean Model System (ROMS) with a horizontal resolution about 1km is implemented for the Yellow Sea and the Bohai Sea, and the results are produced for the year 2014 and 2015. Observations from bottom moored ADCP profilers and CTD on the northern shelf of the Yellow Sea are used for validation of the model. The comparison of current time series and bottom temperature evolution show good agreement between model and observation. Barotropic tides are the dominant current component throughout the year on the shelf and consistently mixing the water column in the shallower parts. A thermal front and associated jet exists during the summer creating a robust current structure on the western part of the shelf. The winds in the region are changing constantly creating episodic currents in the upper part of the sea lasting from hours to a couple of days.

1. Introduction

This study aims at investigating the currents at the northern shelf of the Yellow Sea (YS). This refers to the coastal water south of the Liaodong Peninsula towards Korea Bay including the Zhangzidao Islands. The bottom depths are shallower than 40–50 m. This area has great importance for aquaculture of especially bottom cultured scallops (Mao et al., 2019). According to the Chinese Fishery Statistical Yearbook 2018, Liaoning province have produced about 472,230 metric tons of cultured scallops, which accounts for about 23% of the total domestic production. The bottom cultured scallops usually take about 3 years to grow up to market level, and recent frequent high scallop mortality within this region has drawn more attention for researchers to studies of ecology and carrying capacity (Zhao et al., 2019). Regarding the sustainable development of the scallop industry on the northern shelf of YS, the understanding of the physical environmental variation and the related driving forces will be crucial.

The Yellow Sea at large is relatively thoroughly investigated. As a semi-enclosed sea in the Western Pacific, surround by the mainland of China and the Korean peninsula, it covers an area of approximately 40,000 km^2 with an average depth of about 44 m (Wei et al., 2010). Recent overviews by Hwang et al. (2014) and Tak et al. (2016) illustrates the general forcing and responses of the water masses in the Yellow Sea. Other studies have illustrated the water masses, especially the Yellow Sea Bottom Cold Water, and general circulation (Li and Yuan, 1992; Su and Huang, 1995; Ichikawa and Beardsley, 2002; Xia et al., 2006; Wang et al., 2014; Zhu et al., 2018). The thermal fronts on the shelves are of particular interest, and is commented in e.g. Liang et al. (2018) and in studies illustrating that these can have a major effect on the phytoplankton growth and biological production (Chen, 2009; Li et al., 2006; Xin et al., 2015; Sun and Cho, 2010).

The conditions at the northern shelf have received less focus, although similarities with other shelf areas around the Yellow Sea are apparent. Zhuang et al. (2017) analyzed the tidal and mean current characteristics with moored current profiling data near Zhangzidao island during June-November in 2009. They found a barotropic diurnal and semi-diurnal tide at the observation location and that the summer stratification has an impact on the vertical structure of the residual currents. Qi et al. (2013) implemented a numerical current model based on FVCOM to simulate the tidal current on the northern shelf near Zhangzidao island. The model result and the observation have showed a major regular semi-diurnal pattern around the island with counter-clockwise rotated tidal current. The tidal residual current has been evaluated to be around 0.08–0.12 m/s around the islands and reduced to about 0.01–0.02 m/s further from the coast. Li and Zhai (2018) studied the subsurface-water pH and aragonite saturation from cruise data during 2011–2013, and identified the

* Corresponding author.
E-mail address: lars.asplin@imr.no (L. Asplin).

https://doi.org/10.1016/j.rsma.2019.100821

contributions from various biogeochemical processes within the north YS cold water mass.

In our study, we focus on the most important current components acting on the northern shelf of the Yellow Sea. We use information from observations by current meters and CTD-sondes when available, although most information is from numerical current modeling and various model results archives. We show that the model results are in good agreement with the available observations. The tidal current is the most important current component in the area. The wind is creating a relatively high frequent current confined to the upper ∼10 m with periods or unidirectional flow being hours to a few days. A frontal jet associated with the temperature distribution on the shelf is apparent in late summer and capable of moving water of the same order of magnitude as the whole water mass of the western part of the shelf for that period.

2. Materials and methods

2.1. The current model

The regional Ocean Modeling System (ROMS) is a free surface, terrain following, primitive equations, hydrostatic ocean model on an Arakawa-C grid (Haidvogel et al., 2008; Shchepetkin and McWilliams, 2005). ROMS is widely used in coastal studies, e.g. along the Norwegian coast (Albretsen et al., 2012). Our implementation of the ROMS for the Yellow Sea is named the Yellow Sea Model (YSM). The YSM covers the Yellow Sea and Bohai Sea with the horizontal grid size being latitude by longitude (∼1 km), and there are 40 vertical layers derived with the stretching factors 7.0, 2.0 and a minimum depth of 15 m giving enhanced resolution near the surface and the bottom. The model grid is rotated counter-clockwise to have one open boundary towards the border between the Yellow Sea and the East China Sea. The model bathymetry is interpolated from SRTM30-plus shuttle radar altimetry supplemented with side-scan sonar survey data and the GEBCO 30" database (Becker et al., 2009) and smoothed with a low-pass filter (Fig. 1). The model is configured with 3rd-order upstream horizontal advection of tracers and 4th-order centered advection for momentum with the Generic Length Scale k-kl vertical mixing scheme (Warner et al., 2005).

Atmospheric forcing is obtained from the European Center for Medium-Range Weather Forecast ERA-Interim Reanalysis datasets (Dee et al., 2011), including 10 m wind velocity, surface specific humidity (derived from 2 m dew point temperature), surface air temperature (2 m), downward long wave and shortwave radiation, precipitation and mean sea level pressure. Accumulated data such as radiation and precipitation are 12-hourly data with spatial resolution of 0.75°, and the rest are 6-hourly data at spatial resolution of 0.25°. Atmospheric forcing is interpolated to the model grid, and the net heat flux is computed from a bulk formulae by Fairall et al. (1996).

Open boundary data includes tide, daily mean elevations, daily mean vertical momentums, temperature and salinity. The mean values are obtained from the HYCOM daily global ocean reanalysis and were interpolated to the YSM grid. Eleven tidal components (M2, K2, S2, N2, K1, P1, O1, Q1, MN4, M4 and MS4) from the Oregon State University global inverse tidal model of TPXO7.2 (Egbert and Erofeeva, 2002) were specified at the open boundary. Open boundary data are imposed with a radiative-nudging scheme and a quadratic bottom drag was employed with the friction coefficient of 0.0025 applied to the entire model domain.

The model was run for 29 months from August 2013 to December 2015. The initial conditions were interpolated from the HYCOM reanalysis mentioned above. Model results were stored as hourly and daily mean values and are validated against the observed current and temperature.

2.2. The observations

Observations include *in-situ* measurement of current and hydrography. A Nortek ADCP Aquadopp Profiler (1.0 MHz, bin size 1.0 m, 20 bins) was moored at the bottom near the Zhangzidao Island. The accuracy of the instrument is 1% measured value +/−0.5 cm/s for current profiling, +/−0.1 for the integrated temperature sensor and 0.5% of maximum range for the pressure sensor. The instrument was deployed twice at different periods and different locations in 2015 (Fig. 1). First deployment was from March to April and the second from September to December. The instrument was moored at the sea floor and measuring upwards with a range of approximately 20 m. Instrument depths were 52 m in the first period (ADCP A) and 39 m in the latter (ADCP B). The bottom temperature and pressure time series were recorded with integrated sensors.

On July 8th, 2015, nine stations of vertical temperature profiles were measured with a Seabird SBE 19plus V2 profiler CTD. Geographical locations of the measurement sites are shown in Fig. 1. The initial accuracy the CTD is 0.005 for temperature and 0.1% full scale range for pressure sensor.

3. Results

The total current at a location will be assembled as a sum of current components from specific forcing agents plus potentially some non-linear contributions. Usually it is meaningful to analyze currents based on individual components created by the separate forcing mechanisms like tide and wind etc., which is what we do in the following.

3.1. The tidal current

The tidal current at the northern shelf is strong with an amplitude in surface elevation of around 2 m. A number of tidal constituents are identified as active, but the main is the semidiurnal M2 component from the moon. A total of 11 constituents are included at the open boundary of the numerical model simulation.

Horizontal current components from the current meter locations near the Zhangzidao island (ADCP A and B) at approximately 10 m above the bottom show a good agreement between observed and modeled current (Fig. 2) with values varying between +/−0.4–0.6 m/s. The correlation coefficient for the modeled and observed u and v component at ADCP A and ADCP B are 0.92, 0.96, 0.94 and 0.97 respectively. The corresponding root-mean-square errors are 0.08 m/s, 0.07 m/s, 0.07 m/s and 0.10 m/s for each component. The largest root-mean-square error for the presented time series is about 19% of the observation maximum value. In general, the numerical model results resemble the observations realistically. The velocity basically follows the spring–neap cycle of the tidal period. The maximum current magnitude is larger at ADCP B, i.e. at a shallower depth closer to the coast. In the model, the u component is slightly underestimated and the v component, on the contrary, is slightly overestimated.

The tidal ellipses extracted from time series of the numerical model results illustrates a variety of eccentricities, from high (flat) to low (circular), typically determined by the topography (Fig. 3). In areas near islands and the coast the tidal motion will be more back and forth, while at the open shelf the tidal ellipses are less eccentric.

If we compute the tidal ellipse from the M_2 constituent horizontal flow in the vertical, we will discover any baroclinicity. A baroclinic tidal signal will be possible if the water column is stratified, and we will present results from three locations T1–T3 (Fig. 1) where T1 is offshore and in a stratified water mass, T2

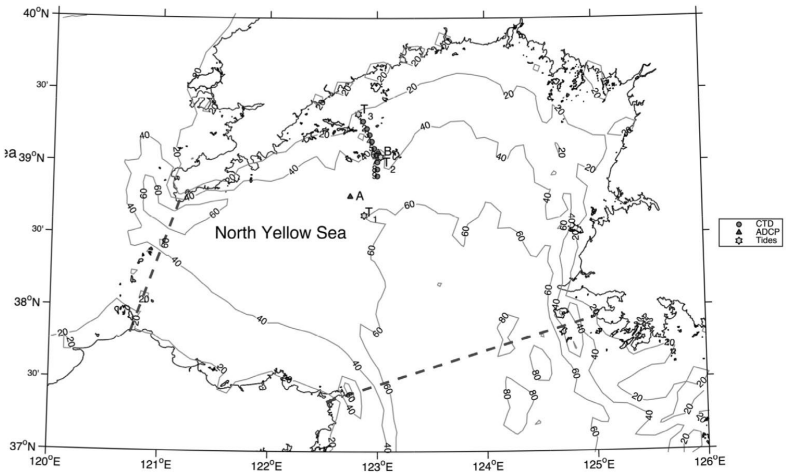

Fig. 1. The northern shelf of the Yellow Sea and the locations of the observations (blue triangles for current observations, red dots for ctd profiles) and the locations for extraction of vertical tidal ellipses (green stars). (For interpretation of the references to color in this figure legend, the reader is referred to the web version of this article.)

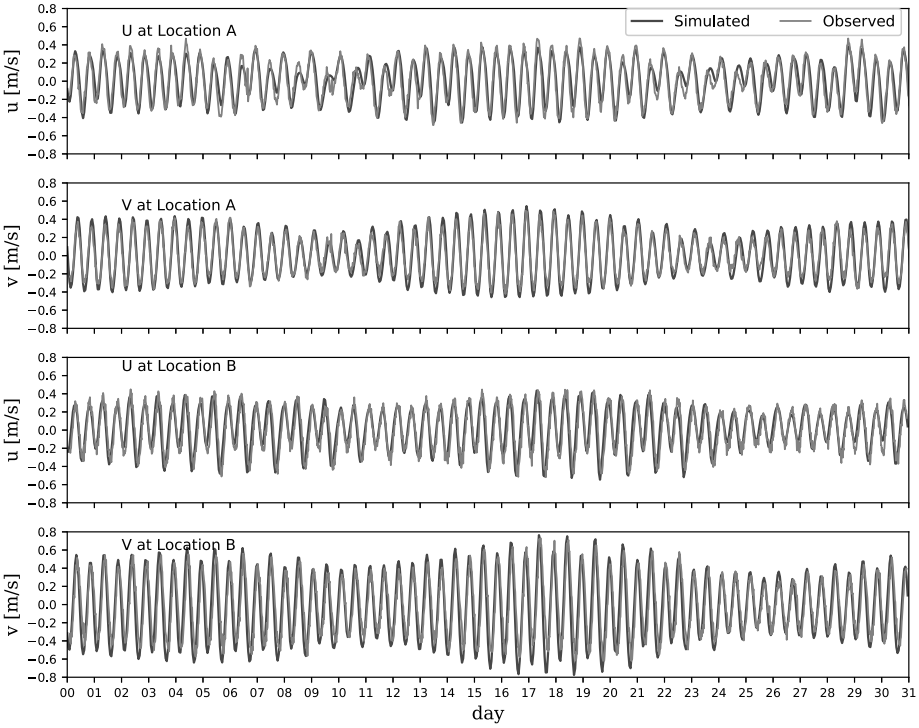

Fig. 2. Observed (red line) and modeled (blue line) current components (m/s) at the locations ADCP A (March 2015) and ADCP B (October 2015).. (For interpretation of the references to color in this figure legend, the reader is referred to the web version of this article.)

is weakly stratified and T3 nearly homogeneous. We will show results from both summer season and winter season, where the latter represents homogeneous water at all three locations. The stratification is mainly due to vertical variation of water temperature (Fig. 4). The tidal ellipses show little vertical variation for the two innermost locations T2 and T3 both in winter and

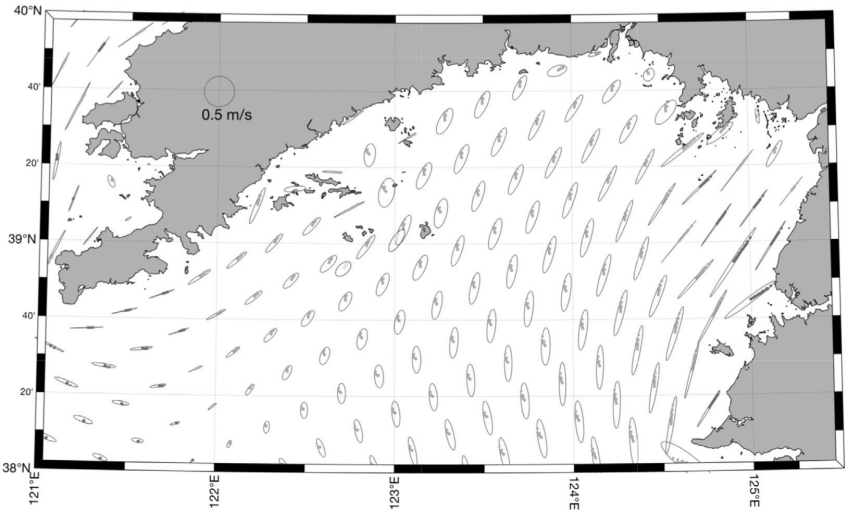

Fig. 3. Tidal ellipses on the northern shelf of the Yellow Sea for the M_2 constituent from the numerical model results. The arrow inside the ellipses indicate current direction for the same phase (red color indicates anticyclonic rotation, blue color cyclonic rotation). The tidal ellipses derived from depth averaged observed velocity is shown in red for the two current meter locations ADCP A and B near the Zangzidao islands. (For interpretation of the references to color in this figure legend, the reader is referred to the web version of this article.)

summer, while at the offshore location T1 there is a reduction in the upper 10–20 m during summer when there is a two layered water column. For all locations there is a reduction of ellipse size towards the bottom due to bottom friction.

3.2. Seasonality of water temperature and the thermal front jet

Observations and numerical model results from the locations of ADCP A and B (locations shown in Fig. 1) illustrate the annual cycle of water temperature at a single point (Fig. 5). Minimum water temperature appears in the early spring and maximum in late autumn. At these locations the minimum value is around 3–4 °C and maximum around 18–20 °C. The observed water temperature is in agreement with the numerical model results with a correlation coefficient and root-mean-square error of 0.96 and 0.27 °C at ADCP A and 0.98 and 0.40 °C at ADCP B. Closer to the coast, the maximum summer bottom temperature and minimum winter bottom temperature from the model results are above 25 °C and less that −1.5 °C respectively, indicating a large interannual difference.

To illustrate the warming of the shelf water through the summer season, numerical model results of bottom water temperature are extracted for the days May 1, June 1, July 1, August 1, September 1 and October 1 (Fig. 6). In May most of the bottom water is cold and less than 6–8 °C but the beginning of a warming is seen near the coast. One month later, the water temperature at the shelf has increased to around 15 °C for most areas shallower than 30 m. Such an increase continues through the summer and early autumn, but restricted to depths shallower than ∼40 m at least for the western part of the shelf. In October the bottom water temperature has started to decrease after a maximum in September.

From a vertical section of temperature observation at June 8. 2015 (location in Fig. 1) a thermal front is found around the locations of the 30–40 m isobaths (Fig. 7). The upper warm layer is about 15 m deep and relatively homogeneous with at temperature just above 20 °C. The thermocline of the numerical model is shallower and only ∼5–10 m, but the structure of the surface and bottom thermal front is similar between the two results, as well as the location of the fronts at around the 30–40 m isobaths.

Observations of salinity from the same vertical section indicated little vertical variations and values around 32. The quality of the observations turned out to be poor with much noise, and values are not presented.

Monthly mean values from our numerical model results of current at 20 m depth illustrate the evolution of a frontal jet system along the shelf (Fig. 8). The strongest flow appears in August and September with an almost continuous jet from the longitude of 123 °E extending about 200 km westward to the tip of the Liaoning Peninsula.

A closer look on the vertical structure of the jet along a cross section stretching south-south east offshore starting at 122 °E for August 25th, 2015 shows a strong bottom thermal front, a weaker surface front and a jet flowing westward (into the page, negative values) extending vertically down to 30–40 m depth (Fig. 9). The width of the jet is ∼40 km but the core is only ∼20 km wide. The internal radius of deformation at this latitude and based on the present vertical density stratification is ∼5 km. The jet does not extend all the way to the bottom, although the iso-therms are forming a distinct bottom front.

3.3. Wind driven current

Calculating mean winds for 2014 and 2015 for the two seasons extracted from the ERA archive we find that the summer circulation and winter circulation differ with southerly and relatively weak mean wind in the months May to August and stronger northerly mean wind during September to April (Fig. 10).

The wind driven currents are created by wind episodes of shorter duration, and to examine this we have extracted a time series of the wind component in the North-South direction approximately at the location of the ADCP A current meter at the southern part of the shelf (Fig. 11). The values are from January 2011 until March 2016 and are based on 3 hourly winds from the

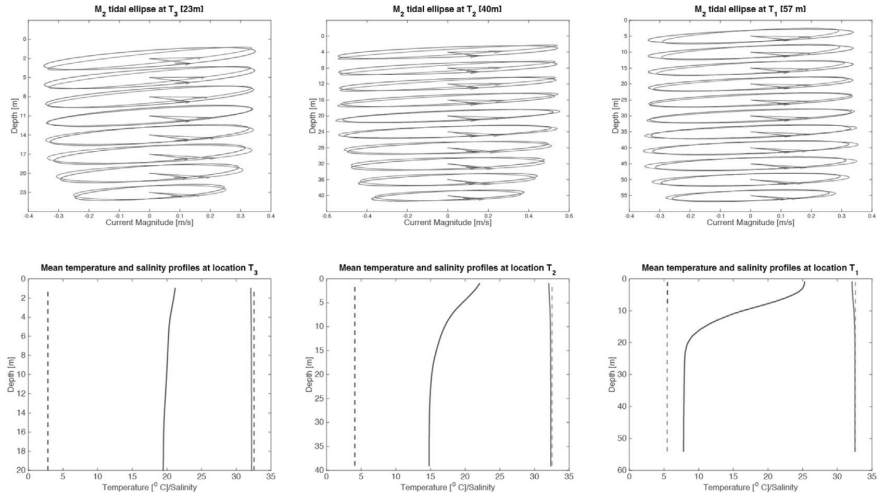

Fig. 4. Vertical distribution of tidal ellipses from the M_2 constituent horizontal flow for three locations T1, T2 and T3 (locations shown in Fig. 1) with corresponding vertical temperature (°C) and salinity profiles in the lower panels. In the upper panels the red color illustrate results for the summer period and blue results for the winter period. In the lower panels, solid lines are results for the summer period and dashed lines results for the winter period. (For interpretation of the references to color in this figure legend, the reader is referred to the web version of this article.)

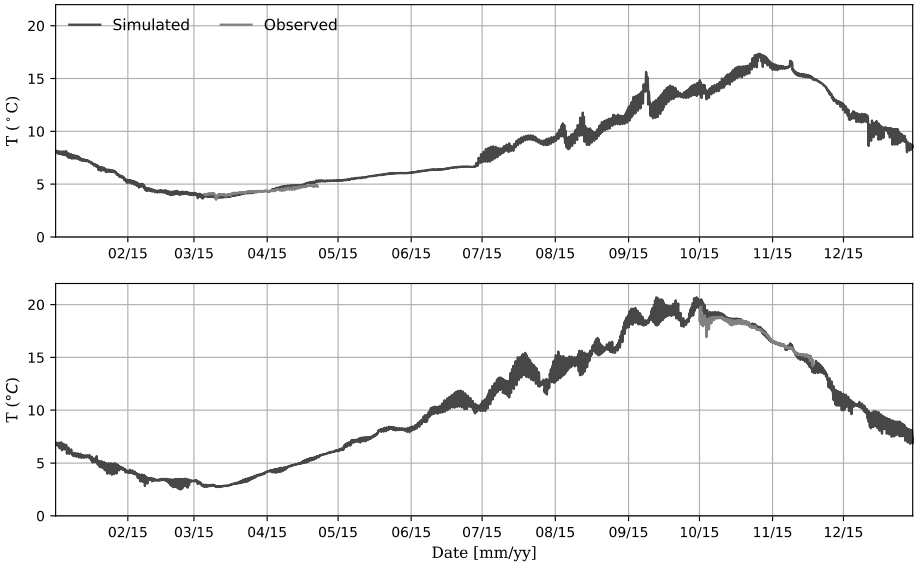

Fig. 5. Water temperature (°C) near the bottom at the location ADCP A (top) and ADCP B (bottom) for January to December 2015. The blue line represents the numerical model results while the red line is observations by the current meter. (For interpretation of the references to color in this figure legend, the reader is referred to the web version of this article.)

Table 1
Values from the ERA-Interim atmospheric archive at the ADCP A location of the north-south component of the wind at 10 m height.

	Episodes	Mean duration	Max duration	Mean speed	Max speed
Northerly	175	13 h	60 h	5.1 m/s	19.2 m/s
Southerly	28	8 h	30 h	3.7 m/s	12.7 m/s

ERA archive. The seasonality with southerly winds during summer (positive NS component) and northerly during the winter is apparent. Maximum values are above 10 m/s in both directions. There are not many periods of calm winds, but an on-going

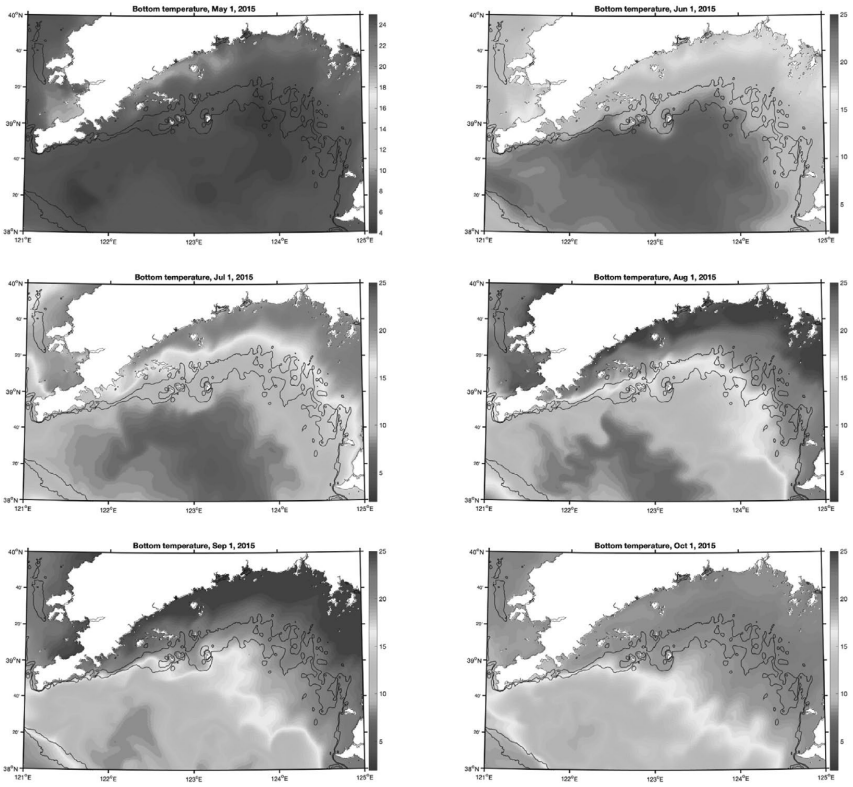

Fig. 6. Evolution of the bottom temperature (°C) between May 1 and Oct 1, 2015, from model results. The contour lines of 30 and 40 m depths are shown.

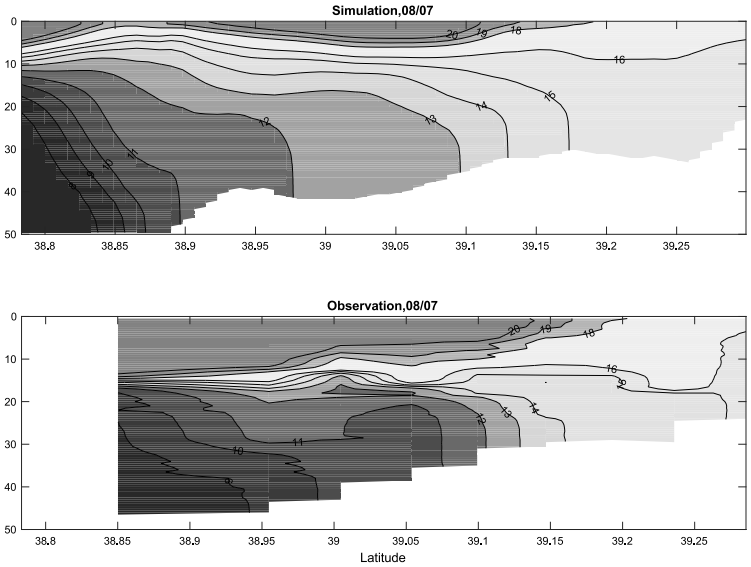

Fig. 7. Along section of temperature (°C) on June 8, 2015, from the numerical model results (top) and observations (bottom).

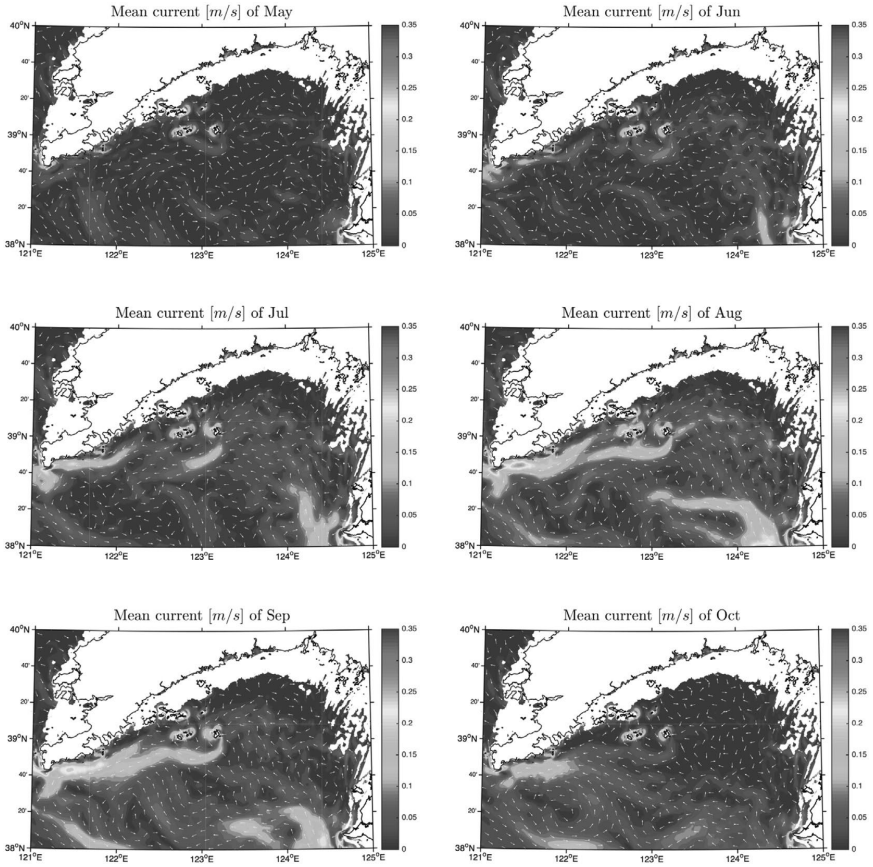

Fig. 8. Monthly mean current (m/s) at 20 m depth from the numerical model results for May to October, 2015.

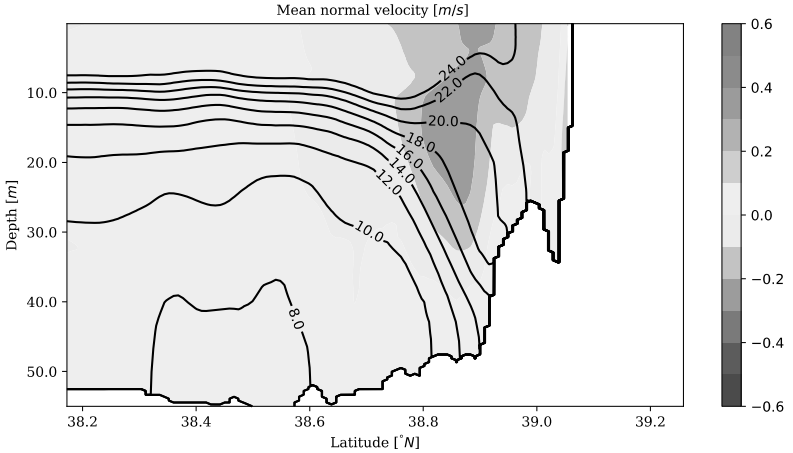

Fig. 9. Vertical view of the daily mean velocity (color) across the section and the temperature (contours) along the section on August 25th, 2015. (For interpretation of the references to color in this figure legend, the reader is referred to the web version of this article.)

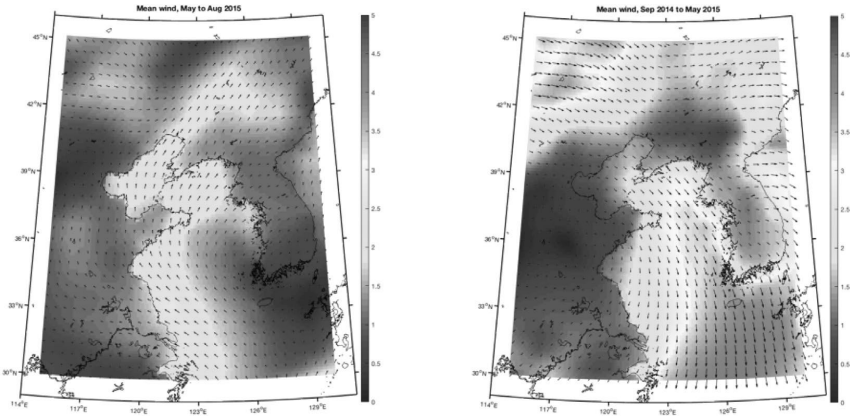

Fig. 10. Mean winds (m/s) for the summer period (left) and the winter (right) extracted from the ERA-Interim 3 hourly wind archive.

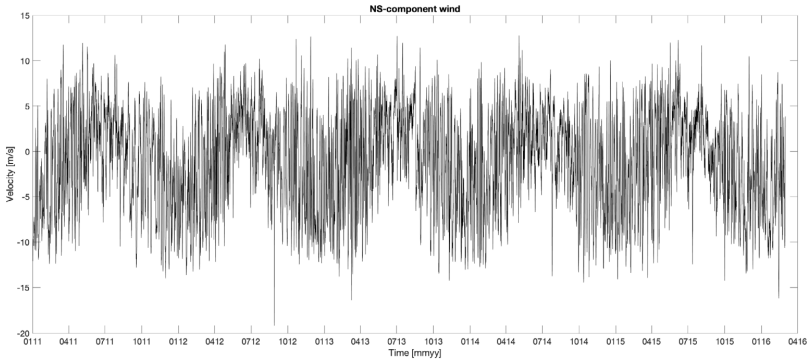

Fig. 11. North-South component of wind (m/s) at 10 m from the ERA-Interim archive at the location of the ADCP A current meter.

fluctuation of episodes. Maximum wind speeds are moderate and never reaching a value to be classified as a storm.

If we count the duration of the episodes with absolute wind value larger than 10 m/s, we find that this occur about 7 times more frequent for winds from the north (winter) than from the south (summer) (Table 1). Northerly winds with speed larger than 10 m/s occur 175 times during the ∼5 years period and the mean duration of such episodes is 13 h and maximum duration 60 h. This indicates such an episode almost weekly. The similar numbers for winds from south are 28 episodes, lasting on average 8 h and with maximum duration of an episode being 30 h.

To illustrate the effect of a wind episode on the current, we choose a situation from March 31, 2015, when there was a northerly wind lasting for ∼20 h. The situation on March 31 at 12 o'clock shows a northerly wind covering the northern part of the Yellow Sea and even stronger in the Bohai Sea (Fig. 12). The corresponding surface current after a 24 h lowpass filter (4th order Butterworth) has been used to remove the main tide, is westward and with speed between 0.1 and 0.2 m/s with higher values towards the west on the shelf (Fig. 13).

If we look at a time series of the surface current components at the location of the ADCP A current meter between March 30 and April 3, 2015, we find that the east–west current component on March 31 adds on to the tide to create a surface current of more than 0.4 m/s (Fig. 14). The 24 h lowpassed current component, mainly consisting of the wind driven part, is westward with a maximum current speed of ∼0.17 m/s. On April 2 the wind direction changes to more southerly, and another episode with current towards north-east is created. Later the same day and the next, a southerly current is apparent again. The absolute value of the lowpassed surface current has a maximum of around 0.2 m/s.

The vertical profile of lowpass filtered current speed illustrates the vertical extension of the wind driven flow component (Fig. 15). For the three times where we have identified different wind episodes, i.e. March 31, April 2 and April 3, 2015, the current speed has maximum around 0.2 m/s at the surface and is rapidly decreasing downwards to approximately 20 m depth.

3.4. Particle dispersion

In order to illustrate the water mass transport capacity of the different current components, a simple particle dispersion calculation has been performed. We have chosen four time periods where two periods consist of mainly wind driven flow component, one period with mainly tidal flow component and one period with the thermal front jet component. Particles are seeded one in each grid square and advected with the current without additional dispersion. We use 121 particles and let them drift horizontally for 25 h (Fig. 16). For the wind driven flow experiments, March 31 and April 1, 2015 are used, and we use 24 h lowpassed current. In the first period the particles drift initially to the west and then to the north. The net movement

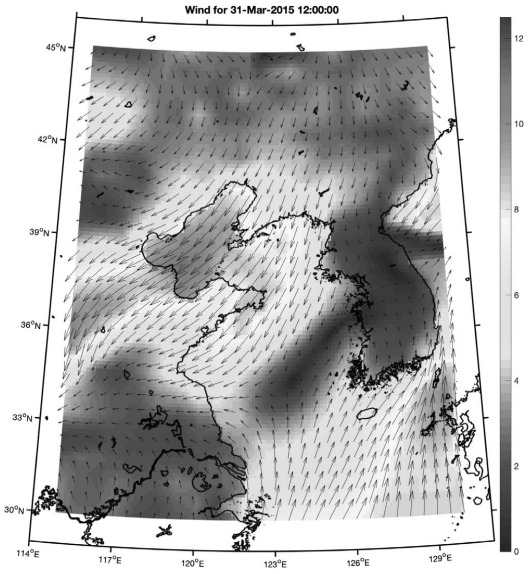

Fig. 12. Wind (m/s) at 10 m height from the ERA-Interim archive on March 31. 2015, at 12 h.

of the particles are 5–10 km in 25 h. Particles seeded on April 1 are subject to a current generated by a northerly wind, and will drift towards the south and with a net dispersion distance also of 5–10 km. The third period illustrates the particle dispersion by the tidal flow, and we subtracted the 24 h lowpassed current from the total current with the main tidal flow remaining. We have also chosen a period with a relatively strong tidal flow with current amplitude of approximately 0.5 m/s. During the 25 h drift, the net movement of the particles are modest while the total drift is much larger with the maximum distance of the particles away from the initial location being 5–10 km. For the dispersion of the particles by the thermal front jet, we have chosen September 1–2, 2015, and the 24 h lowpassed filtered current at 20 m depth. The particle dispersion for those captured in the relatively narrow jet is stable towards the west, and after 48 h around 30 km is covered.

4. Validation of the numerical model results

Numerical current model results validation is an exercise that should be as extensive as possible and also one that never ends (Dee, 1995). A numerical current model might perform good while standard statistical error metrics as root-mean-square or cross-correlation still can be large (Ziegeler et al., 2012). The Yellow Sea Model is implemented from the ROMS current model which has been extensively applied for coastal seas worldwide, e.g. the NorKyst800 model system for the Norwegian coast (Albretsen et al., 2012) or TFOR for the Taiwan Strait (Xinyou et al., 2016). These implementations has proven to produce realistic results and useful applications (Asplin et al., 2013; Johnsen et al., 2014; Sandvik et al., 2016; Xinyou et al., 2016).

The horizontal current speed at 10 m above the bottom is in good agreement with the independent observations (least correlation coefficient is 0.92 and largest rms error is 0.10 m/s). The 20 m measurement range of the ADCP limits the observations to the lower part of the water column, where the tidal flow is dominating. Potential erroneous bathymetry in the model can be responsible for the small deviations in both modeled elevations and currents compared to the observations. Improving the bottom depth in the model domain will be important when developing the model further.

Model results of temperature distribution resembles the observations in both variability on longer and shorter time scales. For the temporal development of temperature measured by the current meters (Fig. 5), the least correlation coefficient is 0.96 and the largest root-mean-square error is about 0.40 °C.

We find that the numerical model underestimates the mixed surface layer (Fig. 7), which is previously reported for the ROMS model and the GLS turbulence formulation (Robertson and Hartlipp, 2017). To simulate the mixing of the upper layer water masses and the sharp transitions is generally challenging for numerical models. The action of surface waves, which is not included in the model, might also represent a mixing agent of

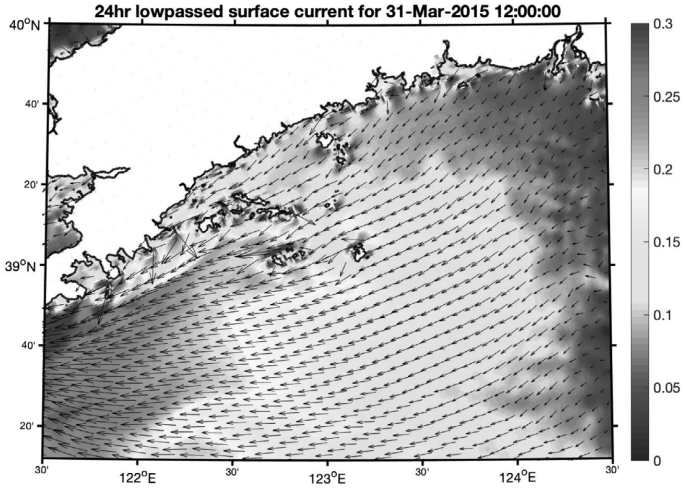

Fig. 13. 24 h low-pass filtered surface current (m/s) from the numerical model results on March 31, 2015 at 12 h.

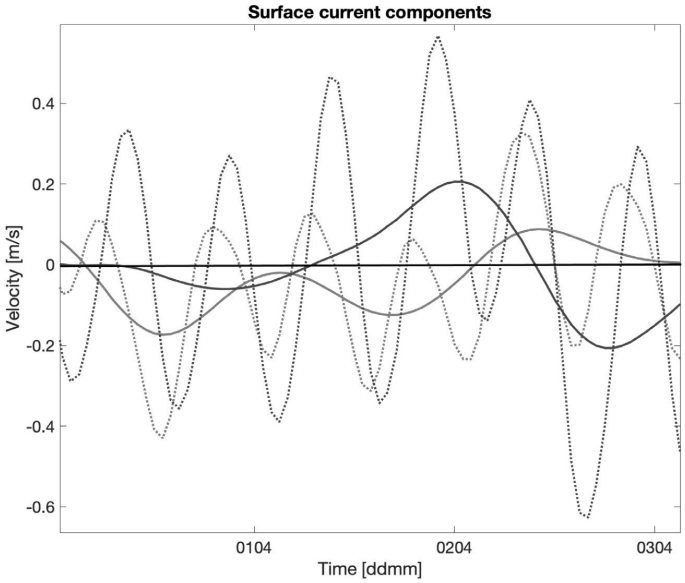

Fig. 14. Time series of the components of the surface current (m/s; EW = red lines, NS = blue lines) at the location of ADCP A from the numerical model results between March 30 and April 3, 2015. Solid lines show the 24 h low-passed values. (For interpretation of the references to color in this figure legend, the reader is referred to the web version of this article.)

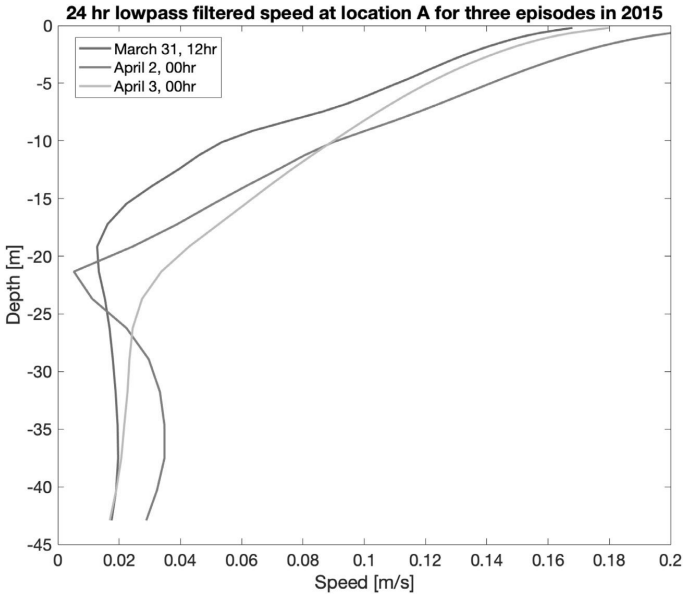

Fig. 15. Vertical profile of 24 h lowpassed current speed (m/s) for three time periods at the location of ADCP A.

importance and one possible explanation of an underestimated mixed layer depth. Still in spite of a slightly misplaced thermocline, the frontal structure and the lateral position of the bottom and surface fronts are reasonably reproduced (Fig. 7).

An advantage with numerical model results is the huge temporal and spatial information provided. The more details included in the model results, the more likely is a small offset in time and space. Since all motion in the ocean is assembled by numerous waves with potentially different phase velocities and amplitudes, as well as an in principle chaotic sub-grid scale turbulent motion, small errors in the numerical simulation and parameterization of these can lead to small displacements, typically as seen in

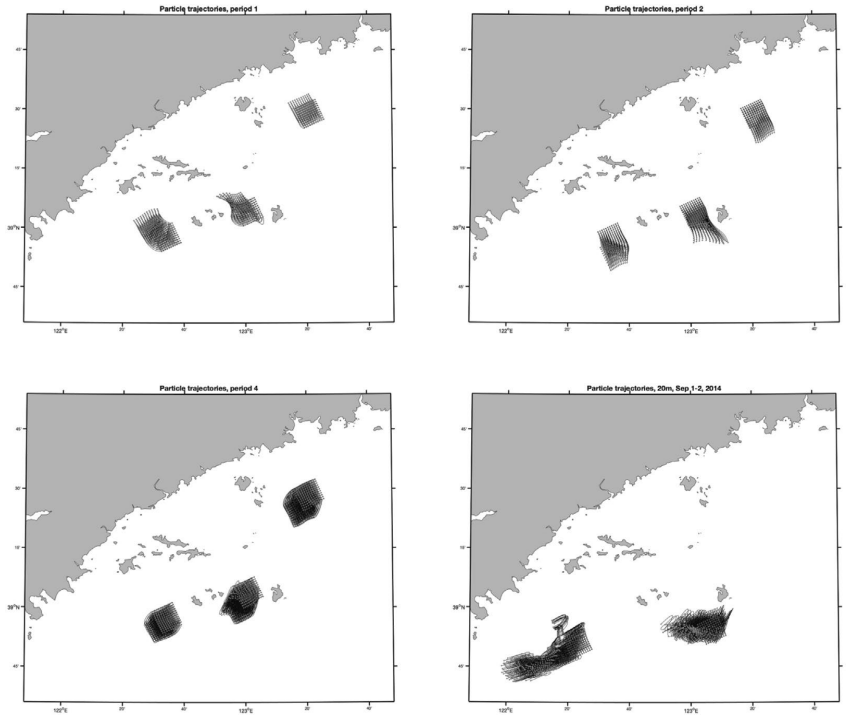

Fig. 16. Trajectories of particles dispersed in the horizontal current at four different episodes. Upper left panel shows 25 h drift on April 1, 2015, with a south-easterly wind episode dominating the lowpassed surface current. Upper right panel shows 25 h of drift om April 2, 2015, and a northerly wind episode. Lower left panel shows trajectories of 25 h drift using the tidal current during a spring tide period and lower right panel shows trajectories from 25 and 48 h drift of particles at 20 m depth on September 1–2, 2015, using 24 h lowpassed current illustrating the effect of the thermal front jet on dispersion. The blue dots represent the initial particle location and the red dots the locations after 25 h drift. The magenta dots represents locations after 48 h drift. (For interpretation of the references to color in this figure legend, the reader is referred to the web version of this article.)

the present comparison between the model results and the observations. Overall, we find that the numerical model delivers a reasonably adequate set of results resembling the same variability as the available observations, and the results will prove useful as information to explore the dynamics and the ecosystems of the Yellow Sea.

5. Discussion

The Yellow Sea is of great ecological importance for marine fishery and the huge aquaculture along its coast, and the northern shelf is an important area for scallop aquaculture (Mao et al., 2019). To understand variability of both natural and farmed ecosystems, it is crucial to understand the variability of the environmental conditions. Water temperature determine the physiology of living organisms and water current determine food availability, water exchange and potential dispersion of diseases. We have investigated the currents of the northern shelf of the Yellow Sea using mainly results from a current model with additional information from a few observations. The observations are a necessary supplement to validate the model results while the latter give us a sufficient information to understand the huge spatial and temporal variability going on.

The tidal current is strong and the dominating current component in the area. The semi-diurnal component is the strongest, meaning the flow will be high frequent and unidirectional for less than 6 h at a time. We find the tidal current to be mostly barotropic, but in the stratified deeper parts there is a minor change of the size of the ellipses vertically (Fig. 4).

We are satisfied with the fact that the model results by and large resembles the observed tides, including the sea surface height (results not shown) since this current component supplies most of the energy to the area.

Around the islands in the western part of the shelf, there will be strong influence on the tidal current from the topography (Qi et al., 2013), but our numerical model set up with 1 km grid resolution is not designed to fully confirm this although our model results (not shown) have an intensified circulation around these islands.

The thermal front jet is a seasonal current system occurring only in the late summer (Fig. 8). The mechanism is similar to what described by Simpson and Hunter (1974) and Simpson (1981) from the Irish Sea, where the surface buoyancy input and the tidal mixing is controlling the water column structure with a front being established at a critical bottom depth. From studies at the northwest European shelf, Hill et al. (2008) found a thermal-wind, geostrophically balanced jet along the front. Xia et al. (2006), Shi et al. (2016) and Liang et al. (2018) showed similar frontal jets on shelf areas in the Yellow Sea, and our results agree with these reports.

Being forced by a thermal wind relation at the thermal front, the front jet is a persistent feature and a geostrophic balance is a preferred state of the nature and the way to spend the minimum energy (Gill, 1982). This current will be limited to the area of the

thermal front though, extending only 20–40 km across (Fig. 9). The shelf area inside of the thermal front, e.g. where the water column is vertically mixed, is not directly affected by this current. The strong tidal current moves the whole shelf water mass back and forth within mainly the M_2 tidal period (∼12.4 h) including the front. However, this movement will mainly be along the front in the area where it is at the strongest, i.e. south-west of the Zangzidao islands (Fig. 3).

The vertical temperature structure of the water column reveals both a surface temperature front and a bottom front similar to what is reported from the northwest European shelf (Hill et al., 2008). They especially highlighted the importance of the bottom temperature front, and on the northern shelf of the Yellow Sea with an extensive bottom aquaculture of e.g. scallops, water temperature and its variations will affect the organism growth. Thus, a precise description of such temperature variations is important in ecosystem models.

We expect the thermal front to be affected by various instability mechanisms, forced by tide, wind or surface heat flux (e.g. Wu et al., 2018). Such instabilities, waves or meandering is beyond the scope for the present work.

The wind driven current will be strongest at the surface and have a logarithmic (i.e. rapid) decrease towards the depth. The duration and strength of the winds determine the strength of the current. Vertically the wind driven current is limited as shown by the classical Ekman theory (Ekman, 1905) with the magnitude of the vertical turbulence coefficient determining the limiting Ekman depth. Typically an Ekman depth is in the range 10–30 m (e.g. Pollard et al., 1973; Madsen, 1977; Stigebrandt, 1985; Lentz, 1992) but the uncertainty is due to the generally unknown turbulence structure. Our model results seems to represent a vertical current structure as anticipated from theory and previous reports (Fig. 15). It is worthwhile to note that a proper description of the strong current shear in the upper few meters require a sufficient number of vertical coordinates, and that the wind driven current component will not directly affect the flow on the deeper parts of the shelf.

The ERA interim atmospheric archive resemble the large-scale atmospheric system in the Yellow Sea area as part of the East Asian monsoon system described in e.g. Hwang et al. (2014). The winds from the ERA-Interim archive reveal conditions on the Northern shelf that are variable, almost always windy and with a strong seasonality, but still with sufficient short time variability that wind driven current episodes of relatively uniform direction will be lasting for only hours to days before changing. Thus, the variability of the wind driven flow is almost on the same periodicity as the tide or slightly longer, and we find that the wind driven flow component in one directions typically is replaced by a similar flow episode hours to a few days later.

The current of the northern shelf of the Yellow Sea is determining the residence time of the water masses. How long the water resides in an area will be important for many reasons, e.g. to determine food availability for bottom cultured scallops, to estimate dispersion of water borne diseases or dilution of pollutants etc. The tide will move and stir water within a radius of 5–10 km (Fig. 16). Thus the tide is less important as a long distance transportations mechanism, but excellent for local transportation and very reliable as a stirring or mixing agent. Similar advection distances for the upper layer water masses due to the wind is also the case, mostly since the winds are not very persistent and rather fluctuate on times from hours to a few days. The thermal front jet on the other hand, is a persistent current and potentially capable of transporting water off the shelf towards the west. This current appears only in late summer so the gross effect might still be limited although seasonally important. With a monthly mean current speed of 0.10–0.15 m/s and the width of the jet being 20–40 km, the capacity of transporting water westward from the shelf is apparent. As an example we consider the shelf area from Dalian and 100 km eastward and 40 km offshore and the upper 30 m of the water column. This volume consist of about 10^{11} m^3 of water. Assuming the thermal front jet to be 20 km wide, 25 m deep and have a mean current speed westward of 0.1 m/s for August and September, the volume transported by this current is also about 10^{11} m^3. Theoretically the thermal jet is then capable of flushing the whole western part of the shelf in the late summer months.

Climate change is an important issue, and the future climate will change also in the Yellow Sea. Parameters like the wind, precipitation/river runoff and temperature might be altered (IPCC, 2014). The various current components on the northern shelf of the Yellow Sea could indirectly be affected, and especially the wind driven current in the case that the atmospheric wind fields change. The tidal current will be unaltered in a climate change, thus the most important current component on the shelf will be less affected. A warming of the water will be on a long spatial scale, but the vertical stratification might change to a warmer surface layer and larger vertical gradient than today. The thermal front will probably remain at the same locations or at a slightly shallower depth contour if the energy needed to vertically mix the water column increases. The speed of the thermal front jet might also alter slightly. However, without any further studies, which apparently should be made, we cannot see now that a possible future climate change will affect the currents dramatically in this area.

6. Concluding remarks

We have implemented a high-resolution current model of the Yellow Sea based on the ROMS model and with an extensive set of forcing and open boundary conditions. The model results compare well with the available observations and we are confident that the information provided by the model will be useful for particularly supplying information of the physical environment to ecological studies.

Although we are satisfied with the model performance per se, improvements should be sought producing even better results. One obvious way to improve the performance is to have a better bottom topography. Usually the forcing of the model is a critical factor for performance, and potentially atmospheric forcing of higher spatial resolution and possibly more precise radiation balance might also improve the results. Testing of internal model constructions as turbulence sub-models (which ROMS has a number to choose from) and the arrangement of the vertical grid, can also make the model perform better. A dynamical coupling to a specific surface wave model will also potentially improve the simulation of the surface mixed layer.

Acknowledgments

The authors sincerely appreciate the support from Sea Ranching Research Center of Zoneco Co Ltd., China, for their help in making observations. This research is jointly funded by the Key Programme for International Cooperation on Scientific and Technological Innovation, Ministry of Science and Technology (2017YFE0118300), the Marine S&T Fund of Shandong Province for Pilot National Laboratory for Marine Science and Technology (Qingdao) (No. 2018SDKJ0502), Youth Talent Program Supported by Laboratory for Marine Fisheries Science and Food Production Processes, Pilot National Laboratory for Marine Science and Technology (Qingdao) (2018-MFS-T13), the Central Public-interest Scientific Institution Basal Research Fund, CAFS (No. 2017GH09) and Modern Agro-industry Technology Research System (CARS-49). This research was also supported by the Research Council of Norway (249056/H30), Environment and Aquaculture Governance, China (MFA, CHN 2152).

References

Albretsen, J., Aure, J., Sætre, R., Danielssen, D.S., 2012. Climatic variability in the Skagerrak and coastal waters of Norway. ICES J. Mar. Sci. 69 (5), 758–763.

Asplin, L., Johnsen, I.A., Sandvik, A.D., Albretsen, J., Sundfjord, V., Aure, J., Boxaspen, K.K., 2013. Dispersion of salmon lice in the Hardangerfjord. Mar. Biol. Res. 10, 216–225. http://dx.doi.org/10.1080/17451000.2013.810755.

Becker, J.J., Sandwell, D.T., Smith, W.H.F., Braud, J., Binder, B., Depner, J.L., et al., 2009. Global bathymetry and elevation data at 30 arc seconds resolution: SRTM30_PLUS. Mar. Geod. 32 (4), 355–371.

Chen, C.T.A., 2009. Chemical and physical fronts in the Bohai, Yellow and East China seas. J. Mar. Syst. 78 (3), 394–410.

Dee, D.P., 1995. On-line estimation of error covariance parameters for atmospheric data assimilation. Mon. Weather Rev. 123 (4), 1128–1145.

Dee, D.P., Uppala, S.M., Simmons, A.J., Berrisford, P., Poli, P., Kobayashi, S., et al., 2011. The ERA-interim reanalysis: Configuration and performance of the data assimilation system. Q. J. R. Meteorol. Soc. 137 (656), 553–597.

Egbert, G.D., Erofeeva, S.Y., 2002. Efficient inverse modeling of barotropic ocean tides. J. Atmos. Ocean. Technol. 19 (2), 183–204.

Fairall, C.W., Bradley, E.F., Rogers, D.P., Edson, J.B., Young, G.S., 1996. Bulk parameterization of air-sea fluxes for tropical ocean-global atmosphere coupled-ocean atmosphere response experiment. J. Geophys. Res. Oceans 101 (C2), 3747–3764.

Gill, A.E., 1982. Atmosphere-Ocean Dynamics. Academic Press, New York, p. 662.

Haidvogel, D.B., Arango, H., Budgell, W.P., Cornuelle, B.D., Curchitser, E., Di Lorenzo, E., et al., 2008. Ocean forecasting in terrain-following coordinates: Formulation and skill assessment of the regional ocean modeling system. J. Comput. Phys. 227 (7), 3595–3624.

Hill, A.E., Brown, J., Fernand, L., Holt, J., Horsburgh, K.J., Proctor, R., Raine, R., Turrell, W.R., 2008. Thermohaline circulation of shallow tidal seas. Geophys. Res. Lett 35, 1–5. http://dx.doi.org/10.1029/2008GL033459.

Hwang, J.H., Van, S.P., Choi, B.J., Chang, Y.S., Kim, Y.H., 2014. The physical processes in the Yellow Sea. Ocean Coast. Manage. 102, 449–457.

Ichikawa, H., Beardsley, R.C., 2002. The current system in the Yellow and East China seas. J. Oceanogr. 58 (1), 77–92.

IPCC, 2014. Climate change 2014: Impacts, adaption, and vulnerability. Part B: Regional aspects. In: Barros, et al. (Eds.), Contribution of Working Group II to the Fifth Assessment Reoport of the Intergovernmental Panel on Climate Change. Cambridge University Press, Cambridge, United Kingdom and New York, NY, USA, p. 688.

Johnsen, I.A., Fiksen, Ø., Sandvik, A.D., Asplin, L., 2014. Vertical salmon lice behaviour as a response to environmental conditions and its influence on regional dispersion in a fjord system. Aquacult. Environ. Interact. 5, 127–141. http://dx.doi.org/10.3354/aei00098.

Lentz, S.J., 1992. The surface boundary layer in coastal upwelling regions. J. Phys. Oceanogr. 22, 1517–1539.

Li, H., Xiao, T., Ding, T., Lü, R., 2006. Effect of the Yellow Sea cold water mass (YSCWM) on distribution of bacterioplankton. Acta Ecol. Sin. 26 (4), 1012–1019.

Li, H., Yuan, Y., 1992. On the formation and maintenance mechanisms of the cold water mass of the Yellow Sea. Chinese J. Oceanol. Limnol. 10 (2), 97–106.

Li, C.L., Zhai, W.D., 2018. Decomposing monthly declines in subsurface-water pH and aragonite saturation state from spring to autumn in the north Yellow Sea. Cont. Shelf Res.

Liang, X.S., Huang, M., Wu, H., Wang, Y., 2018. The Yellow Sea surface cold patches in warm seasons. In: Liang, X.S., Zhang, Y. (Eds.), Coastal Environment, Disaster, and Infrastructure: A Case Study of China's Coastline. pp. 27–45. http://dx.doi.org/10.5772/intechopen.80732.

Madsen, O.S., 1977. A realistic model of the wind-induced Ekman boundary layer. J. Phys. Oceanogr. 7, 248–255.

Mao, Y., Lin, F., Fang, J., Fang, J., Li, J., Du, M., 2019. Bivalve production in China. In: Smaal, A., Ferreira, J., Grant, J., Petersen, J., Strand, Ø. (Eds.), Goods and Services of Marine Bivalves. Springer.

Pollard, R.T., Rhines, P.B., Thompson, R.O.R.Y, 1973. The deepening of the wind-mixed layer. Geophys. Fluid Dyn. 4, 381–404.

Qi, J., Guo, C., Yang, D., Xu, Z., Yin, B., 2013. 3-D numerical simulation of tidal field near Zhangzi island, NE China. Oceanol. Limnol. Sin. 44 (6), 1469–1478 (in Chinese with English abstract).

Robertson, R., Hartlipp, P., 2017. Surface wind mixing in the regional ocean modeling system (ROMS). Geosci. Lett. 4, 24. http://dx.doi.org/10.1186/s40562-017-0090-7.

Sandvik, A.D., Skagseth, Ø., Skogen, M.D., 2016. Model validation: Issues regarding comparisons of point measurements and high-resolution modeling results. Ocean Model. 106, 68–73. http://dx.doi.org/10.1016/j.ocemod.2016.09.007.

Shchepetkin, A.F., McWilliams, J.C., 2005. The regional oceanic modeling system (ROMS): a split-explicit, free-surface, topography-following-coordinate oceanic model. Ocean Model. 9 (4), 347–404.

Shi, F., Luo, Y., Rong, Z., 2016. A numerical study of the summer circulation in the southwestern Yellow Sea. Acta Oceanol. Sin 35, 1–8. http://dx.doi.org/10.1007/s13131-016-0943-5.

Simpson, J.H., 1981. The shelf-sea fronts: implications of their existence and behaviour. Philos. Trans. R. Soc. Lond. A Math. Phys. Eng. Sci. 302, 531–546.

Simpson, J.H., Hunter, J.R., 1974. Fronts in the Irish Sea. Nature 250, 404–406. http://dx.doi.org/10.1038/250404a0.

Stigebrandt, A., 1985. A model for the seasonal pycnocline in rotating systems with application to the Baltic proper. J. Phys. Oceanogr. 15, 1392–1404.

Su, J., Huang, D., 1995. On the current field associated with the Yellow Sea Cold Water Mass. Oceanol. Limnol. Sin. 26 (suppl.), 1–7.

Sun, Y.J., Cho, Y.K., 2010. Tidal front and its relation to the biological process in coastal water. Ocean Sci. J. 45 (4), 243–251.

Tak, Y.J., Cho, Y.K., Seo, G.H., Choi, B.J., 2016. Evolution of wind-driven flows in the Yellow Sea during winter. J. Geophys. Res. Oceans 121 (3), 1970–1983.

Wang, B., Hirose, N., Kang, B., Takayama, K., 2014. Seasonal migration of the Yellow Sea bottom cold water. J. Geophys. Res. Oceans 119 (7), 4430–4443.

Warner, J.C., Sherwood, C.R., Arango, H.G., Signell, R.P., 2005. Performance of four turbulence closure models implemented using a generic length scale method. Ocean Model. 8 (1–2), 81–113.

Wei, H., Shi, J., Lu, Y., Peng, Y., 2010. Interannual and long-term hydrographic changes in the Yellow Sea during 1977–1998. Deep-Sea Res. II 57 (11–12), 1025–1034.

Wu, X., Cahl, D., Voulgaris, G., 2018. Effects of wind stress and surface cooling on cross-shore exchange. J. Phys. Oceanogr. 48, 2627–2647. http://dx.doi.org/10.1175/JPO-D-17-0216.1.

Xia, C., Qiao, F., Yang, Y., Ma, J., Yuan, Y., 2006. Three-dimensional structure of the summertime circulation in the Yellow Sea from a wave-tide-circulation coupled model. J. Geophys. Res. Oceans 111 (297), http://dx.doi.org/10.1029/2005JC003218.

Xin, M., Ma, D., Wang, B., 2015. Chemicohydrographic characteristics of the Yellow Sea cold water mass. Acta Oceanol. Sin. 34 (6), 5–11.

Xinyou, L., Xiao-Hai, Y., Yuwu, J., Zhenchang, Z., 2016. Performance assessment for an operational ocean model of the Taiwan Strait. Ocean Model. 102, 27–44. http://dx.doi.org/10.1016/j.ocemod.2016.04.006.

Zhao, Y., Zhang, J., Lin, F., Ren, J.S., Sun, K., Liu, Y., et al., 2019. An ecosystem model for estimating shellfish production carrying capacity in bottom culture systems. Ecol. Model. 393, 1–11.

Zhu, J., Shi, J., Guo, X., Gao, H., Yao, X., 2018. Air-sea heat flux control on the Yellow Sea cold water mass intensity and implications for its prediction. Cont. Shelf Res. 152, 14–26.

Zhuang, Y., Liu, Z.Z., Zhai, F.G., 2017. Analysis on continuous current observation in the northern Yellow Sea. Oceanol. Limnol. Sin. 48 (4), 703–711.

Ziegeler, S.B., Dykes, J.D., Shriver, J.F., 2012. Spatial error metrics for oceanographic model verification. J. Atmos. Ocean. Technol. 29, 260–266. http://dx.doi.org/10.1175/JTECH-D-11-00109.1.

frontiers in Marine Science

ORIGINAL RESEARCH
published: 17 December 2021
doi: 10.3389/fmars.2021.798504

Summertime M_2 Internal Tides in the Northern Yellow Sea

Fan Lin[1,2,3,4], *Lars Asplin*[3]* *and Hao Wei*[5]

[1] Yellow Sea Fisheries Research Institute, Chinese Academy of Fishery Sciences (CAFS), Qingdao, China, [2] Laboratory for Marine Fisheries Science and Food Production Processes, Qingdao National Laboratory for Marine Science and Technology (QNLM), Qingdao, China, [3] Institute of Marine Research, Bergen, Norway, [4] Geophysical Institute, University of Bergen, Bergen, Norway, [5] School of Marine Science and Technology, Tianjin University, Tianjin, China

The summertime M_2 internal tide in the northern Yellow Sea is investigated with moored current meter observations and numerical current model results. The hydrodynamic model, which is implemented from the Regional Ocean Model System (ROMS) with 1 km horizontal resolution, is capable of resolving the internal tidal dynamics and the results are validated in a comparison with observations. The vertical pattern of a mode-1, semi-diurnal internal tide is clearly captured by the moored ADCP as well as in the simulation results. Spectral analysis of the current results shows that the M_2 internal tide is dominant in the northern Yellow Sea. Analysis of the major M_2 internal tide energetics demonstrated a complex spatial pattern. The tidal mixing front along the Korean coast and on the northern shelf provided proper conditions for the generation and propagation of the internal tides. Near the Changshan islands, the M_2 internal tide is mainly generated near the local topography anomalies with relatively strong current magnitude, equal to about 30% of the barotropic component, thus modifying the local current field. These local internal tides are short-lived phenomena rapidly being dissipated along the propagation pathway, restricting their influence within a few kilometers around the islands.

Keywords: northern Yellow Sea, internal tides, current modification, tidal mixing front, energetics

OPEN ACCESS

Edited by:
Achilleas G. Samaras, Democritus University of Thrace, Greece

Reviewed by:
Hailun He, Second Institute of Oceanography, Ministry of Natural Resources, China
SungHyun Nam, Seoul National University, South Korea

***Correspondence:**
Lars Asplin
lars.asplin@hi.no

Specialty section:
This article was submitted to Coastal Ocean Processes, a section of the journal Frontiers in Marine Science

Received: *20 October 2021*
Accepted: *29 November 2021*
Published: *17 December 2021*

Citation:
Lin F, Asplin L and Wei H (2021) Summertime M_2 Internal Tides in the Northern Yellow Sea. Front. Mar. Sci. 8:798504. doi: 10.3389/fmars.2021.798504

INTRODUCTION

Waves in the ocean are a dominant part of the dynamics. Especially visible are wind driven high frequency surface waves and low frequency tides. Less visible though are internal waves, existing in stratified water masses. However, internal waves are a potential source for ocean mixing and can be important for material transportation. When tidal currents flow over steep topography such as ridges or continental shelf breaks, internal waves with tidal frequency can be generated, known as internal tides. Our present work originates from an observation of currents in the water column near Changshan islands, and the results reveal a clear two-layered oscillation superposed on the strong semi-diurnal tide which characterizes the currents in the region. This internal wave will obviously modify the total current in the area. Knowledge of the currents here is particularly useful since this is an important area for scallop aquaculture.

The Yellow Sea (**Figure 1A**) is the marginal sea between the mainland of China and the Korean peninsula. According to Egbert and Ray (2001), Yellow Sea is estimated to have the most intensive tidal energy dissipation due to friction from shallow topography estimated to be about 150 GW annually. Affected by strong tides and the East Asian monsoon system, the hydrodynamics of the

Yellow Sea have high spatial-temporal variability (Hwang et al., 2014). The competition between the solar radiation induced buoyancy and the endless tidal mixing power, creates the featured summertime "Yellow Sea bottom cold water" (YSBCW) located in the central region of the Yellow Sea surrounded by the tidal mixing front (Lin et al., 2019). The tidal mixing front is usually located between the 20–60 m isobaths with relatively homogeneous water inshore and stratified water offshore (Tana et al., 2017; Zhu et al., 2017; Lin et al., 2019). The stratified waters enable the generation and propagation of baroclinic waves, including the internal tides. Compared to the research conducted in the South China Sea, where the Luzon strait act as a powerful wave generator of internal waves with amplitude up to hundred meters (Jan et al., 2008; Shang et al., 2015; Yan et al., 2020), internal dynamics in the Yellow Sea have been less investigated. For a coastal region with activities such as fishing and aquaculture, knowledge on the coastal circulation and internal tidal-induced hydrodynamics will be important.

Previous literature on the internal tides in the Yellow Sea is mainly derived from observations and mainly for the southern part where the water depth exceeds 80 m, and the stratification is established throughout the year (Lee et al., 2006; Liu et al., 2009; Wei et al., 2013). Liu et al. (2019) have studied the characteristics of the M_2 internal tide in the Yellow Sea at basin scale with a numerical model, concluding with complicated spatial interference wave patterns and strong seasonality. During summer, the M_2 internal tide is generated from multiple sources and the baroclinic kinetic energy is present as the stratification is established around the YSBCW. The major baroclinic energy input is distributed in the southern Yellow Sea near the Yangtze River estuary and the shelf break near Jeju Island. In winter, the spatial coverage of the internal tides usually become very limited (Liu et al., 2019). There were also few reports of the internal tides in the northern Yellow Sea from *in-situ* observations. Guo and Hu (2010) reported the observed regular oscillation of the isotherms at the semi-diurnal frequency off the Qingdao coast, which is originated from the M_2 internal tide. Wang et al. (2020) identified the mode-1, semi-diurnal internal tides with moored current profiler and temperature/conductivity sensors off the coast of Shandong Peninsula and concluded with a significant internal tidal induced cross-shore advection of the coastal mass transport. However, knowledge and data regarding the internal tides on the northern shelf of the Yellow Sea can barely be found.

During the summer of 2017, an RDI ADCP profiling current meter was placed at the bottom on the northern shelf of the Yellow Sea near the Changshan islands (**Figure 1C**). From these observations, a clear mode-1 vertical baroclinic oscillation with a semi-diurnal period was seen, indicating a semi-diurnal internal tide passing the mooring location. In our study, we combined results from a numerical current model and the observations to investigate the dynamics of the M_2 internal tides on the northern shelf of the Yellow Sea in summer (**Figure 1B**). The objective of this study is to clarify the generation, propagation, and dissipation characteristic of the internal tides and to demonstrate their impact on local hydrodynamics in the northern Yellow Sea. We find that the mode-1, semi-diurnal internal tide will increase the total current in the bottom layers in the Changshan islands area where the water masses are stratified during summer. The internal waves are generated locally and with limited regional propagation. The content of this paper is organized as follows: The model setup, observation, and the analysis method are described in section "Materials and Methods." In section "Results," the results including the current observations, the simulated internal tide field, and corresponding energetics, are given. In section "Discussion," the model performance will be evaluated and the internal tidal dynamics in the northern Yellow Sea will be discussed. Finally, a conclusion will be summarized in section "Conclusion."

MATERIALS AND METHODS

Model Setup

The model implemented for this study is based on the Regional Ocean Modeling System (ROMS), which is a free surface, terrain-following, primitive equations, hydrostatic ocean model on an Arakawa-C grid (Shchepetkin and McWilliams, 2005; Haidvogel et al., 2008). A detailed description of the model implementation for the Yellow Sea can be found in Lin et al. (2019). The model covers the Yellow Sea and the Bohai Sea with the horizontal grid size being ∼1 km with 40 vertical layers derived with the stretching factors 7.0 and 2.0, and with a minimum depth of 15 m, giving enhanced resolution near the surface and the bottom. As the horizontal wavelength of internal tides is usually far larger than the water depth on the northern shelf, a hydrostatic model is applicable to resolve the internal tides with the 1 km model horizontal resolution. The model bathymetry is interpolated from SRTM30-plus shuttle radar altimetry supplemented with side-scan sonar survey data and the GEBCO 30" database (Becker et al., 2009). The model is configured with the Generic Length Scale k-kl vertical mixing scheme (Warner et al., 2005).

A full model set up with realistic forcing and boundary conditions was conducted. The atmospheric forcing is taken from the European Centre for Medium-Range Weather Forecast ERA-Interim Reanalysis datasets (Dee et al., 2011), with the net heat flux computed from a bulk formulae by Fairall et al. (1996). The daily mean values of elevation, momentum, water temperature, and salinity were obtained from the HYCOM daily global ocean reanalysis and interpolated to the model grid as open boundary conditions. Eleven tidal components from the Oregon State University global inverse tidal model of TPXO7.2 (Egbert and Erofeeva, 2002) were specified at the open boundary. Open boundary data are imposed with a radiative-nudging scheme and a quadratic bottom drag was employed with the friction coefficient of 0.0025 applied to the entire model domain. A simulation of the period from August 2013 to December 2018 was conducted, and the results from the summertime of 2017 will be used in this study.

Additionally, two simulations were conducted covering the period July–August 2017 in order to investigate the spatial-temporal characteristics of the dominant M_2 internal tide of the northern Yellow Sea. The first is a barotropic simulation with homogeneous water which eliminates the baroclinic component and with the M_2 tide as the only forcing at the open

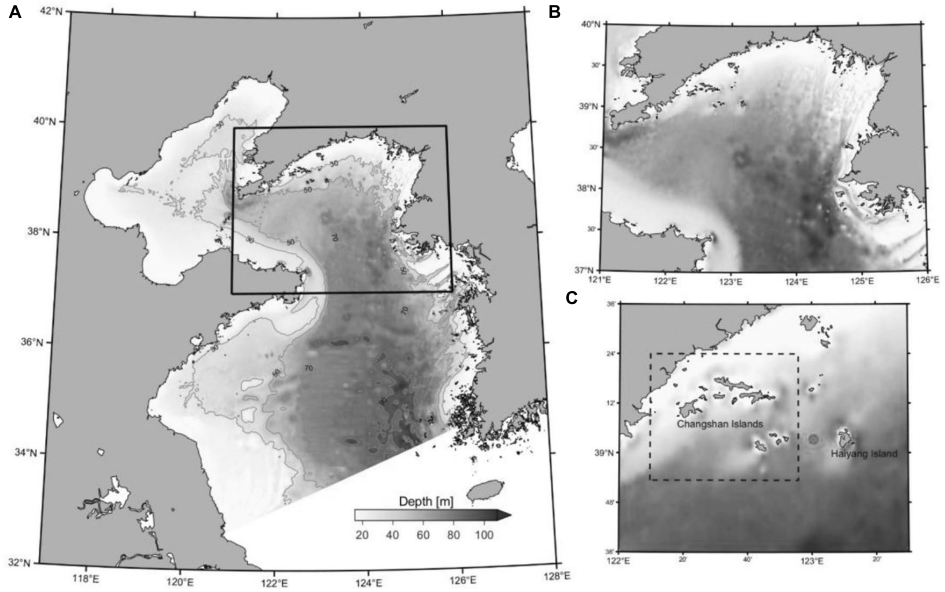

FIGURE 1 | Domain and topography of the Yellow Sea model. **(A)** Model domain covering the Yellow Sea and Bohai Sea. **(B)** Major results will be presented from the northern Yellow Sea where the ADCP mooring site is shown as the red dot in **(C)**. All the subfigures share the same color scale as shown in **(A)**.

TABLE 1 | The configurations of the model simulations used in the study.

Model configuration	Fully forced	M_2 barotropic	M_2 baroclinic
Simulation period	Aug,2013–Dec,2018	Jul–Aug,2017	Jul–Aug,2017
Tidal forcing	11 components TPXO 7.2	M_2 component	M_2 component
Vertical homogeneity	Stratified	Homogeneous	Stratified

boundary. The second simulation is conducted with the same forcing setup but with the monthly mean stratification extracted from the climatological simulation results. The results will be used to demonstrate the internal tidal dynamics. The model configurations are listed in **Table 1**.

Observations

An RDI acoustic doppler current profiler (1.0 MHz, bin size 2.0 m, 20 bins) was moored at the bottom near Changshan islands from July 10 to August 24, 2017. The accuracy of the instrument is 1% measured value $\pm$ 0.5 cm/s for current profiling, $\pm$ 0.1 for the integrated temperature sensor, and 0.5% of maximum range for the pressure sensor. The deployment location is shown in **Figure 1C**. The instrument was moored at the seafloor measuring upwards with a range of about 40 m. The sampling interval was set to 10 min. The water depth at the mooring location is approximately 40 m, and the water pressure time series was recorded with an integrated pressure sensor.

The horizontal baroclinic current velocity $u'(z,t)$ will be extracted from both the observation and simulation results, by subtracting the depth-averaged barotropic component from the total current as:

$$u'(z,t) = u(z,t) - \frac{1}{h}\int_{-h}^{0} u(z,t)\,dz$$

where h is the water depth and $u(z,t)$ is the total velocity. A 4-h lowpass filter is applied to eliminate higher-frequency signals.

Harmonic analysis will be applied to both the barotropic and baroclinic flows to obtain the current ellipses of the M_2 component. Spectral analysis is also applied to the horizontal baroclinic current velocity at different depths to demonstrate the vertical power spectrum distribution.

Generation and Energetics of the Internal Tides

The generation of internal tide requires a stratified water column and a barotropic tide that manages to perturb this stratification. In a situation with a sloping bottom, generation of internal tidal waves from the M_2 constituent can be described by a functional relation between the M_2 tidal wave frequency (ω), the local inertial frequency (the Coriolis parameter, f), the local buoyancy frequency (N), and the local slope of bottom

topography (s, dimensionless) defined as vertical depth change over unit horizontal grid length (Thorpe, 1998; Cacchione et al., 2002). The inertial frequency can be calculated as $f = 2\Omega sin(\varphi)$, where Ω is the angular velocity of Earth rotation and φ is the local latitude. On the northern shelf of the Yellow Sea, the local inertial frequency is within the range of 1.36–1.48 $\times 10^{-5}$ s^{-1}.

A characteristic angle of the M_2 internal tide (β) can be expressed as:

$$\beta = \sqrt{\frac{\omega^2 - f^2}{N^2 - \omega^2}} \quad (1)$$

and the functional relation between this characteristic angle and the topographical slope is calculated as:

$$\gamma = \frac{s}{\beta} \quad (2)$$

A critical slope is when $\gamma < 1$, subcritical for $\gamma = 1$, and supercritical for $\gamma > 1$. In areas around a critical slope, the internal wave beam angle matches the topographic slope and internal tide generation is most favorable. The generated internal waves can propagate to shallower regions with subcritical slope or being reflected at the supercritical slope (Thorpe, 1998; Cacchione et al., 2002).

Liu et al. (2019) have computed the seasonal M_2 internal tide energetics in the whole Yellow Sea using an energy conversion rate (C) from barotropic to baroclinic motion calculated as:

$$C = W \cdot p' \quad (3)$$

where W is the vertical barotropic velocity induced by horizontal barotropic flow over topography:

$$W = -\nabla_H \left[(h + \eta) U_H \right]. \quad (4)$$

Here U_H is the horizontal barotropic flow, h is the bottom depth, and η is the sea surface elevation. In this study, the conversion rate will be calculated with the M_2 baroclinic simulation results, and will be integrated over the water depth and averaged over 32 semi-diurnal tidal cycles in the simulation period from July 26 to August 10, 2017.

The perturbation pressure p' is derived from the perturbation density ρ'. According to the definition of Kang and Fringer (2012), the perturbation density can be calculated as:

$$\rho' = \rho(z, t) - \rho_0 - \rho_b(z) \quad (5)$$

where $\rho(z, t)$ is the time-dependent density of the water column, ρ_0 is the reference density (ρ_0 = 1,000 kg/m^3), and $\rho_b(z)$ is the time-independent background density. The perturbation pressure is then calculated as:

$$p' = g \int_z^{\eta} \rho' dz. \quad (6)$$

In the expression for the energy conversion rate C, a positive value means that W and p' are in phase and the local barotropic energy is transferred to baroclinic energy. A negative value of C may imply a superposition of local and remote internal tides and the barotropic-baroclinic conversion does not happen (Carter et al., 2012; Kang and Fringer, 2012; Masunaga et al., 2017). This metric has been widely used in previous studies to understand the internal tidal dynamics in coastal regions (Kang and Fringer, 2012; Nash et al., 2012; Kumar et al., 2019; Liu et al., 2019).

The depth-integrated baroclinic energy flux can be computed from current model results according to Kang and Fringer (2012) as:

$$F_{bc} = \int_{-h}^{\eta} p' u' dz \quad (7)$$

where u' is the horizontal baroclinic current component. The depth-integrated baroclinic energy flux will also be averaged over 32 semi-diurnal tidal cycles in the simulation period from July 26 to August 10, 2017.

Coherent-Incoherent Analysis of Tidal Waves

According to Nash et al. (2012), a broadband internal tide can be decomposed into two components, (1) the coherent component, which is largely predictable and can be described by a series of tidal frequency sinusoids, and (2) the incoherent component, which is largely unpredictable and associated with intermittent pulses of tidal-band energy that are arriving with different phases and amplitudes. The coherent component of the internal tides is often applied as a parameter to estimate the contribution of local generation from the barotropic tides (Nash et al., 2012; Kumar et al., 2019; Li et al., 2020).

The coherent-incoherent analysis can be applied to time series from, e.g., observations or current model results. The harmonic analysis based on the least-squares method will be used to obtain the semi-diurnal internal tidal currents of the M_2, N_2, S_2 constituents, which will be tested as coherent variables that are phase-locked with the local barotropic tides. A fourth-order Butterworth filter will be applied to extract the baroclinic current of the semi-diurnal frequency band (1.73∼2.13 cpd) from the observation and the simulation results. The coherent internal tidal current is then subtracted, and the remaining signal within the semi-diurnal band can be defined as incoherent.

To demonstrate the baroclinic energy contribution of the locally and remotely generated internal tides, the observed and simulated currents with full forcing were decomposed to coherent and incoherent components of the semi-diurnal tidal constituents M_2, S_2, K_2, and N_2. The horizontal kinetic energy is then computed as KE = $\frac{1}{2}\rho_0 \left[u^2 + v^2\right]$, where u, v are the horizontal velocity component and ρ_0 is the reference density.

RESULTS

Currents Around the Changshan Islands in the Northern Yellow Sea

The measured and modeled horizontal velocities at different depths are shown to basically flow along the coastline isobaths with the major oscillation direction about 30–210 degrees (**Figure 2**). The model results compare reasonably well with the observations in both magnitude and oscillation direction. The observed current magnitudes are 0.69, 0.86, and 0.96 m/s for

the depth of 5, 15, and 30 m, respectively. The corresponding model results are 0.71, 0.91, and 1.08 m/s. The root-mean-square error of observed and simulated currents are 0.09, 0.10, and 0.16 m/s for the presented layers. For both the observation and the simulation, the flow becomes stronger toward the bottom. This vertical structure indicates that the contribution from baroclinic components of the current can be of importance in the mooring region.

The mean density at the surface (**Figure 3a**) and bottom (**Figure 3b**) water for July 2017, illustrates a thermal front approximately located between the 20–60 m isobaths, since in July the water temperature is sufficiently high for the temperature to be the leading factor in the determination of water density. Inshore of this front is homogeneous coastal water and offshore is stratified water (**Figure 3**). The ADCP was moored near the cold/heavy water boundary or the thermal front area. The background stratification enables the propagation of baroclinic waves with frequencies between the local inertial frequency (f) and the buoyancy frequency (N).

To illustrate the vertical structure of the baroclinic flow, the baroclinic current along the major axis 30–210° with the positive values toward 30°is extracted (**Figures 4a,b**). The data from above 10 m is excluded due to the impact of the surface wind. The vertical structure of the measured baroclinic velocity profile is a typical mode-1 plane internal wave with a clear semi-diurnal period, implying a dominating semi-diurnal internal tidal signal. The current model results are comparable to the observation with a similar vertical structure and current magnitude. The amplitudes of both measured and simulated baroclinic currents are around 0.2 m/s, indicating that the baroclinic component speed is comparable to the barotropic.

The observed and simulated M_2 current ellipses of both the barotropic and baroclinic flow are presented in **Figures 5A,B**. The modeled barotropic M_2 tidal ellipse is a bit stretched along the major axis in the numerical model results compared to the observation, but the orientation of the ellipses matches well and is roughly along the isobaths (**Figure 5A**). The magnitude of the barotropic M_2 tidal current is around 0.4 m/s, which is comparable to both the observation and simulation results. **Figure 5B** shows the baroclinic M_2 tidal ellipse distribution for both observation and simulation results. The baroclinic M_2 currents have a nearly opposite phase between the surface and bottom layers, representing the feature of the mode-1 wave. The simulation results reproduce the baroclinic M_2 ellipse for the upper layers, while the current magnitudes are slightly overestimated in the lower layers. The maximum baroclinic M_2 current speed is around 0.1 m/s for both observed and simulated results.

To further investigate the baroclinic currents near the mooring location, the vertical spectra is derived for the water column between 5 and ∼35 m depth (**Figures 6a,b**). The baroclinic vertical spectra computed from the ADCP measurement (**Figure 6a**) is relatively complicated, with various smaller energy contributions at different depths and frequencies. However, for the whole water column, the energy is mainly distributed around the semi-diurnal bandwidth, especially the M_2 tidal frequency. The modeled baroclinic signal (**Figure 6b**) has a similar vertical structure for the whole water column, and the energy is concentrated near the semi-diurnal M_2 component.

The vertically averaged KE of the band-passed barotropic and coherent/incoherent baroclinic tides are presented in **Figures 7A,B** for the current observation. **Figure 7A** illustrates that the barotropic tide is the dominant current component at the mooring location. The variability of the coherent semi-diurnal baroclinic tides is largely correlated with the variability of the barotropic tide, as shown in **Figure 7B**. The incoherent baroclinic KE during the observation period is much weaker compared to the barotropic KE. The time-averaged semi-diurnal barotropic KE is 67 J/m^3 at the mooring site, and the corresponding baroclinic KE is only 4 J/m^3. The energy of the coherent baroclinic tides is also much larger than the incoherent baroclinic tide, and accounts for almost 83% of the total semi-diurnal baroclinic KE. A similar analysis is also applied to the model results (figure not shown). The model overestimates the semi-diurnal barotropic motion, with a time-averaged KE being 80 J/m^3, and the corresponding baroclinic KE is estimated to be 10 J/m^3. The fraction between coherent and incoherent semi-diurnal baroclinic KE is consistent with the observations though, being around 85%.

To demonstrate the impact of the locally generated internal tide on the current field in the region around the Changshan islands, the simulated baroclinic current velocities at different depths are shown in **Figures 8A–D**, together with the barotropic flow shown in **Figures 8E,F**. The current is extracted from the M_2 baroclinic simulation on July 23, with a 6-h time difference between the columns. **Figure 8** clearly shows the M_2 barotropic current is dominant, although the internal tidal current cannot be neglected around the Changshan islands. The statistics of the flow speed are shown in **Table 2**. The internal tidal current is stronger near the islands in the deeper part, close to the generation site (**Figures 8C,D**). Furthermore, there is an apparent direction change of the current, representing an opposite phase of the internal tidal current. The statistics of the current speed at 15 m depth are similar to that of the deeper flows, but the current field is more uniformly distributed for the upper layer (**Table 2** and **Figures 8A,B**). The mean flow speed of the internal tidal current accounts for about 30% of the barotropic current at each presented layer, and the flow modification on the barotropic tide will be more pronounced closer to the islands.

The M_2 Internal Tide in the Northern Yellow Sea

With the summertime stratification and strong tidal current in the northern Yellow Sea, we expect favorable conditions for generation and propagation of internal tides. A measure of where internal tide generation might occur is the slope criticality (γ) for the M_2 internal tide (computed from Equation 2). The spatial distribution of the critical slope values in the northern Yellow Sea is shown in **Figure 9A**. The topographic angle is derived from the model bathymetry, and the near bottom buoyancy frequency is derived and averaged from the modeled density profiles for a tidal period during July 26 to August 10, 2017. The critical slopes (γ = 1) are mostly confined within the isobaths between ∼40

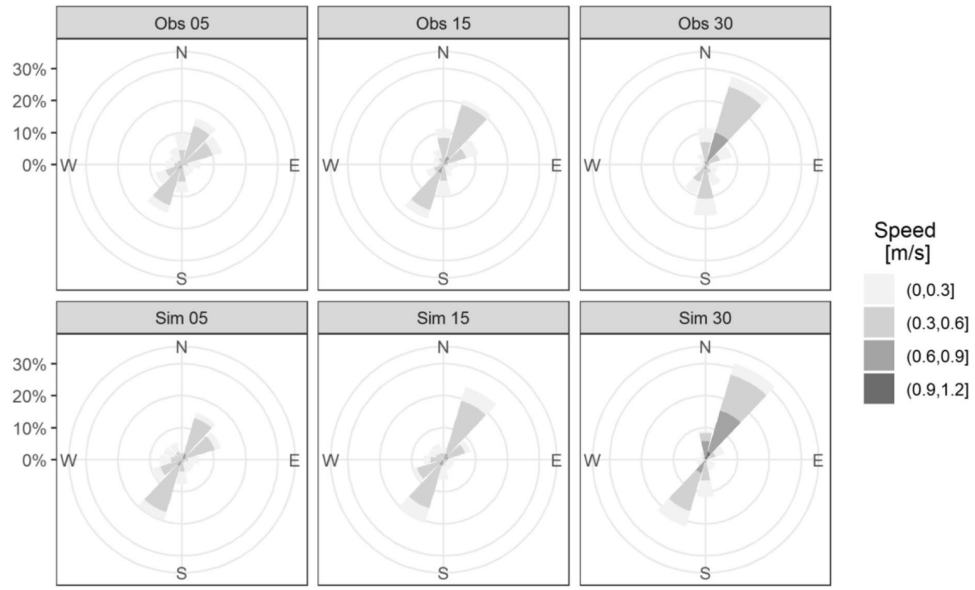

FIGURE 2 | Current directions and magnitudes from the observed **(top)** and simulated **(bottom)** total current at different depths (5, 15, and 30 m below surface).

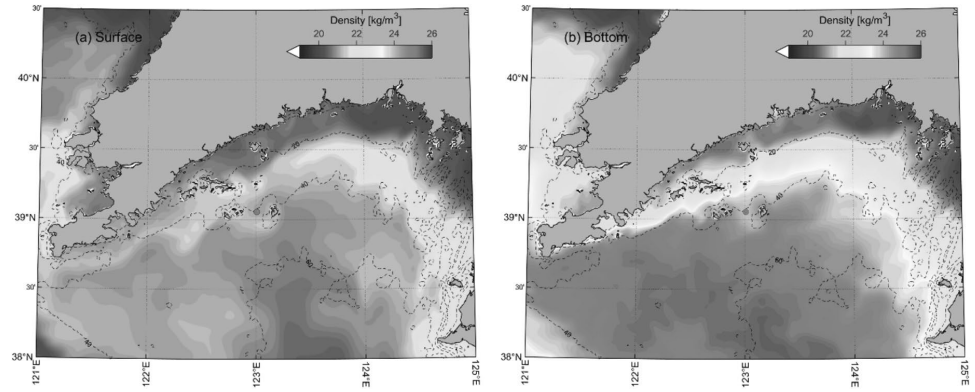

FIGURE 3 | (a) Surface and **(b)** bottom density (kg/m^3) computed from the numerical model results for July 2017. The dashed lines represent the isobath contours of 20, 40, and 60 m. The ADCP mooring site is shown with the red dot.

and ∼60 m, which overlap the location of the tidal mixing front (**Figure 3**). Areas of supercritical slopes will reflect the waves, while the waves can propagate in areas of sub-critical slopes depending on the local stratification. The rugged topography along the Korean coast has near critical or supercritical slope values, acting as an internal tide generator. Near the Changshan islands, there are also critical slopes that are eligible for emitting M_2 internal tides (**Figure 9B**). The depth-mean slope criticality from the model shows that favorable generation sites for M_2 internal tides are generally located between the depths of 40∼60 m (**Figure 9C**).

To visualize the internal tidal field, the vertical velocity fields computed from the difference between the baroclinic and barotropic M_2 model results are presented in **Figures 10A,B** with a 6-h time lag to represent the M_2 internal tide at 10 m depth. An opposite phase of the oscillation can be estimated

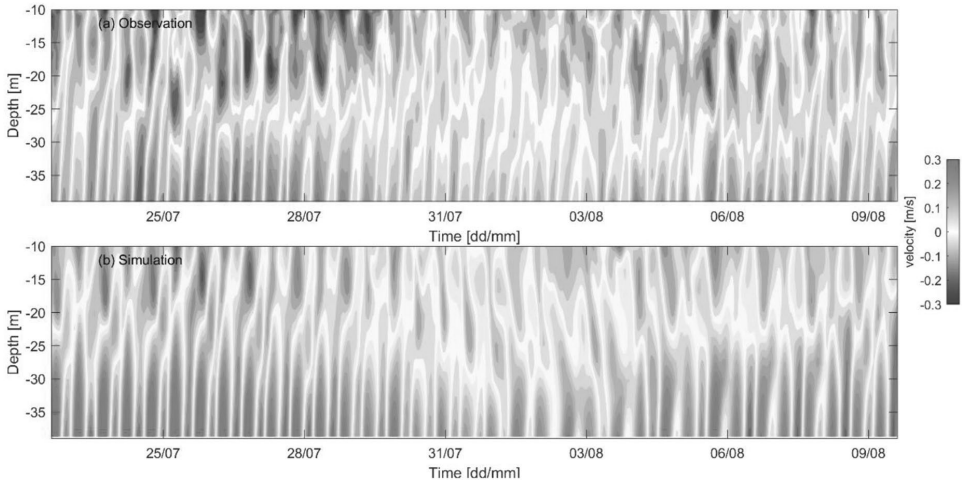

FIGURE 4 | The filtered baroclinic current component below 10 m depth for **(a)** observation and **(b)** simulation at the mooring site from July 23 to August 10, 2017. The component is computed along the major axis of the flow, which have the positive values at 30°toward north-east.

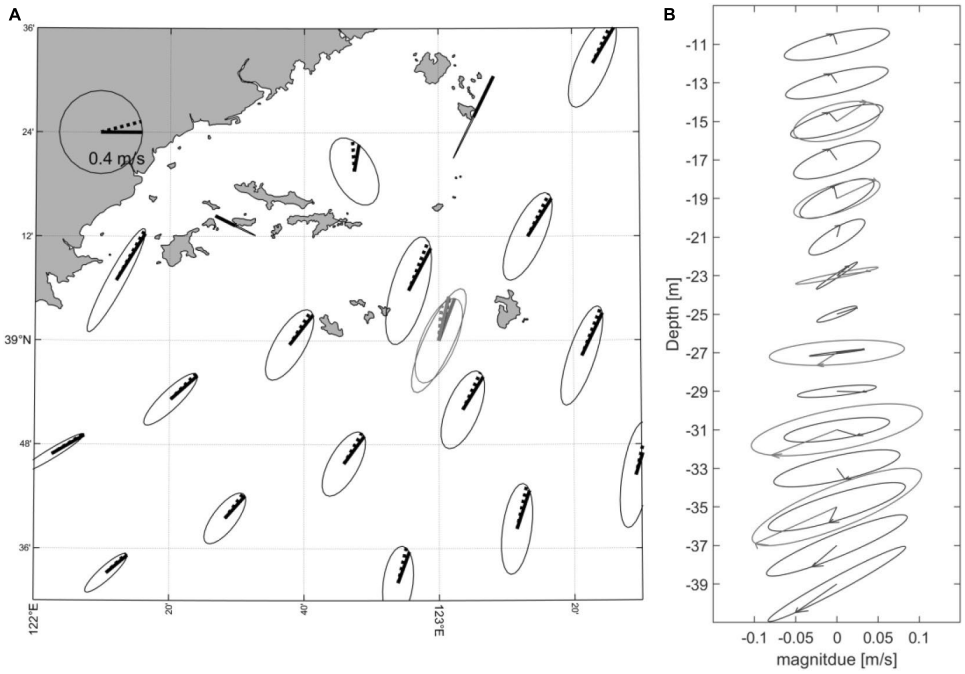

FIGURE 5 | (A) The barotropic M2 tidal ellipse derived from the model results (black), the ADCP observation (blue), and the simulation results at the mooring site (red) for 2017. **(B)** The vertical baroclinic M2 tidal ellipse derived from ADCP mooring results (blue) and the simulated ellipses (red) at given depths.

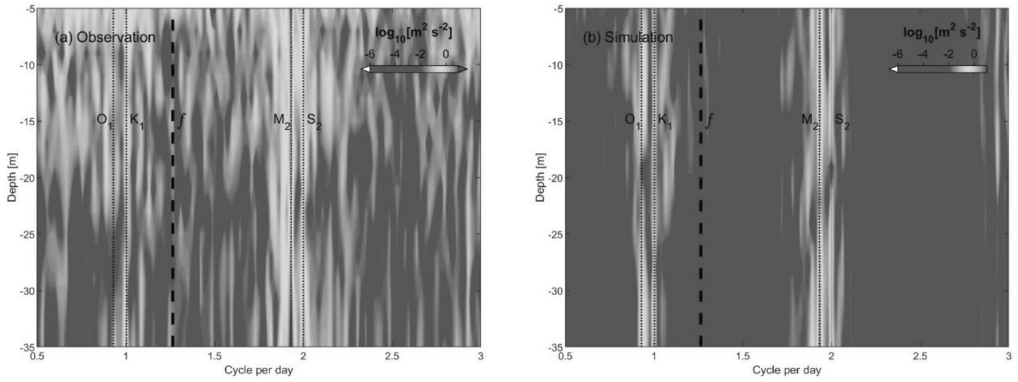

FIGURE 6 | Spectral analysis results of **(a)** observed and **(b)** simulated baroclinic current at the mooring site. The diurnal constituents K_1, O_1, and semi-diurnal constituents M_2, S_2 are represented with vertical dotted lines, and the inertial frequency (f) is represented with the thick dotted line.

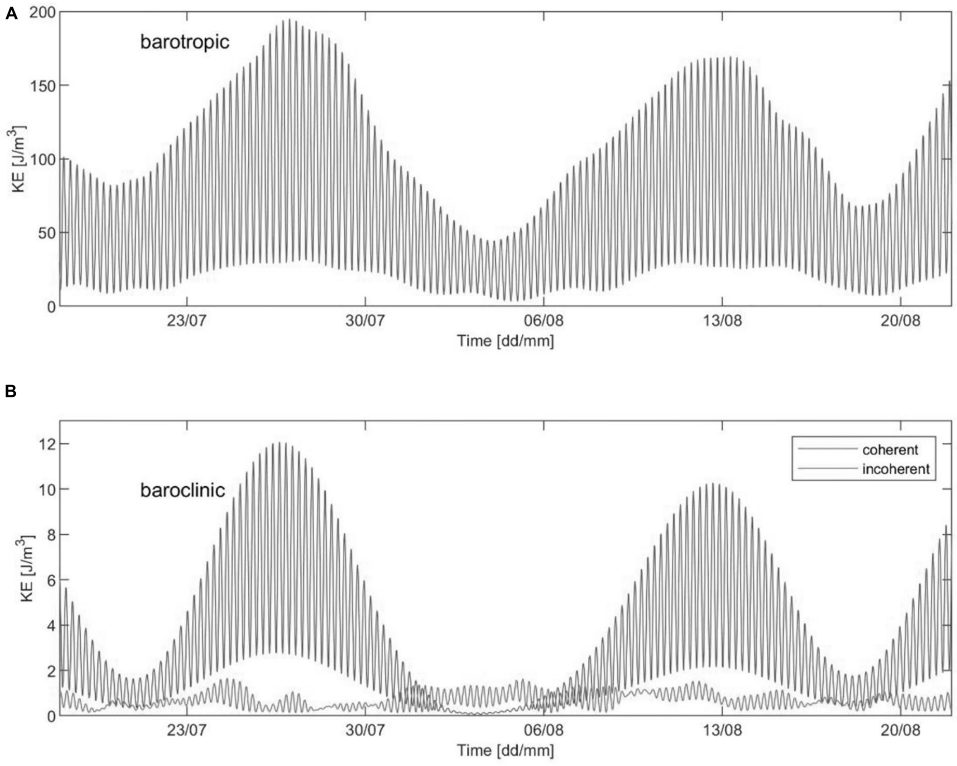

FIGURE 7 | Vertically averaged kinetic energy of the band-passed observed horizontal velocity. **(A)** The barotropic horizontal kinetic energy. **(B)** The coherent and incoherent baroclinic horizontal kinetic energy.

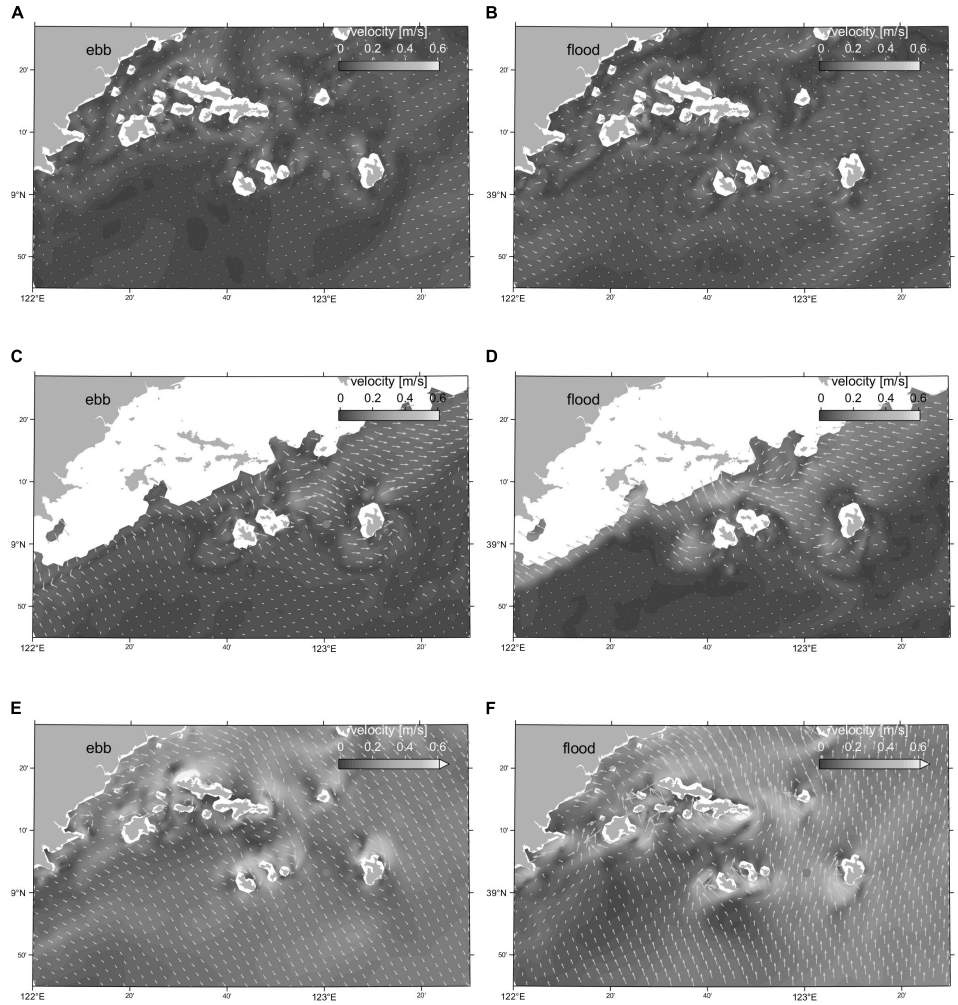

FIGURE 8 | Modeled M_2 baroclinic flow for horizontal current fields (m/s) 6-h apart (at ebb tide and flood tide) at different depths. **(A,B)** Baroclinic current at 15 m depth. **(C,D)** Baroclinic current at 30 m depth. **(E,F)** Barotropic flow. The baroclinic current component will add (or subtract) to the total current. The ADCP mooring location is marked as a red dot.

TABLE 2 | Statistics of current speed around the Changshan islands in **Figure 8**.

Layer	Moment	Maximum speed (m/s)	Mean speed (m/s)	Standard deviation (m/s)
15 m baroclinic current	High	0.42	0.05	0.03
	Low	0.31	0.06	0.03
30 m baroclinic current	High	0.24	0.06	0.03
	Low	0.34	0.07	0.06
Barotropic current	High	0.78	0.18	0.07
	Low	0.84	0.18	0.07

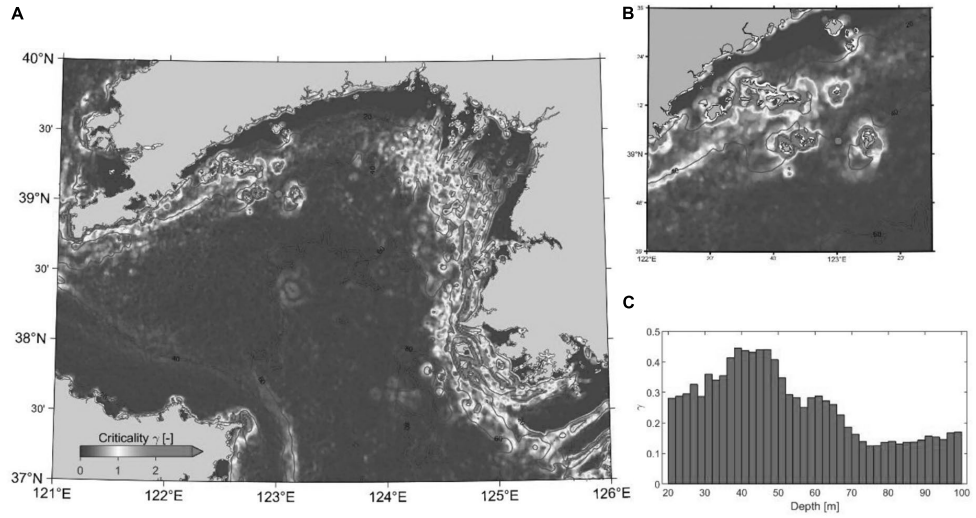

FIGURE 9 | (A) Criticality of the topography on the northern Yellow Sea shelf estimated from the mean simulated buoyancy frequency near the bottom between July 26 and August 10. Solid lines represent the isobath contours of 20, 40, 60, and 80 m. **(B)** Detailed view of slope criticality near the mooring ADCP (red dot). **(C)** The depth-mean topographic criticality calculated for the northern Yellow Sea.

from the striped patterns, which indicates propagation pathways. The internal tidal current is strong along the Korean coast with favorable generation conditions and abundant barotropic energy input (**Figure 10**). On the northern shelf near the Changshan islands, the internal tide propagates mainly along the tidal mixing front, passing the ADCP mooring. The horizontal wavelength and phase speed can also be estimated from the M_2 tidal period and the distance between each stripe, varying from 8.5 to 20 km and corresponding phase velocities between 0.19 and 0.45 m/s.

The depth-integrated energy conversion rate (C) from the barotropic tide (BT) to the baroclinic tide (BC) is shown in **Figure 11A**. A positive energy conversion is occurring along the Korean coast, with typical conversion rates greater than 0.01 W/m^2, making it a significant source for the M_2 internal tide in the northern Yellow Sea (**Figure 11A**). The positive conversion rate is much weaker (between 0.005 and 0.01 W/m^2) around the Changshan islands (**Figure 11B**), and with areas of negative conversion rates implying an energy transfer from BC to BT (<-0.01 W/m^2). The depth-binned accumulated conversion rate (**Figure 11C**) shows that the positive conversion mainly occurs below the depth of 35 m and with a maximum of around 50–60 m.

The time-averaged and depth-integrated baroclinic energy flux F_{bc} is presented for the M_2 baroclinic simulation in **Figure 12A**. The M_2 internal tides generally have a diverse propagation pattern in the northern Yellow Sea. The F_{bc} originated from the Korean coast is strong and generally directed westward between 38.5 and 39.5°N. The maximum flux is approximately 45 W/m. When approaching the northern shelf of the Yellow Sea and near the 50 m isobaths, the baroclinic energy propagates northward onshore with gradually reduced energy. A zoomed pattern of the F_{bc} around the Changshan islands is shown in **Figure 12B**, and the baroclinic energy flux is much weaker around the islands, with a maximum value of ∼10 W/m. In the nearshore areas, almost no baroclinic energy is propagating as the water is nearly homogeneous.

The time-averaged and depth-integrated coherent/incoherent baroclinic energy flux and the corresponding flux divergence derived from the M_2 baroclinic model results are presented for Changshan islands and the adjacent seas in **Figure 13**. The locations with high values of the coherent baroclinic energy flux and divergence (**Figure 13A**) coincide with the locations where the barotropic energy converts into baroclinic energy (**Figure 11**). Coherent baroclinic energy flux radiates away from the generation sites around the island. The M_2 internal tide mainly propagates westward, and the energy flux damps quickly after a few kilometers. The coherent M_2 baroclinic energy flux divergence is mostly negative around the Changshan islands, indicating a net loss of coherent energy within the domain. The incoherent baroclinic energy flux is almost an order of magnitude smaller than the coherent ones (**Figure 13B**), implying the internal tide generated at remote locations is weak in this region.

DISCUSSION

Model Performance

Numerical models are suitable to study and describe the dynamics of internal tide in various regions of the world (Kang and Fringer, 2012; Nash et al., 2012; Masunaga et al., 2017; Liu et al., 2019; Davis et al., 2020). As the

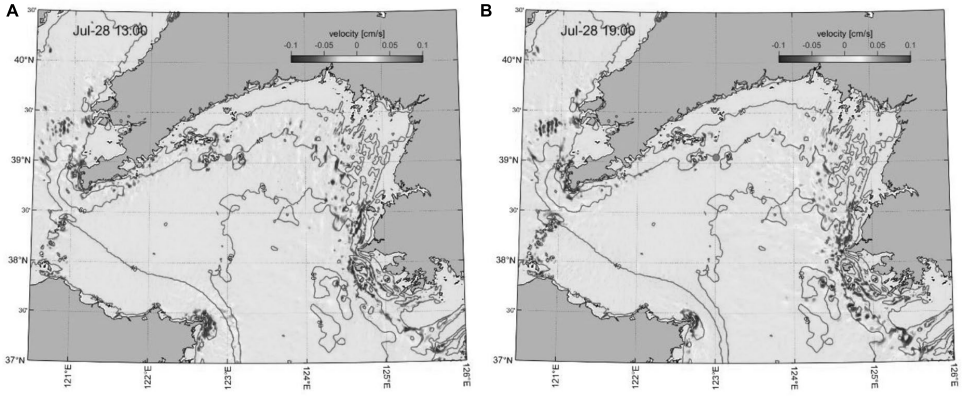

FIGURE 10 | Simulated vertical velocity difference (cm/s) at 10 m depth for **(A)** 13:00 July 28 and **(B)** 19:00 July 28, computed from baroclinic and barotropic simulations forced with the M_2 tidal component at the boundary. Solid lines represent the isobath contours of 20, 40, 60, and 80 m. The red dot represents the ADCP mooring location.

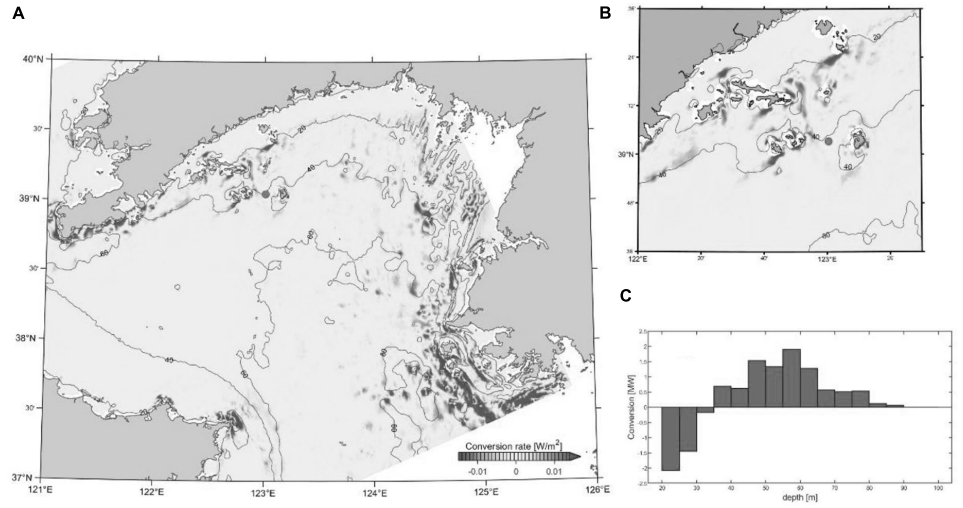

FIGURE 11 | (A) Depth integrated and period averaged barotropic to baroclinic energy conversion (W/m^2) in the northern Yellow Sea. Results were computed for the results from July 26 to August 10 in 2017. **(B)** The detailed conversion rate near the ADCP mooring site (red dot). **(C)** Mean conversion rate for binned depths within the domain in **(A)**. Solid lines represent the isobath contour of 20, 40, 60, and 80 m.

horizontal scale of the internal tide in the Yellow Sea is much larger than the regional depth, a hydrostatic model is sufficient to describe the features of the phenomena. The hydrodynamic model employed in this study has previously been applied to describe the hydrodynamics in the northern Yellow Sea by Lin et al. (2019) as well as in numerous applications worldwide[1]. The model results from the Yellow Sea were validated against current and water temperature observations and did reproduce the summertime total current field and thermohaline structure reasonably well (Lin et al., 2019).

In the present study, current observations from the summer of 2017 were compared to model results focusing on the baroclinic current features. The total horizontal current at different layers calculated by the current model agrees well with the observation results. The model results do reasonably

[1]www.myroms.org

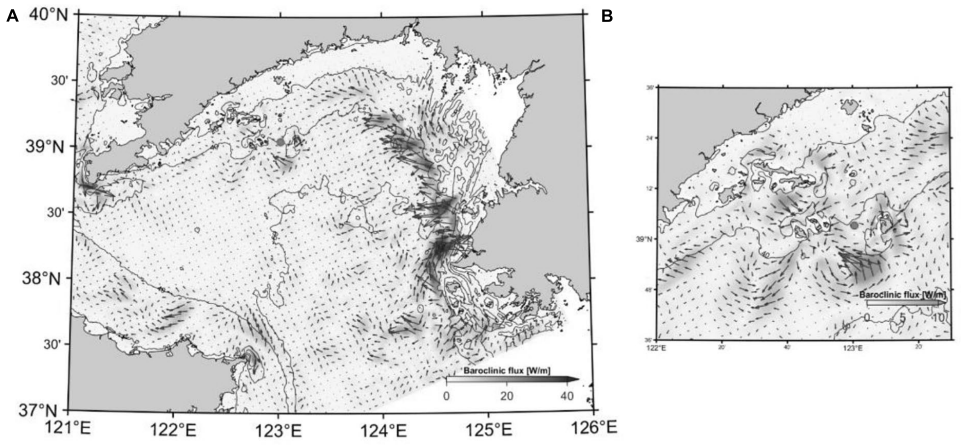

FIGURE 12 | (A) The depth-integrated baroclinic energy flux (W/m) for the M2 semi-diurnal internal tide in the northern Yellow Sea averaged from July 26 to August 10, 2017. **(B)** Detailed view of the baroclinic energy flux near Changshan islands, with the ADCP mooring location shown as the red dot.

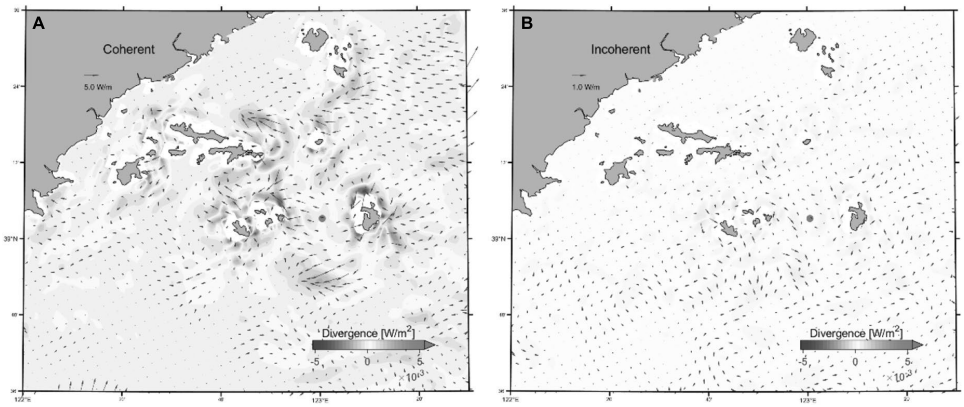

FIGURE 13 | (A) The coherent baroclinic energy flux ($\boldsymbol{F_{coh}}$, arrow W/m) and the flux divergence ($\nabla_H \cdot F_{coh}$, W/m^2) derived for 10 tidal cycles for the M_2 internal tide around the Changshan islands. **(B)** The incoherent baroclinic flux (F_{incoh}, arrow W/m) and flux divergence ($\nabla_H \cdot F_{incoh}$, W/m^2) for the same region. ADCP mooring location is represented as red dot.

reproduce the current magnitude and direction at all depths (the averaged RMS error is 0.12 m/s). The barotropic tide is dominant in this region, but the vertical current structure with a stronger flow speed toward the bottom is apparent in both the observation and simulation (**Figure 2**), demonstrating a robust baroclinic signal at the observation site. This baroclinic signal is a semi-diurnal mode-1 wave (**Figure 4**). With the barotropic component removed, the model results resemble a temporal-spatial baroclinic velocity pattern comparable to the observation. The barotropic and baroclinic tidal ellipses of the M_2 component also compare well between the observation and simulation results (**Figure 5**), indicating the dynamics of the internal tides are reproduced by the model. The spectral analysis results (**Figure 6**) illustrate that the M_2 internal tide is dominant in the entire water column but with a noisier pattern in the observations. The simulated baroclinic spectrum demonstrates a similar energy distribution concentrated around the diurnal and semi-diurnal frequencies. The discrepancy between the observation and simulation results is probably due to the inaccuracy in the background model stratification and smoothed bathymetry related to challenges in modeling turbulent mixing and potentially inaccurate depth data for this region. Also, the 1 km grid size will somewhat smooth the model results compared to the ADCP data.

Nevertheless, the comparison of the model results and observation shows that the hydrodynamic model is capable of reproducing the internal tides in the northern Yellow Sea.

Generation and Propagation of the Internal Tide in the Northern Yellow Sea

The focus of this study is to investigate the generation and propagation mechanism of the internal tides in the northern Yellow Sea. The current system in the Yellow Sea is dominated by the barotropic tides (Ichikawa and Beardsley, 2002; Xia et al., 2006; Hwang et al., 2014; Lin et al., 2019), with the main being the M_2 component for which the current amplitude is ∼0.5 m/s on the northern shelf (Lin et al., 2019). We concentrate on the M_2 internal tide since it is the dominating baroclinic component and can propagate with respect to the frequency restriction. Liu et al. (2019) have studied the seasonal and spatial distribution of the M_2 internal tides in the entire Yellow Sea and concluded with multiple sources and a complex interference internal tidal field in the summer. They focused on the southern Yellow Sea where the stratification is well established with the year-round buoyancy flux input from the Yangtze River estuary. In the northern Yellow Sea, the water depth is relatively shallow (<80 m), and the most intensive stratification is found at the seasonal thermocline above the YSBCW, where the buoyancy frequency can be around 2×10^{-3} s^{-1} (Lin et al., 2019), allowing the propagation of high-frequency internal waves. In the tidal mixing front along the shelf break, a typical depth-averaged buoyancy frequency is about 4.3×10^{-4} s^{-1}, satisfying the generation and propagation of the semi-diurnal internal tides with a frequency of about 2.2×10^{-5} s^{-1} (**Figure 9**). Hence, the M_2 internal tide in the northern Yellow Sea is mainly generated from the rugged topography within the tidal mixing front along the coast.

The various internal tidal wavelengths and the interference patterns computed from the M_2 internal tidal current field at 10 m depth (**Figure 10**) are consistent with previous studies (Liu et al., 2019). The relatively strong internal tidal signal appears to be within the tidal mixing front, coinciding with the generation pattern presented in **Figure 9**. A high BT-BC energy conversion (**Figure 11A**) occurs along the Korean coast where the tidal current is strong and supplies abundant kinetic energy (Lin et al., 2019). The negative conversion around this region may probably be caused by a remotely generated internal tide being superposed with locally generated ones, which does not refer to energy conversion from baroclinic tide to barotropic tide (Kang and Fringer, 2012; Masunaga et al., 2017). The detailed conversion pattern around the Changshan islands (**Figure 11B**) illustrates that the positive conversion here can be the source of the internal tidal signal captured at the current meter mooring location. The depth accumulated BT-BC conversion for the presented area (**Figure 11C**) implies that most internal tides inshore of 35 m isobath have been propagating from the deeper part, probably generated at the tidal mixing front nearby.

The depth-integrated and period-averaged baroclinic energy flux (**Figure 12A**) demonstrates a specific pattern of the internal tidal propagation for the simulation period. Because of the shallow bathymetry in the Yellow Sea (average depth of 44 m), the total baroclinic energy is non-comparable to that of the deep seas such as the South China Sea or Monterey Bay (Jan et al., 2008; Kang and Fringer, 2012). From the results of Liu et al. (2019), the most active region for baroclinic energy propagation is near the Yangtze River, with a typical energy flux of more than 100 W/m. In the northern Yellow Sea, baroclinic energy from the internal tide is mainly propagating westward from the Korean coast between the latitude of 38.5∼39.5°N. The maximum magnitude is around 45 W/m, and this is damped rapidly. The baroclinic energy flux is much weaker near the Changshan islands (**Figure 12B**), mainly due to less barotropic kinetic energy available. The relatively strong baroclinic energy flux in this region originates between the 40∼50 m isobaths near the islands, suggesting that the M_2 internal tidal signal captured by the ADCP is probably generated locally. This can also be confirmed from the spatial pattern of the coherent and incoherent baroclinic energy flux (**Figures 13A,B**). Coherent energy flux is dominant on the northern shelf, implying the baroclinic energy of the internal tide is mainly generated from local barotropic tides (**Figure 13A**). The coherent flux generally becomes stronger when propagating away from the islands and is damped toward the islands. The complicated and shallow topography around the Changshan islands makes the local generated internal tide a short-lived phenomenon limited to the neighboring area. The incoherent energy flux (**Figure 13B**) is about an order of magnitude smaller than the coherent energy flux, which is consistent with the results from the current observations from the ADCP (**Figure 7**).

From the perspective of the entire Yellow Sea, the internal tidal induced mixing only accounts for a small amount (∼0.8%) of the total tidal mixing. However, it can be important when discussing the enhanced turbulent mixing near the pycnoclines (Liu et al., 2019). When it comes to the northern shelf of the Yellow Sea where most regions either consist of homogeneous water or are located in the mixing front, the impact on currents is more prominent. The barotropic tide is most important for local water mass transportation (Lin et al., 2019), but in areas around the Changshan islands where locally generated internal tides are strong, the barotropic current will be modified by the internal tide. Typically, the internal tide will have a first mode or two-layer structure with the flow in the direction of the barotropic tide in the lower layer and the opposite direction in the upper layer (**Figure 8**). The interface of this two-layer structure is usually at a depth of approximately 25 m (**Figure 4**) and may vary with the background stratification caused by the barotropic advection and spring-neap tidal cycles. Generally, the internal tidal current is stronger at the bottom (**Figures 8C,D**) and at about 30% of the speed for the barotropic M_2 component. This superposed barotropic and baroclinic current may strengthen the bottom material transport within the northern shelf horizontally during each tidal oscillation. The vertical shear imposed by the internal tide may also enhance the turbulent mixing across the water

column in the tidal mixing front. Thus, promoting the material exchange in this aquaculture region on the northern shelf of the Yellow Sea.

CONCLUSION

The barotropic tide is important for the currents in the Yellow Sea and dominates the dynamics on the northern shelf. Our study using data from a current meter mooring and a regional current model, shows that also the semi-diurnal internal tide can be important in the northern Yellow Sea. The results indicate that:

- A mode-1, semi-diurnal internal tide is generated in the tidal mixing front of the northern shelf of the Yellow Sea.
- The current of the internal tide is in the same direction as the barotropic tide in the lower layer, adding to the total current toward the bottom.
- The internal tide is mainly generated locally and with a limited regional propagation.
- The shelf break areas toward the Korean coast are the most prominent locations for generation of the internal tide.

DATA AVAILABILITY STATEMENT

The raw data supporting the conclusions of this article will be made available by the authors, without undue reservation.

AUTHOR CONTRIBUTIONS

FL: manuscript writing and revision, model setup and run, data analysis, and data collection. LA: manuscript writing and revision and data analysis. HW: manuscript revision and data collection. All authors contributed to the article and approved the submitted version.

FUNDING

This research was jointly funded by the Sino-EU Cooperative Research on Ecosystem-based Spatial Planning for Aquaculture (2017YFE0112600) and the Central Public-interest Scientific Institution Basal Research Fund, CAFS (NO. 2020TD50). This research was also supported by the Research Council of Norway (249056/H30), and the Environment and Aquaculture Governance project (MFA, CHN 2152).

ACKNOWLEDGMENTS

We appreciate the support from Tianjin University and the Sea Ranching Research Center of Zoneco Co., Ltd., for their help in making observations. We also thank the European Center for Medium-Range Weather Forecasts for the atmospheric data, the international team of GEBCO for bathymetry data and NOPP for HYCOM data.

REFERENCES

Becker, J. J., Sandwell, D. T., Smith, W. H. F., Braud, J., Binder, B., Depner, J., et al. (2009). Global Bathymetry and Elevation Data at 30 Arc Seconds Resolution: SRTM30_PLUS. *Mar. Geod.* 32, 355–371. doi: 10.1080/01490410903297766

Cacchione, D. A., Pratson, L. F., and Ogston, A. S. (2002). The Shaping of Continental Slopes by Internal Tides. *Science* 296, 724–727. doi: 10.1126/science.1069803

Carter, G., Fringer, O., and Zaron, E. (2012). Regional Models of Internal Tides. *Oceanography* 25, 56–65. doi: 10.5670/oceanog.2012.42

Davis, K. A., Arthur, R. S., Reid, E. C., Rogers, J. S., Fringer, O. B., DeCarlo, T. M., et al. (2020). Fate of internal waves on a shallow shelf. *J. Geophys. Res. Oceans* 125. doi: 10.1029/2019jc015377

Dee, D. P., Uppala, S. M., Simmons, A. J., Berrisford, P., Poli, P., Kobayashi, S., et al. (2011). The ERA−Interim reanalysis: configuration and performance of the data assimilation system. *Q. J. Roy. Meteor. Soc.* 137, 553–597. doi: 10.1002/qj.828

Egbert, G. D., and Erofeeva, S. Y. (2002). Efficient Inverse Modeling of Barotropic Ocean Tides. *J. Atmos. Ocean Tech.* 19, 183–204. doi: 10.1175/1520-04262002019<0183:eimobo>2.0.co;2

Egbert, G. D., and Ray, R. D. (2001). Estimates of M2 tidal energy dissipation from TOPEX/Poseidon altimeter data. *J. Geophys. Res. Oceans* 106, 22475–22502. doi: 10.1029/2000jc000699

Fairall, C. W., Bradley, E. F., Rogers, D. P., Edson, J. B., and Young, G. S. (1996). Bulk parameterization of air−sea fluxes for Tropical Ocean−Global Atmosphere Coupled−Ocean Atmosphere Response Experiment. *J. Geophys. Res. Oceans* 101:3764. doi: 10.1029/95jc03205

Guo, S., and Hu, T. (2010). Simulating the effects of the internal tide in the Yellow Sea on acoustic propagation. *J. Harb. Eng. Univ.* 31, 967–974.

Haidvogel, D. B., Arango, H., Budgell, W. P., Cornuelle, B. D., Curchitser, E., Lorenzo, E. D., et al. (2008). Ocean forecasting in terrain-following coordinates: Formulation and skill assessment of the Regional Ocean Modeling System. *J. Comput. Phys.* 227:3624. doi: 10.1016/j.jcp.2007.06.016

Hwang, J. H., Van, S. P., Choi, B.-J., Chang, Y. S., and Kim, Y. H. (2014). The physical processes in the Yellow Sea. *Ocean Coast Manage* 102:457. doi: 10.1016/j.ocecoaman.2014.03.026

Ichikawa, H., and Beardsley, R. C. (2002). The Current System in the Yellow and East China Seas. *J. Oceanogr.* 58, 77–92.

Jan, S., Lien, R.-C., and Ting, C.-H. (2008). Numerical study of baroclinic tides in Luzon Strait. *J. Oceanogr.* 64, 789. doi: 10.1007/s10872-008-0066-5

Kang, D., and Fringer, O. (2012). Energetics of Barotropic and Baroclinic Tides in the Monterey Bay Area. *J. Phys. Oceanogr.* 42, 272–290. doi: 10.1175/jpo-d-11-039.1

Kumar, N., Suanda, S. H., Colosi, J. A., Haas, K., Lorenzo, E. D., Miller, A. J., et al. (2019). Coastal Semi-diurnal Internal Tidal Incoherence in the Santa Maria Basin, California: Observations and Model Simulations. *J. Geophys. Res. Oceans* 124, 5158–5179. doi: 10.1029/2018jc014891

Lee, J. H., Lozovatsky, I., Jang, S., Jang, C. J., Hong, C. S., and Fernando, H. J. S. (2006). Episodes of nonlinear internal waves in the northern East China Sea. *Geophys. Res. Lett.* 33:27136. doi: 10.1029/2006gl027136

Li, B., Wei, Z., Wang, X., Fu, Y., Fu, Q., Li, J., et al. (2020). Variability of coherent and incoherent features of internal tides in the north South China Sea. *Sci. Rep.* 10:12904. doi: 10.1038/s41598-020-68359-7

Lin, F., Asplin, L., Budgell, P., Wei, H., and Fang, J. (2019). Currents on the northern shelf of the Yellow Sea. *Regional. Stud. Mar. Sci.* 32:100821. doi: 10.1016/j.rsma.2019.100821

Liu, K., Sun, J., Guo, C., Yang, Y., Yu, W., and Wei, Z. (2019). Seasonal and Spatial Variations of the M2 Internal Tide in the Yellow Sea. *J. Geophys. Res.* 124, 1115–1138. doi: 10.1029/2018JC014819

Liu, Z., Wei, H., Lozovatsky, I. D., and Fernando, H. J. S. (2009). Late summer stratification, internal waves, and turbulence in the Yellow Sea. *J. Mar. Syst.* 77, 459–472. doi: 10.1016/j.jmarsys.2008.11.001

Masunaga, E., Fringer, O. B., Kitade, Y., Yamazaki, H., and Gallager, S. M. (2017). Dynamics and energetics of trapped diurnal internal Kelvin waves around a mid-latitude island. *J. Phys. Oceanogr.* 47, 2479–2498. doi: 10.1175/jpo-d-16-0167.1

Nash, J., Shroyer, E., Kelly, S., Inall, M., Duda, T., Levine, M., et al. (2012). Are Any Coastal Internal Tides Predictable?. *Oceanography* 25, 80–95. doi: 10.5670/oceanog.2012.44

Shang, X., Liu, Q., Xie, X., Chen, G., and Chen, R. (2015). Characteristics and seasonal variability of internal tides in the southern South China Sea. *Deep Sea Res. Part Oceanogr. Res. Pap.* 98, 43–52. doi: 10.1016/j.dsr.2014.12.005

Shchepetkin, A. F., and McWilliams, J. C. (2005). The regional oceanic modeling system (ROMS): a split-explicit, free-surface, topography-following-coordinate oceanic model. *Ocean Model* 9, 347–404. doi: 10.1016/j.ocemod.2004.08.002

Tana, Fang, Y., Liu, B., Sun, S., and Wang, H. (2017). Dramatic weakening of the ear-shaped thermal front in the Yellow Sea during 1950s–1990s. *Acta Oceanol. Sin.* 36, 51–56. doi: 10.1007/s13131-016-0885-y

Thorpe, S. A. (1998). Physical Processes in Lakes and Oceans. *Coast Estuar. Stud.* 1998, 441–460. doi: 10.1029/ce054p0441

Wang, Z., Li, Q., Wang, C., Qi, F., Duan, H., and Xu, J. (2020). Observations of internal tides off the coast of Shandong Peninsula. China. *Estuar. Coast Shelf Sci.* 245:106944. doi: 10.1016/j.ecss.2020.106944

Warner, J. C., Sherwood, C. R., Arango, H. G., and Signell, R. P. (2005). Performance of four turbulence closure models implemented using a generic length scale method. *Ocean Model* 8, 81–113. doi: 10.1016/j.ocemod.2003.12.003

Wei, H., Yuan, C., Lu, Y., Zhang, Z., and Luo, X. (2013). Forcing mechanisms of heat content variations in the Yellow Sea. *J. Geophys. Res. Oceans* 118, 4504–4513. doi: 10.1002/jgrc.20326

Xia, C., Qiao, F., Yang, Y., Ma, J., and Yuan, Y. (2006). Three−dimensional structure of the summertime circulation in the Yellow Sea from a wave−tide−circulation coupled model. *J. Geophys. Res. Oceans* 111:297.

Yan, T., Qi, Y., Jing, Z., and Cai, S. (2020). Seasonal and spatial features of barotropic and baroclinic tides in the northwestern South China Sea. *J. Geophys. Res.* 125:e2018JC014860. doi: 10.1029/2018JC014860

Zhu, J., Shi, J., Guo, X., Gao, H., and Yao, X. (2017). Air-sea heat flux control on the Yellow Sea Cold Water Mass intensity and implications for its prediction. *Cont. Shelf Res.* 152, 14–26. doi: 10.1016/j.csr.2017.10.006

Conflict of Interest: The authors declare that the research was conducted in the absence of any commercial or financial relationships that could be construed as a potential conflict of interest.

Publisher's Note: All claims expressed in this article are solely those of the authors and do not necessarily represent those of their affiliated organizations, or those of the publisher, the editors and the reviewers. Any product that may be evaluated in this article, or claim that may be made by its manufacturer, is not guaranteed or endorsed by the publisher.

Vol. 13: 111–119, 2021
https://doi.org/10.3354/aei00394

AQUACULTURE ENVIRONMENT INTERACTIONS
Aquacult Environ Interact

Published May 6

Rapid water temperature variations at the northern shelf of the Yellow Sea

Lars Asplin[1,*], Fan Lin[2,3,4], W. Paul Budgell[1], Øivind Strand[1]

[1]Institute of Marine Research, PB 1870 Nordnes, 5817 Bergen, Norway
[2]Yellow Sea Fisheries Research Institute, CAFS, 106 Nanjing Rd, 266000 Qingdao, PR China
[3]Laboratory for Marine Fisheries Science and Food Production Processes, Qingdao National Laboratory for Marine Science and Technology, 1 Wenhai Rd, Aoshanwei, 266237 Qingdao, PR China
[4]Geophysical Institute, University of Bergen, PB 7803, 5020 Bergen, Norway

ABSTRACT: During summer, there is great spatial variability in bottom water temperature on the northern shelf of the Yellow Sea. This variability is associated with a thermal front along the shelf. Oscillatory currents from semidiurnal and fortnightly period tides transport water masses laterally, resulting in oscillations of bottom water temperature at fixed positions, sometimes with large amplitudes. Temperature variations, as demonstrated in the present work, can cause damage to bottom-cultured scallops. In particular, in the scallop sea ranching area near Zhangzidao Island, such oscillations are evident in late summer. We constructed a spatial index of aggregated temperature variability from current model results identifying how temporal variability during the summer period varies in space. This information can be useful both in selecting favorable ranching areas and designing laboratory stress experiments on aquaculture candidate species.

KEY WORDS: Northern Yellow Sea shelf · Sea ranching · Current modelling · Yellow Sea Model · Tidal front

1. INTRODUCTION

The northern shelf of the Yellow Sea is a shallow shelf area extending approximately 200 km in the along-shore direction and 20–50 km in the cross-shore direction, with a mean depth of approximately 40 m. The currents are dominated by the tidal flow, with smaller contributions from wind-driven flow and a seasonal thermal jet (Lin et al. 2019). The water masses are seasonally heated and cooled, creating a large amplitude between the warmest water in summer and coldest in winter, with a typical range of bottom water temperature from <5 to >20°C. Due to mixing energy input from the tide combined with the shallow sloping bathymetry, a thermal front in the along-shore direction is established during the spring and summer (Simpson & Hunter 1974, Hill et al. 2008), and the water temperature difference across this front can be several degrees (Lin et al. 2019).

The northern shelf area is important for aquaculture, where sea ranching of the Japanese scallop *Patinopecten yessoensis* has been of particular economic importance (Zhou 2012). Ranching is carried out by releasing juveniles to bottom habitats, where the scallops usually reach market size after 3 yr. Mortalities of scallops in sea ranching within this region have been related to large bottom-water temperature variations in summer (Zhao et al. 2019). The water masses on the shelf oscillate back and forth over many km, mainly due to the various components of the tidal forcing (Lin et al. 2019). In areas with large horizontal bottom temperature gradients, e.g. in the region of the seasonal thermal front, periodically large variations of water temperature will occur and potentially expose individual scallops to water

*Corresponding author: lars.asplin@imr.no

Publisher: Inter-Research · www.int-res.com

temperature amplitudes of several degrees at tidal and longer frequencies (Lin et al. 2019). Previous records of massive mortality of cultured scallops have mostly been related to temperature extremes, reproduction processes, overcrowding and invaders or pathogens (Strand & Brynjeldsen 2003, Xiao et al. 2005, Shumway & Parsons 2016). Knowledge is lacking on how temperature variations at short temporal scales impact bivalves. However, recent experimental studies have shown that physiology, metabolism and immune functions in *P. yessoensis* are affected by acute temperature changes assumed to represent the temperature gradients on the northern shelf (Jiang et al. 2016, 2018a,b, Gao et al. 2017). Such temperature stress may act as a major factor in causing the observed mortality of scallops, but more information on spatial and temporal temperature variability is needed to understand its role in explaining the mortality.

The objective of our study was to demonstrate that high-resolution temporal and spatial bottom temperature variability based on numerical current model results for the Yellow Sea can be used to support risk assessment and sustainable management of scallop sea ranching on the northern shelf areas. The numerical model results we used have previously been validated for the northern shelf of the Yellow Sea and were found to be reasonably accurate (Lin et al. 2019). We identified the semidiurnal tidal current and a fortnightly oscillating current as being responsible for the variable bottom temperatures. From the time series of oscillating bottom temperatures, we created a spatially varying index representing the aggregated temporal temperature variation at the shelf area of relevance for scallop sea ranching. This index can be used to identify site and area suitability for sea ranching of scallops as well as help to explain differences in scallop mortality between years.

2. MATERIALS AND METHODS

2.1. The current model

We used the Regional Ocean Modeling System (ROMS) for our study (Shchepetkin & McWilliams 2005, Haidvogel et al. 2008). ROMS is solving the primitive hydrostatic equations including a free surface. The numerical grid has terrain following vertical coordinates and a rectangular Arakawa-C grid horizontally. Internationally, ROMS has been widely used in coastal studies, including along the Norwegian coast (Albretsen et al. 2012, Asplin et al. 2020). Our implementation of the ROMS for the Yellow Sea is a transfer of the model implementation along the Norwegian coast; it is named the Yellow Sea Model (YSM) and covers the Bohai Sea and the Yellow Sea. The horizontal grid size of the model is 1 km and there are 40 vertical terrain following layers. The resolution near the surface and the bottom is in dm and at the bottom is in m. The actual spacing is dependent on water depth. The model grid is rotated and has an open boundary towards the border between the Yellow Sea and the East China Sea. Bottom topography is interpolated from SRTM30-plus shuttle radar altimetry and the GEBCO 30′ database (Becker et al. 2009) (Fig. 1). Horizontally, the model uses a 3rd order upstream horizontal advection scheme for tracers and a 4th order centered advection scheme for momentum. Vertically, the model uses the Generic Length Scale k-kl vertical mixing scheme (Warner et al. 2005).

The atmospheric forcing component of the model is from the European Centre for Medium-Range Weather Forecast ERA-Interim Reanalysis data sets (Dee et al. 2011). The forcing contains wind velocity

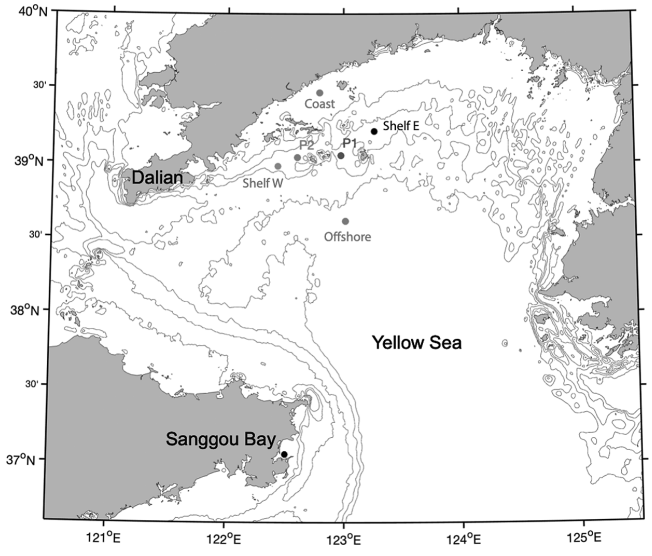

Fig. 1. The northern part of the Yellow Sea. Lines represent bathymetry every 10 m between 20 and 50 m depths. Colored dots: time series locations; P1: location of the current observations; P2: location of more detailed analysis of the bottom temperature variations. Zhangzidao Island is between P1 and P2

at 10 m height, surface-specific humidity derived from 2 m dew point temperature, surface air temperature at 2 m, downward longwave and shortwave radiation, precipitation and mean sea level pressure. Accumulated data such as radiation and precipitation are specified at 12 h intervals while the rest are at 6 h intervals. The atmospheric forcing was originally on a 3 km grid and is interpolated in the model grid. Net heat flux is computed from bulk formulae by Fairall et al. (1996).

At the open boundary, information of the tide, the daily mean sea surface elevation and daily values of currents, temperature and salinity in the vertical are specified. The values are taken from the HYCOM daily global ocean reanalysis (www.hycom.org). Eleven tidal components (M2, K2, S2, N2, K1, P1, O1, Q1, MN4, M4 and MS4 constituents) were taken from the Oregon State University global inverse tidal model TPXO7.2 (Egbert & Erofeeva 2002) and were specified at the open boundary. Open boundary data enter the domain using a radiative-nudging scheme. A quadratic bottom drag with a friction coefficient of 0.0025 is applied to the entire model domain.

The model results are based on a simulation with realistic forcing from August 2013 to December 2015. The initial conditions were interpolated from the HYCOM reanalysis. We store the model results as hourly and daily mean values. The model was also run for 2017 with only the tidal forcing activated, isolating this current component. The reason for selecting this period is an overlap with available current observations.

2.2. The observations

Current observation data are from moored acoustic Doppler current profilers (ADCPs) from 2 periods. From September to December 2015, current was measured by a Nortek ADCP 1 MHz Aquadopp Profiler (www.nortekgroup.com) with 1 m bin size and 20 bins, located near Zhangzidao Island at Site P1 (Fig. 1), measuring upwards. The accuracy of the instrument was 1% measured value ±0.5 cm s^{-1} for current profiling, ±0.1°C for the integrated temperature sensor and 0.5% of maximum range for the pressure sensor. In July and August 2017, an RDI ADCP 300 KHz profiler (http://www.teledynemarine.com/adcps/marine-measurements/) was moored at another location near Site P1. The accuracy of the current for the RDI instrument was 0.5% of the measured value ±0.5 mm s^{-1}. The ADCP measured the whole water column with a vertical bin resolution of 2 m.

3. RESULTS

The typical seasonal cycle of temperature for the water masses on the northern shelf of the Yellow Sea has a large amplitude, with maximum water temperature occurring in September and minimum in March. At Site P2 (Fig. 1), the time series of modelled surface and bottom temperature for 2014 and 2015 illustrate that the water masses are homogenized during late fall and winter and stratified during summer (Fig. 2). The depth at this location is 32 m. In areas on the shelf with depths shallower than 15–20 m, the water will be mostly homogeneous all year due to vertical mixing from the strong tide.

The spatial temperature difference is also high in late summer with a strong offshore gradient of the bottom temperature (Fig. 3). The temperature difference from the deeper outer part of the shelf to the shallower inner part is typically ~10°C in mid-September. The areas along the thermal front will be vulnerable to temperature variations if the water masses oscillate in the cross-front direction.

To illustrate the temporal variability at various locations at the shelf, we extracted time series of bottom water temperatures from 4 locations in the region of the thermal front (Shelf W, P1, P2 and Shelf E; Fig. 1), one from a location near the coast, one in

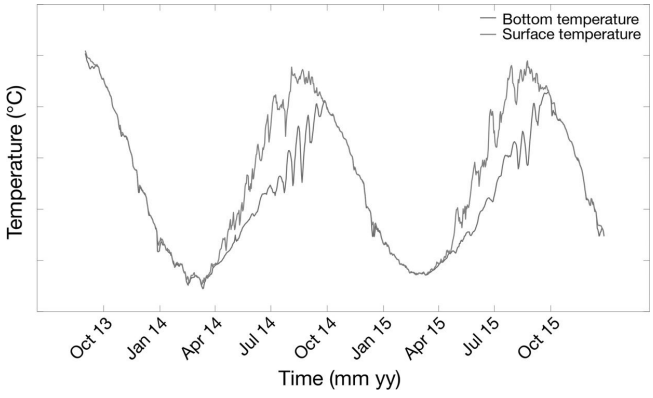

Fig. 2. Time series of water temperature at the surface (red line) and the bottom (blue line) from Site P2, west of Zhangzidao Island

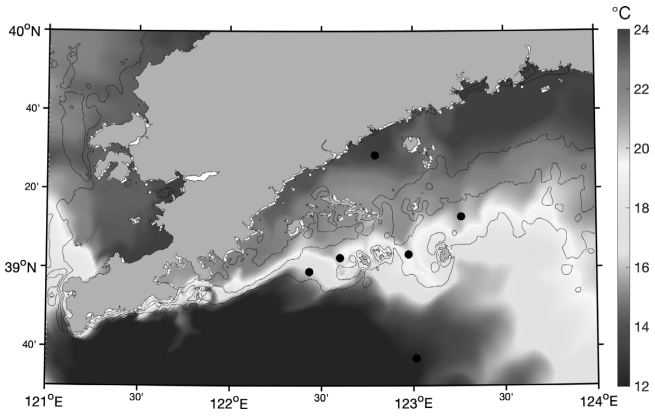

Fig. 3. Bottom water temperature on 15 September 2014, from the numerical current model results. Black lines: isobaths for 20, 30 and 40 m depths; black dots: locations where time series were extracted (see Fig. 1)

the open sea and one across the sea in the Sanggou Bay, which is another intensive aquaculture area. After reducing the diurnal and semidiurnal tidal signals with a 48 h, 4th order Butterworth filter, we see the strong seasonal signal with bottom water temperatures higher than 20°C in late summer and lower than 5°C in the winter (Fig. 4). The 4 locations on the northern shelf vary similarly throughout the season, but the 2 westernmost locations (P2 and Shelf W; red and green colored lines in Fig. 4) experience some large oscillations in August and September before the water temperature reaches its maximum value. The amplitude of these oscillations is several degrees Celsius and a period of approximately 2 wk is apparent. At the 2 easternmost locations (Shelf E and P1; black and blue lines in Fig. 4) such oscillations are less pronounced. The strongest seasonal signal occurs at the location close to the coast (red dotted line in Fig. 4), whereas the seasonal signal is much reduced offshore (blue dotted line in Fig. 4). On the other side of the sea in the other large aquaculture area at Sanggou Bay, the temperature variation is also relatively strong (black dotted line in Fig. 4).

A closer view of the bottom temperature at Site P2 (Fig. 1) illustrates the oscillations with temperature amplitudes of several degrees (Fig. 5). Both the full temporal resolution with hourly values from the numerical model results and the 48 h low-pass filtered values are presented. The difference between these 2 time series is shown as a black line in Fig. 5, illustrating the variability due to the strong high frequency tidal flow only. Superposed on the high frequency oscillations of the semidiurnal tide (M_2, ~12.4 h) we have 4–5 low-frequency oscillations of ~2 wk period and amplitudes up to more than 2°C in the late summer in both 2014 and 2015.

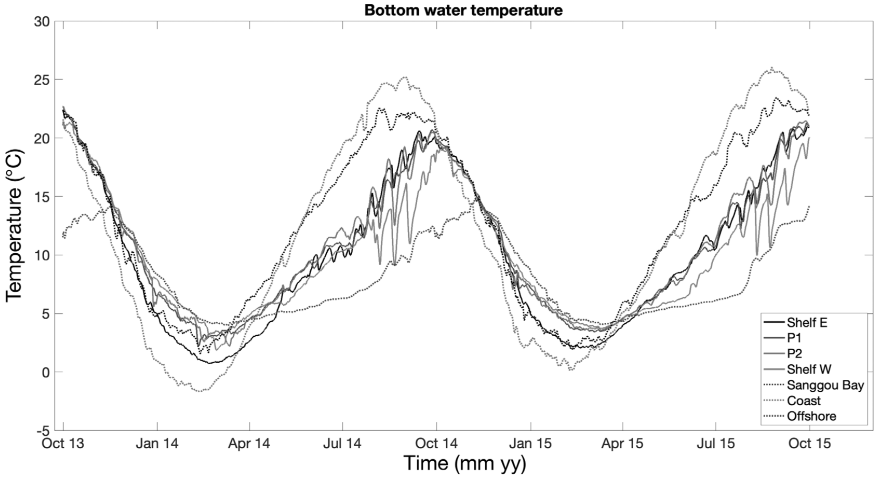

Fig. 4. Time series of bottom water temperature from locations at the northern shelf of the Yellow Sea and at Sanggou Bay. The positions are marked on the map in Fig. 1, and the line colors are similar to the colors of the dots. Black dotted line: Sanggou Bay location; red dotted line: location near the coast; blue dotted line: location offshore in the ocean

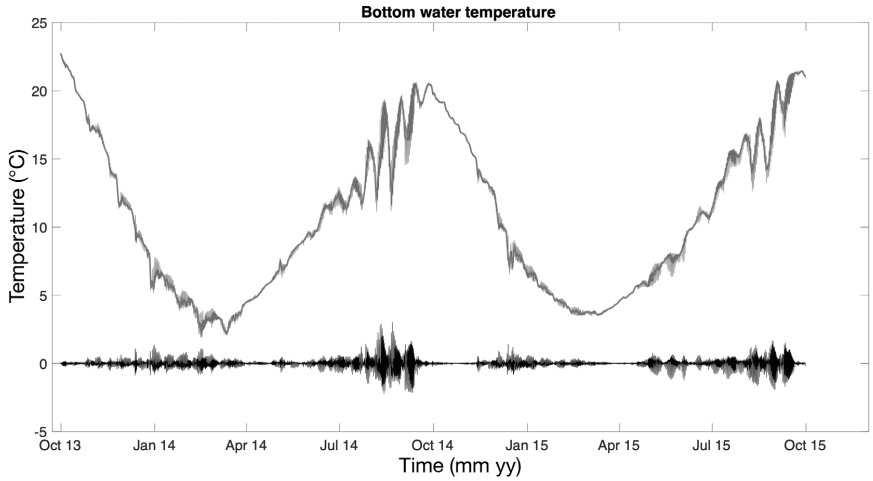

Fig. 5. Time series of bottom temperature (blue line), the low-passed values (red line) and the difference between the 2 (black line) at Site P2, west of Zhangzidao Island

The temperature oscillations with the longer period must be due to a slowly oscillating current component superposed on the higher frequency tidal flow. From a 7 d low-pass filtered time series of the bottom current component along the North–South direction, we indeed find small amplitude oscillations (1–2 cm s^{-1}) with a typical period of ~2 wk (Fig. 6). The time series are from the 2 locations on the shelf (Sites P1 and P2 in Fig. 1) as well as the observed bottom current near Site P1. The currents are from a depth above the frictional bottom layer. The time period covers 2014 and 2015 for the model results and late fall 2015 for the observations. The modelled current has a net southerly component and there is a seasonal signal with a stronger southerly flow during summer.

In order to further investigate the nature of these long period current oscillations, the YSM was run for 2017 with only tides as forcing, i.e. other forcing mechanisms such as wind, radiation, runoff and a daily open boundary forcing were omitted. The current components along the *x*- and *y*-directions of the model grid after 7 d low-pass filtering reveal current oscillations with a near 14 d period and a magnitude

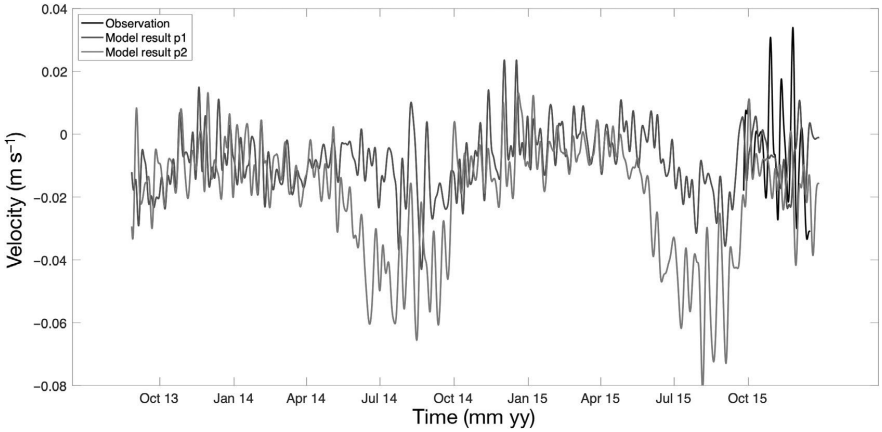

Fig. 6. Time series from the model results of 7 d low-passed north–south current component close to the bottom at Sites P1 and P2. The black line is a similar current component from the observations near P1

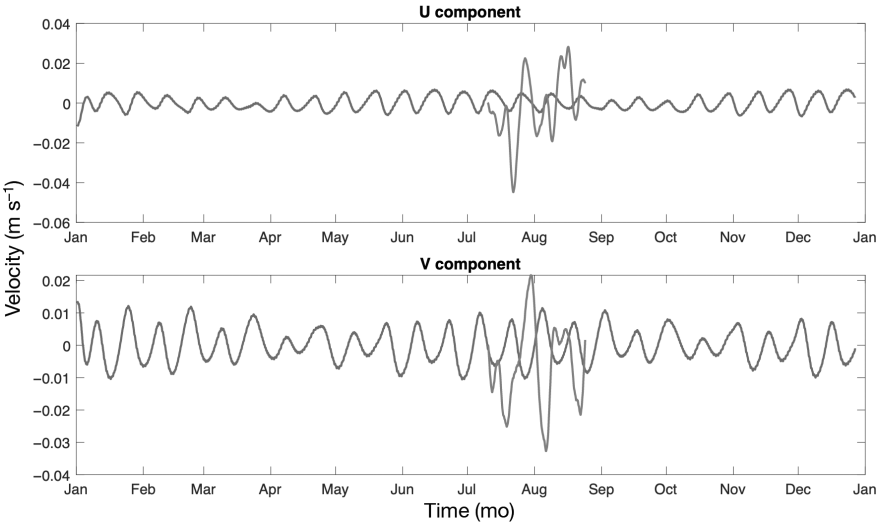

Fig. 7. Time series of 7 d low-passed current component close to the bottom at Site P1 from the model results of the tides only simulation of 2017. Red line: similar current component from observations, including additional forcing compared to the model results

around 1–2 cm s^{-1} (Fig. 7). Observations from this location (red line) also reveal similar oscillations and amplitude, although they are not directly comparable since the numerical model results lack all the available forcing.

Based on the numerical model results, we can spatially quantify the influence of both the low-frequency bottom temperature oscillations and the (mostly) semidiurnal tidal oscillations in late summer. From individual oscillations, we multiply the temperature difference between the maximum and minimum temperatures in the first half of the wavelength with the time between the 2 in days and sum these values at each grid square in the numerical model domain. We call this index 'dt*days' (with units [°C day]), and it will represent an aggregated value of the temperature oscillation effect at that location. Hence, this can be viewed as a measure of an environmental stress on the organisms. The period 1 July to 30 September is when the thermal front along the shelf is well established. The geographical distribution of the 'dt*days' index shows that the highest values mainly appear at locations with bathymetry between 20 and 40 m, where the thermal front is located (Fig. 8a–d). We split the index values between those generated by oscillations from the semidiurnal tide (Fig. 8c,d) and those generated by longer period oscillations (Fig. 8a,b). Obviously, the semidiurnal tides generate higher values of the index compared to those of the longer period oscillations. We also find differences between years in the 'dt*days' index, mostly attributable to the influence of the long-period oscillations.

Spatially aggregated values of the 'dt*days' index as an average for the 2 summer periods for the whole domain shown in Fig. 8 reveal relatively similar values (Table 1). The index is nearly twice as high from the semidiurnal oscillations compared to the longer period oscillations. The mean values for the whole shelf area do not differ appreciably between the summers of 2014 and 2015. This is not the case, however, if we perform this calculation only for the scallop ranching area marked by the black rectangle in Fig. 8a. For this area, which is located close to the thermal front, we find larger variability between years and especially in the values from the long-period oscillations.

4. DISCUSSION

We have shown that the bottom water temperature can oscillate by several degrees in amplitude and last many weeks in areas along the northern shelf of the Yellow Sea. This occurs mostly in late summer when the thermal front is established. The period of oscillations is either semidiurnal or approximately 14 d. The reason for these temperature fluctuations at specific

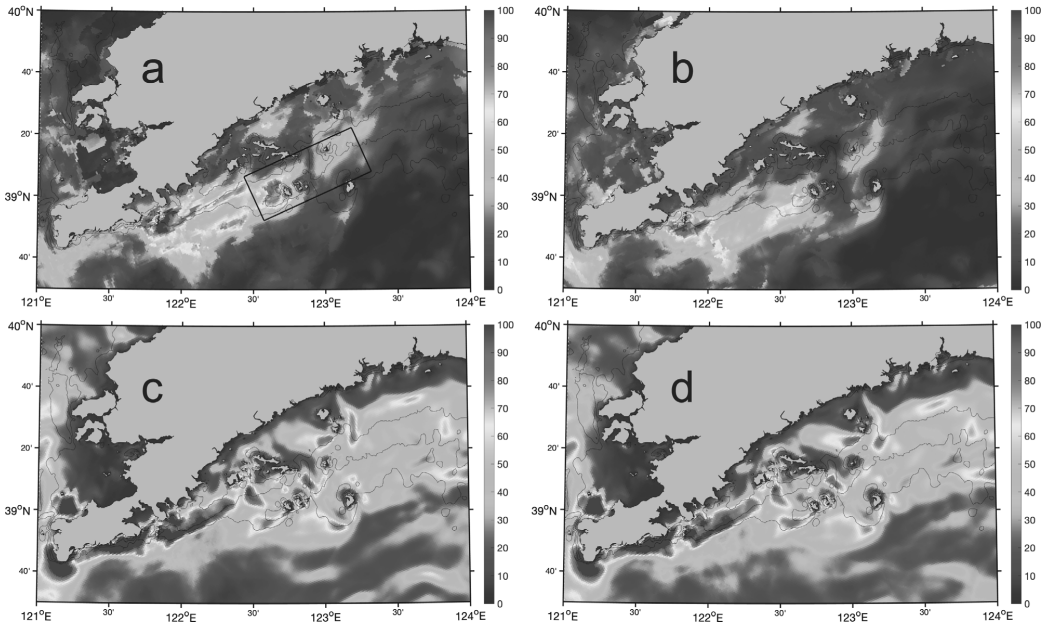

Fig. 8. Geographical distribution of the 'dt•days' index for the period 1 July to 30 September in (a,c) 2014 or (b,d) 2015, based on (a,b) low-passed bottom temperature time series or (c,d) original bottom temperature time series. Lines: isobaths for 20, 30 and 40 m depth; black rectangle: production area for Japanese scallops

Table 1. Spatial mean values of the 'dt•days' index for the whole northern shelf area and scallop ranching area (in parenthesis) based on the bottom temperature low-passed time series (long period) and the pure tidal component (semidiurnal)

Time	De-tided (°C day)	Hourly tidal (°C day)	Sum (°C day)
Summer 2014	14 (35)	24 (49)	38 (84)
Summer 2015	15 (24)	25 (45)	40 (69)

locations is the combination of an oscillatory current and a spatial temperature gradient. Thus, both the semidiurnal tidal flow (i.e. the M_2 component) and the low frequency and much weaker fortnightly oscillating flow will move water of different temperature back and forth.

It is well known that on shallow shelves with a strong tidal flow, a thermal front can be established with vertical homogeneous water in the onshore direction or towards shallower depths and a thermal stratification offshore or towards deeper water (Simpson & Hunter 1974, Hill et al. 2008). This is also the case on the northern shelf during the summer with an along-shore thermal front mainly following the 20–30 m isobaths (Lin et al. 2019). The sea ranching areas near Zhangzidao Island were situated in the middle of the frontal zone in September 2014.

The movement of the water from the semidiurnal tide will typically be 5–10 km back and forth (Lin et al. 2019). Longer oscillations will move the water back and forth 5–10 km given that the water speed is 0.01–0.02 m s^{-1} and the period of the oscillation is around 14 d. Thus, the total area affected can have a radius of 10–20 km depending upon the phases of the 2 oscillations.

The low frequency oscillation appears in both the numerical model results and the observations. Even though the current speed is low, its duration of flow in the same direction makes it important. After running the numerical model forced by tides only, the oscillations appear year-round and are a permanent phenomenon (Fig. 7). In the results of the simulation including all forcing mechanisms, we find an even longer seasonal signal (Fig. 6). This might be of importance. The origin could be variations in stratification or the seasonality of the winds; however, this is beyond the scope of the present investigation.

The 14 d signal in the current field could be produced by nonlinear advection processes that generate compound shallow water tidal constituents at the sum (quarter-diurnal MS4) and difference (fortnightly MSF) of the lunar M2 and S2 tidal frequencies (Godin 1972). The spring–neap modulation of the semi-diurnal tide can produce fortnightly variations in the strength of vertical mixing (Haas 1977, Budgell 1982) which can lead to fortnightly variations in bottom temperature. The circulation is also affected in an indirect manner on a 14 d time scale by spring–neap variations in frontal structure caused by changes in vertical mixing (Li & Zhong 2009).

We found differences between the summers of 2014 and 2015 in the 'dt*days' index, but mostly these appear in space. When considering the whole northern shelf, the difference between 2014 and 2015 is small (Table 1). However, inside the scallop production area (Fig. 8a) the index is more than 20% higher in 2014 compared to 2015. This difference is mostly due to the contribution from the long period oscillations. This can be interpreted as the location of the seasonal thermal front varying between years. The mechanisms behind the front are the tidal current, bottom topography, atmospheric radiation (heat exchange) and other mixing agents like wind. Only the last 2 will change between years; thus, the atmospheric conditions will probably cause the interannual differences of the thermal front strength and location. The difference of the 'dt*days' index between 2014 and 2015 illustrates that there can be a temporal–spatial shift in the bottom temperature patterns and magnitude. Experimental studies by Jiang et al. (2016, 2018a,b) indicate that acute temperature variations are more critical to the scallops than variations at longer periods. This factor will be affected by such temporal–spatial shifts and influences how the risk of scallop mortality should be assessed.

The spatial–temporal variability of the temperature gradients shown in our study is crucial information for designing experiments to better understand stress responses of *Patinopecten yessoensis* and ultimately the role of the temperature environment in explaining their growth and mortality in sea ranching (Zhao et al. 2019). In previous studies, indices typically representing the temperature environment integrated over time (e.g. growing degree days) have been used in assessing temperature-dependent growth and development in several molluscan species (Broell et al. 2017, Steeves et al. 2018). To our knowledge, none of the previous studies used indices involving representation of the degree of temperature oscillations. The variability in the 'dt*days' index is an approach normalizing the temperature environment assumed to detrimentally affect the scallops over the spatial domain in the sea ranching area. However, better understanding of physiological and immunological factors affecting the mortality of the scallops is needed to access thresholds for mortality in sea ranching conditions (Jiang et al. 2018a,b). Therefore, more research needs to be completed before higher accuracy can be provided in developing temperature indices for risk assessment and site or area selection for the scallop releases. Such indices would clearly contribute to the development of sustainable sea ranching and would likely provide direct economic benefit to the aquaculture industries in the area.

The results from the YSM reproduced the ambient environment reasonably well. These results will be available for further investigations. We believe that this information, in combination with specifications of the relationship between physical stress on the cultured scallops and the effects on scallop growth and survival, can be used to identify favorable sea ranching conditions. Temperature variations extracted from model results can provide crucial information for further physiological study of high frequency stress.

Acknowledgements. The authors sincerely appreciate the support from Sea Ranching Research Center of Zoneco, for their help in making observations. The authors also thank the European Center for Medium-Range Weather Forecasts for the atmospheric data, the international team of GEBCO for bathymetry data and NOPP for HYCOM data. This research was supported by the Research Council of Norway (249056/H30), Environment and Aquaculture Governance (MFA, CHN 17/0033) and Horizon 2020 IMPAQT project (774109). This research was also supported by the Key Programme for International Cooperation on Scientific and Technological Innovation, Ministry of Science and Technology (2017YFE0118300).

LITERATURE CITED

Albretsen J, Aure J, Sætre R, Danielssen DS (2012) Climatic variability in the Skagerrak and coastal waters of Norway. ICES J Mar Sci 69:758–763

Asplin L, Albretsen J, Johnsen IA, Sandvik AD (2020) The hydrodynamic foundation for salmon lice dispersion along the Norwegian coast. Ocean Dyn 70:1151–1167

Becker JJ, Sandwell DT, Smith WHF, Braud J and others (2009) Global bathymetry and elevation data at 30 arc seconds resolution: SRTM30_PLUS. Mar Geod 32: 355–371

Broell F, McCain JSP, Taggart CT (2017) Thermal time explains size-at-age variation in molluscs. Mar Ecol Prog Ser 573:157–165

Budgell WP (1982) The influence of the spring–neap tidal cycle upon vertical stratification in Chesterfield Inlet, Hudson Bay. Nat Can 109:709–718

Dee DP, Uppala SM, Simmons AJ, Berrisford P and others (2011) The ERA-Interim Reanalysis: configuration and performance of the data assimilation system. Q J R Meteorol Soc 137:553–597

Egbert GD, Erofeeva SY (2002) Efficient inverse modeling of barotropic ocean tides. J Atmos Ocean Technol 19:183–204

Fairall CW, Bradley EF, Rogers DP, Edson JB, Young GS (1996) Bulk parameterization of air–sea fluxes for tropical ocean–global atmosphere coupled–ocean atmosphere response experiment. J Geophys Res Oceans 101:3747–3764

Gao G, Zhang J, Li M, Ma S, Guo X, Jiang W, Lv X (2017) Effects of temperature fluctuation on physiological and immune parameters of scallop (*Patinopecten yessoensis*). Yuye Kexue Jinzhan 38:148–154 (In Chinese)

Godin G (1972) The analysis of tides. University of Toronto Press, Toronto

Haas LW (1977) The effect of the spring–neap tidal cycle on the vertical salinity structure of the James, York and Rappahannock Rivers, Virginia, USA Estuar Coast Mar Sci 5:485–496

Haidvogel DB, Arango H, Budgell WP, Cornuelle BD and others (2008) Ocean forecasting in terrain-following coordinates: formulation and skill assessment of the Regional Ocean Modeling System. J Comput Phys 227:3595–3624

Hill AE, Brown J, Fernand L, Holt J and others (2008) Thermohaline circulation of shallow tidal seas. Geophys Res Lett 35:L11605

Jiang W, Li JQ, Gao YP, Mao YZ and others (2016) Effects of temperature change on physiological and biochemical responses of Yesso scallop, *Patinopecten yessoensis*. Aquaculture 451:463–472

Jiang W, Lin F, Fang J, Gao Y and others (2018a) Transcriptome analysis of the Yesso scallop, *Patinopecten yessoensis* gills in response to water temperature fluctuations. Fish Shellfish Immunol 80:133–140

Jiang W, Du M, Fang J, Gao Y and others (2018b) Response of Yesso scallop *Patinopecten yessoensis* to acute temperature challenge: physiological and biochemical parameters. J Oceanol Limnol 37:321–329

Li M, Zhong L (2009) Flood–ebb and spring–neap variations of mixing, stratification and circulation in Chesapeake Bay. Cont Shelf Res 29:4–14

Lin F, Asplin L, Budgell WP, Wei H, Fang J (2019) Currents on the northern shelf of the Yellow Sea. Reg Stud Mar Sci 32:100821

Shchepetkin AF, McWilliams JC (2005) The regional oceanic modeling system (ROMS): a split-explicit, free-surface, topography-following-coordinate oceanic model. Ocean Model 9:347–404

Shumway SE, Parsons GJ (eds) (2016) Scallops: biology, ecology, aquaculture and fisheries, 3rd edn. Elsevier Science, Oxford

Simpson JH, Hunter JR (1974) Fronts in the Irish Sea. Nature 250:404–406

Steeves LE, Filgueira R, Guyondet T, Chassé J, Comeau L (2018) Past, present, and future: performance of two bivalve species under changing environmental conditions. Front Mar Sci 5:184

Strand Ø, Brynjeldsen E (2003) On the relationship between low winter temperatures and mortality of juvenile scallops, *Pecten maximus* L., cultured in western Norway. Aquacult Res 34:1417–1422

Warner JC, Sherwood CR, Arango HG, Signell RP (2005) Performance of four turbulence closure models implemented using a generic length scale method. Ocean Model 8:81–113

Xiao J, Ford S, Yang H, Zhang G, Zhang F, Guo X (2005) Studies on mass summer mortality of cultured zhikong scallops (*Chlamys farreri* Jones et Preston) in China. Aquaculture 250:602–615

Zhao Y, Zhang J, Lin F, Ren JS and others (2019) An ecosystem model for estimating shellfish production carrying capacity in bottom culture systems. Ecol Modell 393:1–11

Zhou JH (2012) Preliminary study on structure and characteristic of Yesso scallop industry in LiaoNing. MSc dissertation, The Ocean University of China, Qingdao (in Chinese)

Editorial responsibility: Jonathan Grant, Halifax, Nova Scotia, Canada
Reviewed by: 3 anonymous referees

Submitted: June 12, 2020
Accepted: January 18, 2021
Proofs received from author(s): April 22, 2021

Ecological Modelling 431 (2020) 109181

Contents lists available at ScienceDirect

Ecological Modelling

journal homepage: www.elsevier.com/locate/ecolmodel

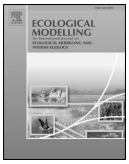

A physical-biological coupled ecosystem model for integrated aquaculture of bivalve and seaweed in sanggou bay

L.I.N. Fan[a,b,c], D.U. Meirong[a,b], L.I.U. Hui[a,b], F.A.N.G. Jianguang[a,b], ASPLIN Lars[d], J.I.A.N.G. Zengjie[a,b,*]

[a] Yellow Sea Fisheries Research Institute, Chinese Academy of Fishery Science, Qingdao, China
[b] Laboratory for Marine Fisheries Science and Food Production Processes, Qingdao National Laboratory for Marine Science and Technology, China
[c] Geophysical Institute, University of Bergen, Norway
[d] Institute of Marine Research, Bergen, Norway

ARTICLE INFO

Keywords:
Sanggou bay
Bivalve-seaweed integrated aquaculture
Ecosystem model
Individual growth model
Carrying capacity estimation

ABSTRACT

To understand the biological process in an aquaculture dominant coastal system and to provide a tool for further aquaculture management, an ecosystem model has been implemented to study the aquaculture-environmental interaction and the carrying capacity for Sanggou Bay. The model coupled the pelagic system, kelp growth dynamics, oyster energetics, and population dynamics with hourly hydrodynamic and water quality data. The study area was divided into four boxes according to similarities in the hydrological environment and aquaculture layout. Scenario simulations were conducted with different combinations of oyster and kelp seeding densities to examine the environmental impacts and production under different aquaculture layouts. Results showed that the model could capture the main characteristics of observed environmental variables and culture organism growth. Increased seeding density of both oysters and kelp generally leads to increased production with diminished individual growth. Kelp aquaculture plays a leading role in the nutrient cycle in the bay, acting as a large reception tank during the rapid growth period. The model results indicate that there is still potential to increase production for both oyster and kelp in Sanggou bay. The current aquaculture practice seems to have the right balance of carrying capacity, management efforts, and other costs under the existing production procedures. The ecosystem model is a promising tool for further study with sustained observation effort and better boundary conditions.

1. Introduction

Aquaculture has contributed up to 46.8% of the world total seafood supplement in 2016, of which China had produced 49.2 Mt of cultured animals (fish, crustaceans, mollusks) and 14.5 Mt of cultured aquatic plants. This is accounting for about 61.5% and 48.0% of the world total production respectively (FAO, 2018). The high biomass produced from aquaculture has brought increased concerns on the pressure of coastal ecosystem and sustainability worldwide (Milewski, I., 2001; Cao et al., 2007; Ferreira et al., 2007; Whitmarsh D. and Palmieri M.G., 2008; Galparsoro et al., 2020). Integrated multi-trophic aquaculture (IMTA) is considered as an effective method for aquaculture productivity and sustainability. The theory behind IMTA is to recycle the nutrients and waste through integrating cultured species at different trophic levels (Chopin et al., 2001). Integrated aquaculture has been practiced in China for centuries (NACA, 1989), and a thriving commercial-scale IMTA of bivalves (currently Pacific oyster *Crassostrea gigas*) and seaweed (kelp *Saccharina japonica*) has been operated since the mid-1980s in Sanggou Bay, China. The bay has become a demonstration site for domestic and global research projects related to carrying capacity estimation and environmental impact assessment.

Sanggou Bay (Fig. 1) is a shallow semi-enclosed bay located at the east end of the Shandong Peninsula (37°01′ - 09′ N, 122°24′ - 35′ E). The bay's total area is about 144 km^2, with the topography deepening from the central coast to outside, and the average depth of about 7.5 m. Tidal currents, particularly the semi-diurnal constituents, dominate the flow in the bay (Zhao et al., 1996). Nearly two-thirds of the bay area have been occupied by bivalve and seaweed aquaculture, the annual production of kelp is estimated to be up to 84,500 tons in dry weight (Mao et al., 2018) and the annual production of shellfish is approximately 100,000 tons in wet weight (Zhang et al., 2009).

Fang et al. (1996) were the first to study the carrying capacity of cultured kelp using the nitrogen budget and estimated water exchange in Sanggou Bay, and the capacity was estimated to be about 54,000 Mt

* Corresponding author.
E-mail address: jiangzj@ysfri.ac.cn (J.I.A.N.G. Zengjie).

https://doi.org/10.1016/j.ecolmodel.2020.109181
Received 15 November 2019; Received in revised form 9 June 2020; Accepted 11 June 2020

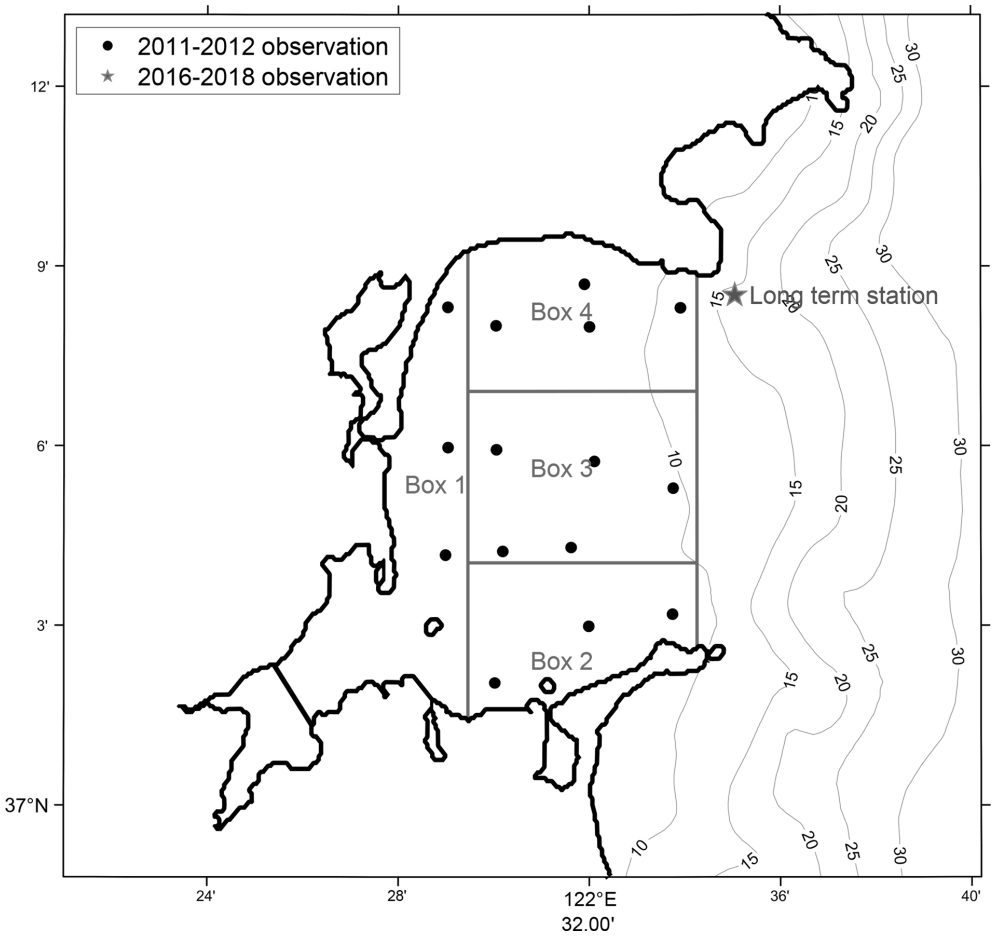

Fig. 1. The domain of the ecosystem model, the model is divided into 4 boxes based on similarities in geographical and exist aquaculture practice. The black dots are the sampling sites during 2011–2012, and the red star is the long-term sampling station for chlorophyll a and DIN since 2016. Culture organism were sampled at the farms near the long-term sample station, which has been used in the validation of individual models.

in dry weight. With the development of observation instruments and computing capabilities, numerical models have gradually become main tools to study the aquaculture sustainability. Jon Grant and Cedric Bacher (2001) have implemented a finite element circulation model to study the current modification by the culture structures for bivalves and seaweed in Sanggou Bay, which brought in the consideration of local hydrodynamics to the problem of carrying capacity. The simulation concluded a 41% decrease in the water exchange due to the presence of the aquaculture facilities, which may lead to an overestimation of particle renewal time, and as a result, thus overestimating the carrying capacity. Shi et al. (2011) have developed a three-dimensional physical-biological coupled model for Sanggou Bay, with a parameterized surface drag from culture structures. The kelp production, nitrogen budget, and current field were simulated for different culture densities to seek the optimum values for sustainable development.

From studies of carrying capacity of suspended oyster aquaculture in Québec, Canada, an oyster individual growth model was integrated into the ecosystem model, and hydrodynamic model results were used to compute water exchange at the box boundaries (Grant et al., 2007). The model results were useful in the management of sustainable development of local oyster industries. Guyondet et al. (2010) have coupled the dynamic energy budget (DEB) of cultured oysters to a nested fine resolution physical-biogeochemical model in the Gulf of Saint-Lawrence to study the interaction of oyster farms with the larger scale coastal ecosystem. Ren et al. (2012) have developed an ecosystem model for IMTA with multiple biological modules, including finfish, seaweed, shellfish, phytoplankton, zooplankton, carnivores, and benthic detritivores in Waihinau Bay and Pelorus Sound, New Zealand. In their study, hydrodynamic computed boundary volume fluxes drive the model defined physiological processes. These numerical models above parameterized the interactions between cultured organisms and the ecosystem components, and predicting individual growth and population state of targeted biological groups as well as the significantly correlated environmental variables. Ecosystem models often have specific regional characteristics, like the natural environment, the ecosystem compositions, the aquaculture method, and the bio-physiology of the cultured organisms. A general frameworks should be modified with detailed localization, calibration, and validation for use in solving specific problems.

The purpose of this study is to establish an ecosystem model to examine the interaction between the integrated aquaculture of bivalve

and seaweed and the local environment in Sanggou Bay. The model can be a tool to study the biogeochemical flux variation due to different culture management and to seek optimum aquaculture principles based on carrying capacity estimation.

2. Methods

2.1. Model description

The ecosystem model for the co-cultured oyster and kelp in Sanggou Bay is developed from several previous studies at the individual level for organism growth (Zhang et al., 2016; Cai et al., 2018; Ren et al., 2008) and at population level for biological group interaction (Grant et al., al.,2007; Ren et al., 2012; Filgueira et al., 2015). The model was established based on a typical Nitrogen-Phytoplankton-Zooplankton-Detritus (NPZD) model. Instead of zooplankton, Pacific oyster *C. gigas* is the model grazer because of the dominant biomass. Kelp *S. japonica* is introduced as an additional nutrient consumer. A concept diagram of the model is shown in Fig. 2. The ecosystem model is deterministic, with no random processes considered. It was simulated based on the box model concept with the identical structure in each box. The environmental terms including dissolved inorganic nitrogen (DIN), phytoplankton, and pelagic organic matter (particle organic carbon, POC) are assumed to be uniformly mixed in each box and properties can be exchanged with adjacent boxes and the outer sea. A hydrodynamic model was incorporated to compute the water volume exchange. The exchange of a given box at each time step is determined by the inflow and outflow volume, as $\Delta Ex = \frac{\sum(\Delta V_{in} \times Ex_{in} - \Delta V_{out} \times Ex_{out})}{V}$, where ΔV_{in} and ΔV_{out} are the inflow and outflow at each boundary, Ex_{in} and Ex_{out} are the concentration from inflow box and the target box, respectively. The exchange at each boundary is then summed up and divided by the target box volume V to obtain the concentration variation. The state variables and differential equations describing the aquaculture system are listed in Table 1. The biological processes and their definitions are listed in Table 2. The parameters and their sources are listed in Table 3. The detailed explanation can be found from referred studies (Zhang et al., 2016; Cai et al., 2018; Ren et al., 2008, 2012)

An Arrhenius relationship is used to describe the impact of the water temperature on the growth and respiration of phytoplankton, as the physiological rates increase exponentially with rising temperature until a maximum and then decrease with further temperature increase (Ren et al., 2012). The growth of phytoplankton is described by two state variables: the phytoplankton carbon (CP) and nitrogen (NP). The uptake of carbon (U_{cp}) and nitrogen (U_{np},) is internally connected by the N-quota (N:C ratio) to prevent the unrealistic absorption of carbon or nitrogen (Ren et al., 2012). The uptake of carbon is limited by temperature, irradiance, and the N-quota, and the uptake of nitrogen follows the Michaelis-Menten equation (Caperon and Meyer, 1972) which is a well-known model to describe the rate of enzymatic reactions. The biomass loss of phytoplankton consists of three processes: their own respiration, oyster grazing (U_{bp}), and natural sinking (M_p). The detailed parameterization of these biological processes is listed in Table 2.

The detritus in the model is described with the state variable particle organic carbon (POC). POC serves as food (U_{bo}) for cultured oyster in the model. Meantime, the feces (O_M) of oyster is also the source of the POC. The sedimentation of POC and the exchange (Ex_{POC}) between boundaries also change the concentrations.

Dissolved inorganic nitrogen (DIN) is the nutrient flux tracking the interaction among trophic groups within the system. Excretion of oysters (O_{excr}) is the biological source of DIN, while kelp (U_{nk}) and

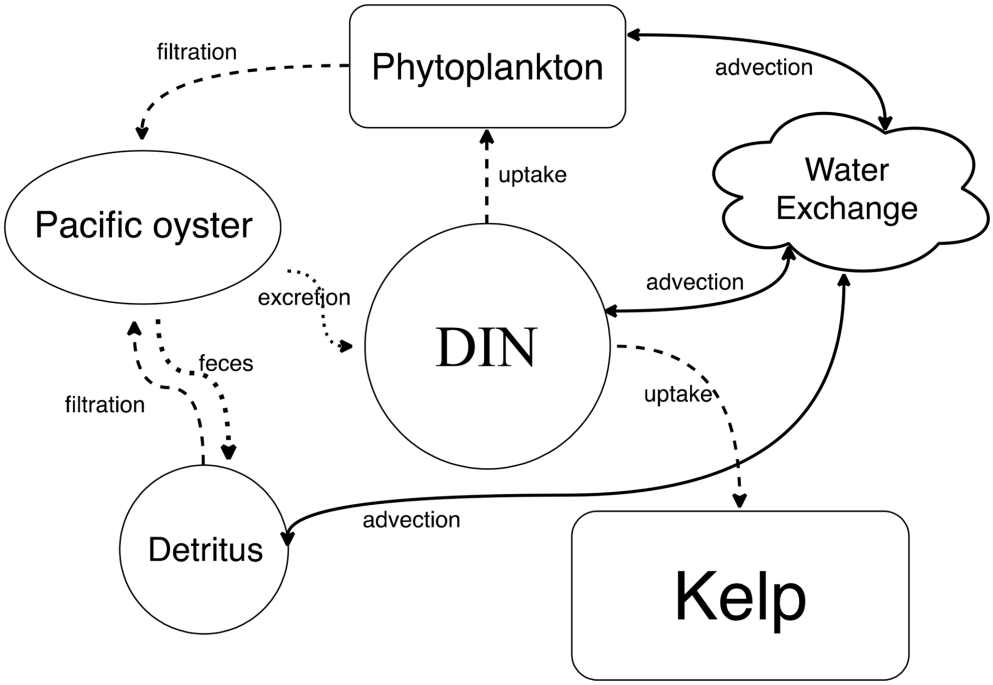

Fig. 2. Conceptual diagram of the ecosystem model implemented in Sanggou bay. The state variables are defined in Table 1 and the corresponding physiological rates are listed in Table 2. The cultured organisms are Pacific oyster Crassostrarea gigas and kelp Saccharina japonica, the major pelagic variables are phytoplankton, dissolved inorganic nitrogen (DIN) and detritus (represented by particle organic carbon). The bay is assumed to be vertically homogeneous, so the benthic processes are not considered for now.

Table 1
State variable and differential equations of the model.

Oyster			
Symbol	Equation	Description	Source
E	$dE/dt = p_A - p_C$	Reserves (j)	Ren et al. (2008)
E_R	$dE_R/dt = (1-\kappa)p_C - p_J$	Reproduction reserves (j)	
V	$dV/dt = (\kappa\, p_C - p_M)_+ / [E_G]$	Biovolume growth (cm^3)	
N	$dN/dt = -(\delta_r + \delta_h) \cdot N$	Population dynamics (No.)	Ren et al. (2012)
Kelp			
B	$d\,B/dt = growth - resp - erosion$	Kelp TDW (g)	Cai et al. (2018)
L	$L = exp\,[ln\,(B \cdot 10^{6.28}/3.35)]$	Kelp length (cm)	
N_{int}	$d\,N_{int}/dt = \varphi - \gamma$	Tissue nitrogen (μmol N/g TDW)	
A	$dA/dt = -(\delta_r + \delta_h) \cdot A$	Population dynamics (No.)	This study
Ecosystem model			
CP	$d\,CP/dt = U_{cp} - r_p \cdot f(T)_p \cdot CP - U_{bp} \cdot N/V_{box} \cdot Mp + Ex_{CP}$	Phytoplankton carbon (mgC/ m^3)	Ren et al. (2012)
NP	$d\,NP/dt = (1-e_{up}) \cdot U_{np} - r_p \cdot f(T)_p \cdot NP - Q_p \cdot U_{bp} \cdot N/V_{box} - Q_p \cdot M_p + Ex_{NP}$	Phytoplankton carbon (mgN/ m^3)	
POC	$d\,POC/dt = O_m\,N/V_{box} - U_{oo}\,N/V_{box} - \lambda_0\,POC + Ex_{POC}$	Detritus particle organic carbon (mgC / m^3)	
DIN	$d\,DIN/dt = O_{excr} \cdot N/V_{box} - U_{np} - U_{nk} \cdot A/V_{box} + Ex_{DIN}$	Dissolved inorganic nitrogen (mgN/ m^3)	

Notes: The expression $(x)+$ is defined as: $[x]+ = x$ for $x > 0$, $[x]+ = 0$ otherwise.

Table 2
Biological process.

Oyster				
Symbol	Description	Formula	Unit	Source
f	Function response of oyster	$F/(F + F_H)$	–	Ren et al. (2012)
T_{emp}	Temperature-dependence rate of oyster	$k_0 \cdot exp\,(T_A/T_0\text{-}T_A/T) \cdot [1 + exp(T_{AL}/T\text{-}T_{AL}/T_L) + exp(T_{AH}/T_H\text{-}T_{AH}/T)]^{-1}$	–	
U_{bp}	Consumption rate of oyster on phytoplankton	$T_{emp} \cdot U_{mm} \cdot CP \cdot V^{2/3}$	mgC d^{-1}	
U_{bo}	Consumption rate of oyster on POC	$T_{emp} \cdot U_{mm} \cdot POC \cdot V^{2/3}$	mgC d^{-1}	
p_A	Assimilation rate of oyster	$T_{emp} \cdot f \cdot \{p_A\} \cdot V^{2/3}$	J d^{-1}	
p_C	Catabolic rate of oyster	$T_{emp} \cdot [[E]/([E_G] + \kappa \cdot [E])] \cdot ([E] \cdot \{p_A\} \cdot {}^{2/3}/[E_m] + [p_M] \cdot V)$	J d^{-1}	
p_M	Maintenance rate of oyster	$T_{emp} \cdot \{p_M\} \cdot V$	J d^{-1}	
p_J	Maturity maintenance rate of oyster	$\min(V, V_p) \cdot [p_M] \cdot (1-\kappa)/\kappa$	J d^{-1}	
O_m	Feces of oyster	$U_{op} + U_{oo} - p_A/\mu_{CJ}$	mgC d^{-1}	
O_{excr}	Oyster excretion	$\{[p_C - (1-\kappa_R) \cdot dE_R/dt - \mu_V \cdot \rho \cdot dV/dt] \cdot Q + p_A \cdot (Q_p - Q) + \}/\mu_{CJ}$	mgN d^{-1}	
W_o	Individual wet weight of oyster	$V \cdot \rho + (E + E_R \cdot \kappa_R)/\mu_E$	g	
Kelp				
growth	Kelp growth rate	$\mu_{max} \cdot f(T) \cdot f(I) \cdot f(N)$	–	Cai et al. (2018)
resp	Kelp respiration rate	$R_{max20}\,{}^{\circ}_{C} \times \theta^{(T-20)}$	–	
erosion	Kelp erosion rate	$E_{max} \cdot p^{(T\text{-}Topt)}$	–	
I	Irradiance at culture depth	$I_0 \cdot exp\,(-k \cdot Z)$	μmol·m^{-2}·s^{-1}	
$f(I)$	Irradiance effect on kelp growth	$(I/I_{opt})\ exp\ (1\text{-}I/I_{opt})$	–	
$f(T)$	Temperature effect on kelp growth	$exp\ \{-2.3 \cdot [(T\text{-}T_{opt})/(T_x\text{-}T_{opt})]^2\}$	–	
$f(N)$	Nutrient effect on kelp growth	$(N_{int} - N_{imin})/(K_q + N_{int} - N_{imin})$	–	
φ	External DIN absorption rate	$[(N_{imax} - N_{int})/(N_{imax} - N_{imin})] \cdot V_{maxN} \cdot [DIN/(K_N + DIN)]$	μmol N/g TDW d^{-1}	
γ	Tissue assimilated DIN	$N_{int} \cdot Growth$	μmol N/g TDW d^{-1}	
U_{nk}	Individual external DIN absorption	$\varphi \cdot B \cdot (14/1000)$	mgN / ind	This study
Phytoplankton				
$f(T)_p$	Temperature effect rate of phytoplankton	$k_{0p} \cdot exp\,(T_{Ap}/T_{0p}\text{-}T_{Ap}/T) \cdot [1 + exp\,(T_{ALp}/T\text{-}T_{ALp}/T_{Lp}) + exp(T_{AHp}/T_{Hp}\text{-}T_{AHp}/T)]^{-1}$	–	Ren et al. (2012)
$f\ (I)_p$	Irradiance effect on carbon uptake	$(1/H) \cdot \int_0^H \frac{I}{I + X_I} dz$	–	
U_{dinp}	Potential uptake of DIN by phytoplankton	$U_{nmaxp} \cdot (DIN/(DIN + X_{pdin}))$	d^{-1}	
U_{np}	Total uptake of N by phytoplankton	$NP \cdot f(T)_p \cdot U_{dinp}/\{1 + exp[(Q_p - Q_{pmax})/Q_{poff}]\}$	mgN d^{-1}	
U_{cp}	Total uptake of C by phytoplankton	$f\ (I)_p \cdot CP \cdot f(T)_p \cdot G_{pm} \cdot (1 - Q_{pmin}/Q_p)_+$	mgC d^{-1}	
Q_p	Phytoplankton N quota	NP/CP	–	
M_p	Phytoplankton C sinking rate	$CP \cdot [\delta_{pmin} + \delta_p \cdot (Q_{pmax} - Q_p)_+]$	mgC d^{-1}	

Notes: The expression $(x)+$ is defined as: $[x]+ = x$ for $x > 0$, $[x]+ = 0$ otherwise.

phytoplankton (U_{np}) absorb DIN from the system. As the ecosystem is dominated by kelp aquaculture, the DIN exchange with the outer sea is crucial for the nutrient supplement.

The individual-based model applied in this study for oyster follows Ren et al. (2008). The three state variables to describe the energetics of the oyster are: reserves (E), reproduction reserves (E_R), and biovolume (V). The reserves are replenished with assimilated energy (p_A) deducting the metabolic expenditure (p_C). Food availability and temperature are the major factors that determine oyster growth. The temperature limitation of the oyster is formulated as an Arrhenius relationship that affects most of the physiological processes. The energy uptake follows a type-II functional response to food density, which assumes a deaccelerated rate with food density (Holling, C. S., 1959), described as $f = F/(F+F_H)$, where F is the food concentration, and F_H is

Table 3
Parameters for the ecosystem model.

Parameter	Description	Value	Unit	Source
F_H	Half-saturation uptake of phytoplankton by oyster	4.3	μg/L	Calibrated
T_A	Arrhenius temperature of oyster	5900	K	Ren et al. (2008)
T_L	Lower boundary of tolerance range for oyster	283	K	Ren et al. (2008)
T_H	Upper boundary of tolerance range for oyster	303	K	Ren et al. (2008)
T_{AL}	Arrhenius temperature at lower boundary for oyster	13,000	K	Ren et al. (2008)
T_{AH}	Arrhenius temperature at upper boundary for oyster	80,000	K	Ren et al. (2008)
k_0	Reference reaction rate for oyster at 291 K	1	–	Ren et al. (2008)
U_{mm}	Oyster maximum surface area-specific clearance	0.045	$m^3\ cm^{-2}\ d^{-1}$	Ren et al. (2012)
$\{p_A\}$	maximum surface area-specific assimilation rate	560	$J\ cm^{-3}\ d^{-1}$	Poureau et al. (2006)
$[p_M]$	Volume-specific maintenance costs	24	$J\ cm^{-3}\ d^{-1}$	Poureau et al. (2006)
$[E_G]$	Volume-specific costs for oyster growth	2900	$J\ cm^{-3}$	Ren et al. (2008)
$[E_m]$	maximum storage density	5900	$J\ cm^{-3}$	Ren et al. (2008)
V_p	Structural volume at sexual maturity	0.4	cm^{-3}	Poureau et al. (2006)
κ	Fraction of p_C spent on maintenance plus growth	0.65	–	Ren et al. (2008)
κ_R	Fraction of reproduction energy fixed in eggs	0.7	–	Ren et al. (2008)
μ_E	energy content of reserves	4500	$J\ g^{-1}$ wet W	Ren et al. (2012)
μ_{CJ}	Ratio of carbon to energy content	48.8	$J\ mgC^{-1}$	Ren et al. (2012)
μ_V	Structure energy content	2700	$J\ g^{-1}$ wet W	Ren et al. (2012)
ρ	Biovolume density of cultured animals	1	g wet W cm^{-3}	Ren et al. (2012)
Q	N-quota of oyster	0.183	mgN mgC^{-1}	Ren et al. (2012)
μ_{max}	Kelp maximum daily growth rate	0.115	d^{-1}	Calibrated
$R_{max20\ °C}$	Kelp maximum respiration rate at 20 °	0.015	d^{-1}	EPA, 1985
θ	Empirical value for kelp respiration	1.02	–	Cai et al.(2018)
E_{max}	Daily mean erosion of kelp	0.006	d^{-1}	Cai et al.(2018)
P	Empirical value for kelp erosion	1.05	–	Cai et al.(2018)
I_{opt}	Optimum irradiance for kelp photosynthesis	350	$\mu mol{\bullet}m^{-2}{\bullet}s^{-1}$	Cai et al.(2018)
T_{opt}	Optimum temperature for kelp growth	12	°C	Cai et al.(2018)
T_{max}	Upper temperature limit above which growth ceases	20	°C	Cai et al.(2018)
T_{min}	Lower temperature limit below which growth ceases	0.5	°C	Cai et al.(2018)
N_{imin}	Minimum internal quota for nitrogen	300	μmol g DW^{-1}	Cai et al.(2018)
N_{imax}	Maximum internal quota for nitrogen	1714	μmol g DW^{-1}	Cai et al.(2018)
K_N	Half-saturation constant for nitrogen uptake	29	$\mu mol\ L^{-1}$	Cai et al.(2018)
V_{maxN}	Maximum nitrogen uptake rate	246.72	μmol g $DW^{-1}\ d^{-1}$	Cai et al.(2018)
K_q	Half-saturation constant for nitrogen assimilation	400	μmol N•gdw^{-1}	Calibrated
Z	Kelp aquaculture depth	0.2	m	Zhang et al.(2016)
T_{Ap}	Arrhenius temperature of phytoplankton	6800	K	Ren et al. (2012)
T_{Lp}	Lower boundary of tolerance range for phytoplankton	286	K	Ren et al. (2012)
T_{Hp}	Upper boundary of tolerance range for phytoplankton	298	K	Ren et al. (2012)
T_{ALp}	Arrhenius temperature at lower boundary for phytoplankton	27,300	K	Ren et al. (2012)
T_{AHp}	Arrhenius temperature at upper boundary for phytoplankton	80,300	K	Ren et al. (2012)
k_{0p}	Reference reaction rate for phytoplankton at 292 K	1	–	Ren et al. (2012)
U_{nmaxp}	Phytoplankton maximum uptake of DIN	0.5	d^{-1}	Ren et al. (2012)
X_{pdin}	Half-saturation DIN for phytoplankton uptake	28	mgN m^{-3}	Calibrated
Q_{pmax}	Maximum phytoplankton N:C ratio	0.25	mgN mgC^{-1}	Ren et al. (2012)
Q_{pmin}	Minimum phytoplankton N:C ratio	0.1	mgN mgC^{-1}	Ren et al. (2012)
Q_{poff}	Phytoplankton nitrogen uptake parameter	0.01	mgN mgC^{-1}	Ren et al. (2012)
G_{pm}	Maximum phytoplankton growth rate	1.6	d^{-1}	Ren et al. (2012)
X_I	Half-saturation light level	7	$\mu mol\ m^{-2}d^{-1}$	Ren et al. (2012)
e_{up}	Uptake associated excretion of phytoplankton	0.005	–	Ren et al. (2012)
δ_{pmin}	Minimum phytoplankton sinking rate	0.1	d^{-1}	Ren et al. (2012)
δ_p	Maximum phytoplankton sinking rate	0.25	d^{-1}	Ren et al. (2012)
δ_r	Natural mortality of oyster/kelp	0.001	d^{-1}	Ren et al. (2012)
δ_h	Harvest mortality of oyster/kelp	1	d^{-1}	Ren et al. (2012)

the half-saturation coefficient for food uptake by oysters. The energy acquired is then distributed according to the κ-rule (Kooijman, 2010): a fixed fraction of κ is utilized in body maintenance (p_M) and growth which lead to a increase in biovolume, and the remaining 1-κ fraction is allocated to reproduction. Detailed equations and definitions of the state variables and biological processes can be found in Table 1 and Table 2. The biological function of the oyster is to graze phytoplankton and particle organic matter from the surrounding water and to excrete nitrogen and feces into the system. The population dynamics of oyster (N) is determined by culture harvest (δ_h) and natural mortality (δ_r). When harvested, the oyster is removed from the system. The natural mortality will lead to a continuous biomass loss during the simulation.

The growth of kelp is simulated with an individual growth model from Zhang et al. (2016) and Cai et al. (2018). Three state variables are used to describe kelp growth: the individual kelp biomass (B), kelp length (L), and the tissue nitrogen content (N_{int}). The individual kelp biomass variation is defined as growth minus respiration and erosion. Growth of kelp is defined as a maximum growth rate (μ_{max}) multiplied by a limiting factors (from 0 - 1) due to water temperature, light intensity, and nutrients concentration (Table 2). The temperature limitation $f(T)$ is an exponential function to produce a partial normal distribution according to the optimum temperature for kelp growth (Radach et al., 1993). For simplicity, only the nitrogen limitation $f(N)$ is considered (Cai et al., 2018), and is calculated by the Michaelis-Menten equation. The light limitation $f(I)$ is defined according to Steele (1962) with the optimum light intensity I_{opt}. The kelp respiration rate and erosion rate, limited by temperature, are parameterized with a similar exponential form (Table 2). The uptake of external DIN by kelp (φ) also follows a Michaelis-Menten function based on the tissue nitrogen content. The population dynamics of kelp (A) is the same as the oyster.

Currently, no stochastic processes (disease and disaster) are considered. As we assume a thorough vertical mixing in the bay, the benthic processes are not considered in the model of this study.

2.2. Study area and hydrodynamics

The model is applied to Sanggou Bay, and the domain is separated into four boxes according to hydrodynamic and aquaculture layout similarities, as shown in Fig. 1. The volumes for Box 1 to 4 are 0.367 km^3, 0.239 km^3, 0.504 km^3, and 0.352 km^3; and the average depths for each box are 6.3 m, 7.3 m, 8.0 m and 8.1 m, respectively. The aquaculture in Sanggou Bay mainly takes place in Box 2, Box 3 and Box 4. Due to the shallow water depth, little aquaculture can be found in Box 1, so we neglect the culture activities there. The hydrodynamic properties of each box are simulated with the Finite-Volume Coastal Ocean Model (FVCOM, Chen et al., 2006), and the details are described by Xuan et al. (2019). In brief, the model was implemented on an unstructured grid with the horizontal grid resolution varying from 50 - 400 m in the study area, and there are 20 vertical σ-layers. The model was forced by atmospheric data from ECMWF ERA-interim (European Medium-Range Weather Forecast, atmospheric reanalysis, https://ecmwf.int), tidal data from TPXO 7.0 (Egbert and Erofeeva, 2002), and the ocean current from the Hybrid Coordinate Ocean Model (Bleck, 2002). The model was run for the period from July 2010 to June 2011, and the results include hourly depth-averaged current, water temperature, and salinity interpolated to a rectangular grid with a horizontal resolution of 100 m. An offline coupled water quality model was implemented to simulate the environmental variables, including DIN, POC, and phytoplankton (Chlorophyll-a concentration) following Xuan et al. (2019). In this study, model current results were used for the volume exchange estimation between boxes and the outer boundary, and the water temperature time series were used for estimation of physiological rates. The water quality model results were used as the far-field boundary forcing of the ecosystem model.

2.3. Observations

The biophysical data for model validation and optimization is from previous observational data and is summarized in Table 4. For the DEB model of oyster, shell height (cm) and tissue wet weight (TWW) data were recorded from 20 samples approximately twice a month from August 2016 to February 2017. The sampling location is shown in Fig. 1 at the long-term station. The corresponding surface chlorophyll-a concentration and the water temperature were also recorded by a JFE Advantec Infinity-CLW fluorometer with a time interval of 4 h. For the individual growth of kelp, around ten samples were collected every month from February 2018 to June 2018. The kelp samples are mostly taken close to the long-term station, and the kelp length and tissue dry weight (TDW) were measured each time. The water temperature and DIN concentration in the kelp farming area were measured every month. DIN from previous cruises during 2011–2012 was collected and assigned to each box according to sampling sites (Fig. 1).

2.4. Model setup

Most of the parameters in the individual models and the ecosystem model are taken from previous studies, and the values and sources are listed in Table 3. In terms of the difference in geographical conditions, some parameters (e.g., oyster half-saturation food uptake concentration, maximum phytoplankton/kelp daily growth rate, etc.) were calibrated and validated using previous local studies and observations. Calibrated parameters were applied to all models for consistency.

Validation runs were conducted for the individual models and the ecosystem model, and the results were compared to observations. For the oyster, observed chlorophyll-a and water temperature data from 2016 - 2017 were used as the external driving force for the DEB model with a time interval of 4 h (Δt = 1/6 day). The initial reserve energy for oyster was set as 40 J, the reproductive reserve was set as 10 J. The initial biovolume was 0.6 cm^3, with an initial oyster TWW being around 0.2 g. For kelp, the individual model was forced with the observed interpolated DIN and water temperature during 2017 - 2018, the monthly values were interpolated to a time series with an interval of 6 h (Δt = 1/4 day). From Cai et al. (2018), the hourly averaged light intensity was set constant (irradiance: 340 $\frac{\mu mol}{m^2\ s}$). The initial kelp biomass tissue dry weight (TDW) is set at 0.5 g for all boxes, and the initial tissue internal nitrogen (N_{int}) is set as 1071 $\frac{\mu mol}{g\,DW}$ (Zhang et al., 2016). For the performance test of the ecosystem model, the initial values of phytoplankton, POC, and DIN concentration were set equal to box-averaged water quality model results. The averaged culture density, which is necessary to represent the situation with varieties of aquaculture companies and self-employed households, is scaled as individuals per m^2 for oyster and kelp. Currently, oyster culture in Sanggou Bay starts around June and usually lasts for 12 months. Then they are transferred to another region to fatten up to market size. Given the existing aquaculture spatial distribution, oysters were cultured only in Box 3 with a farm density of around 50 ind./m^2. The kelp was cultured in Box 2, Box 3 and Box 4 with the seeding starting in November and the harvest starting in May. The culture density was estimated to be 4 - 5 kelps per m^2 (Mao et al., 2018). The individual model results were compared to observations for performance evaluation. The ecosystem model results were compared to data from the previous cruise and moored devices for the magnitude and seasonal cycle of the environmental variables.

The ecosystem model equations were computed with the open-source programming language Python 3.7 (https://www.python.org/) .

2.5. Scenario simulation

The ecosystem model was run for ten scenarios representing different seeding combinations. Scenario III is the validation simulation that represents the existing aquaculture practice. Scenarios I toVI aimed to study the response of the phytoplankton and production with different oyster seeding densities under a fixed amount of cultured kelp. Scenarios III, VII, VIII, IX, X aimed to study the growth and environmental feedback of different kelp seeding densities under a fixed number of cultured oyster. The combinations are summarized in Table 5.

3. Results

3.1. Model validation

The comparisons of simulated and observed values of oyster TWW are showed in Fig. 3, together with the time series of water temperature

Table 4
Observation information.

Year	Measurement	Frequency	Method
2011–2012	Dissolved inorganic nitrogen (NH_4, NO_3, NO_2)	2011.04; 2011.08; 2011.10; 2012.01	Water samples from cruise
2016.8–2017.2	Oyster shell length, shell height, DFW	~ twice per month	20 oyster samples per measure
2016.6–2017.8	Surface water temperature/Chlorophyll a	Every 4 h	JFE Advantec Infinity-CLW fluorometer hanged about 0.2 m below surface
2018.2–2018.6	Kelp TDW, length, width	Every month	10 kelp samples per measure
2017.11–2018.10	DIN (NH_4, NO_3, NO_2), surface water temperature	Every month	Water samples in the kelp culture area

Table 5
Scenarios of the ecosystem simulation.

Scenario	Oyster (ind./ha; Box 3)	Kelp (ind./ha; Box 2, Box 3, Box 4)
I	0	40,000
II	300,000	40,000
III	500,000	40,000
IV	700,000	40,000
V	1000,000	40,000
VI	1500,000	40,000
VII	500,000	50,000
VIII	500,000	60,000
IX	500,000	70,000
X	500,000	80,000

and the chlorophyll-a concentration. Error bars represent the standard deviation for each measurement of 20 oysters. The simulated oyster growth starts in May, which is approximately the seeding time of the sampled oysters. Both the observed and simulated oysters showed rapid growth from August with suitable temperature and relatively abundant food and tended to slow down after November as the environment changes. As the oyster grows, the TWW tends to be diverse as a result of individual differences. The most substantial standard deviation is 2.6 g, which is about 27% of the mean value. The simulated results have reproduced the growth situations, the root-mean-square error between the observation and the simulations is 0.6 g. However, the simulated growth of oyster slightly deviates from the observation after December as it showed a continuous but small growth. The simulated oyster did not spawn in the first year as the gonad index did not reach 35%. The oyster spawned as the model ran to next August, and approximately a 40% weight drop was predicted as the gonad emptied.

The comparison of simulated kelp tissue dry weight and the observed values are shown in Fig. 4, together with the corresponding environmental data and the 6-hourly interpolated curve. The observations are mean kelp TDW (g) from 10 samples of the same farm. Error bars represent the standard deviation for each measurement. Harvest of kelp begins in May and lasts until late August. In the simulation, the kelp was cultured to the end of November, with a computational time step of 6 h. The simulated and observed kelp growth showed the right consistency of the general trend of the TDW increase. The root-mean-square error is 17.03 g for the modeled and observed values. Although the model tends to underestimate the TDW during April when the kelp starts to proliferate, a precise growth condition reproduction of the cultured organism is difficult. The model is applicable to describe the kelp growth with reasonable forcing and uncertainties.

Fig. 5 compares simulated phytoplankton biomass (converted to chlorophyll-a with a ratio of phytoplankton carbon: Chl-a = 40) of each box with the observed chlorophyll-a during 2016–2017 near the long-term station. The ecosystem model reproduced the proper chlorophyll-a content and the seasonal variation during the vigorous growth seasons from May to October. However, when kelp was cultured, the Chlorophyll-a development was not captured fully and underestimated in the model. The magnitude of general Chlorophyll-a content, and the short-term peaks and valleys induced by water exchange are well reproduced in the model results.

Fig. 6 compares simulated DIN in each box with the observed values averaged from sample sites during 2011–2012. A ratio of 14 is used to convert the unit from mgN/m^3 to μmol/L. Although the simulation period is different from the observations, the simulated seasonal variation confirms the trend. With the absence of kelp in July, the DIN in each box is above 10 μmol/L. During winter, the simulated DIN remained at a high level around 12.5 μmol/L, but the observed values already dropped to around 7.5 μmol/L in January, indicating that the kelp growth is underestimated in the model. When the kelp starts to proliferate around March, the modeled DIN decreases sharply. As harvest starts in May, the kelp growth slows down, and the modeled DIN stabilized at a low level around 2.5 μmol/L for Box 3 and Box 4. After the kelp is harvested in June, the DIN in the ecosystem model rapidly recovered for each box according to the outer boundary constraints.

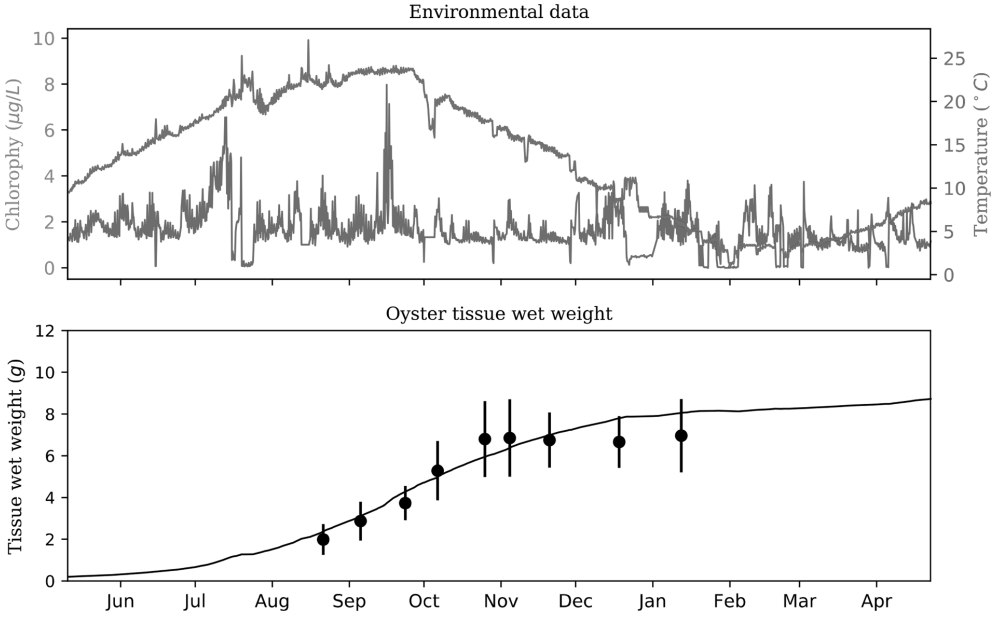

Fig. 3. Upper panel: environmental driving data (temperature and chlorophyll a) from observation during the simulation period. Lower panel: comparison of observations (dots) and simulation (line) of tissue wet weight (TWW) of cultured Pacific oyster in Sanggou bay during the observation period in 2016/2017, where errorbars are the standard deviation of observed TWWs.

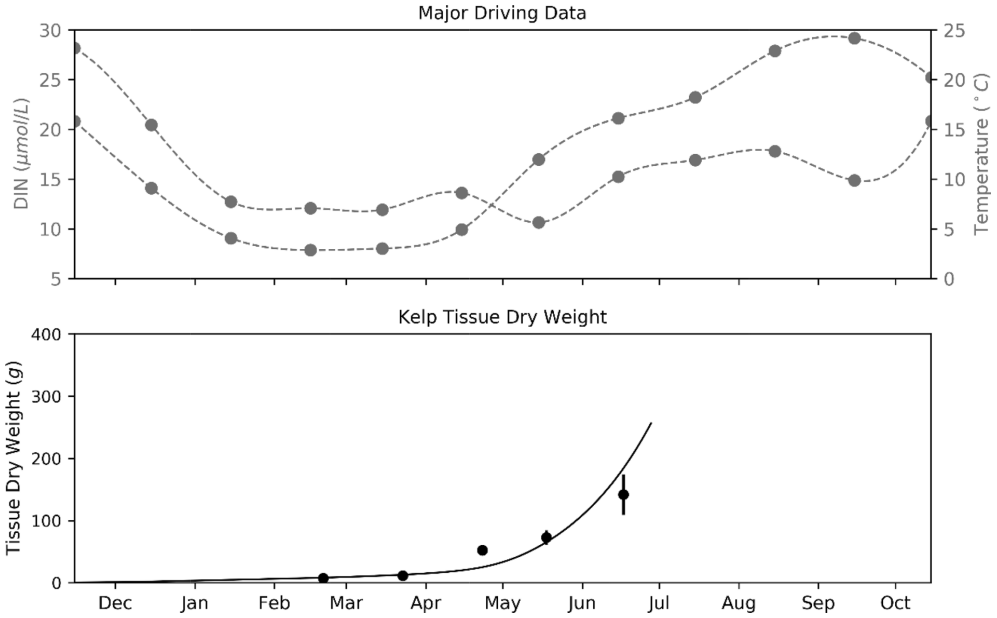

Fig. 4. Upper panel: environmental data (dissolved nitrogen and temperature) from observation (dots) and interpolated to a time sequence with $\Delta t = 1/4$ day. Lower panel: comparison of the simulated kelp tissue dry weight (solid line) and observed TDW from aquaculture in Sanggou Bay (dots) during the simulation period in 2018.

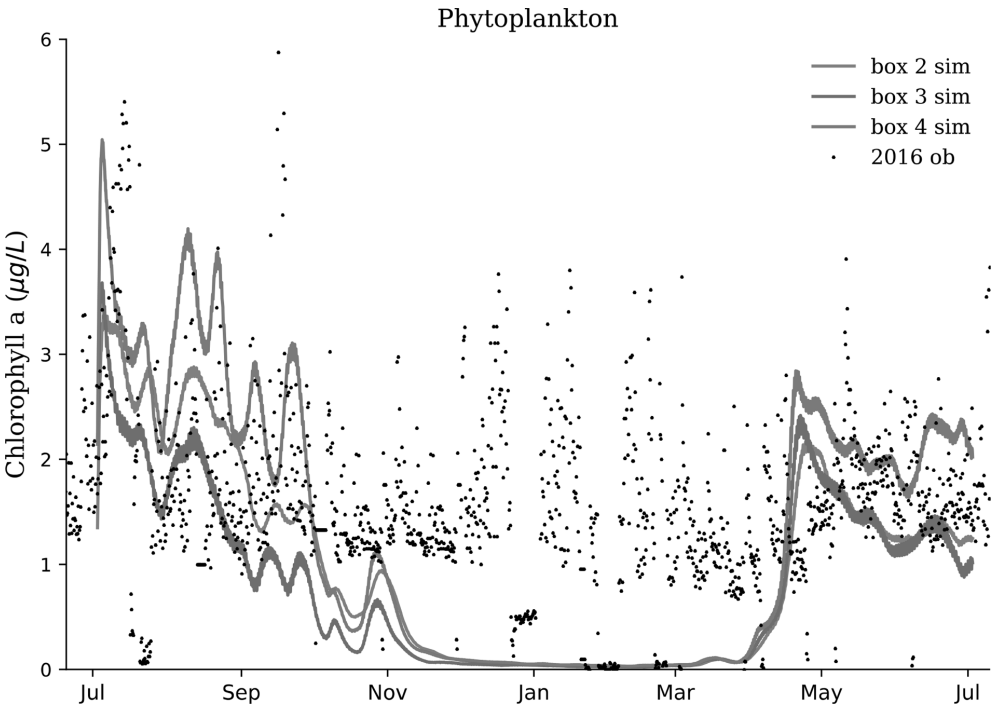

Fig. 5. Comparison of simulated Chlorophyll a concentration (lines) for Box 2 (red), Box 3 (blue) and Box 4(green) and the observed chlorophyll a (black dots) during 2016–2017 at the long-term station.

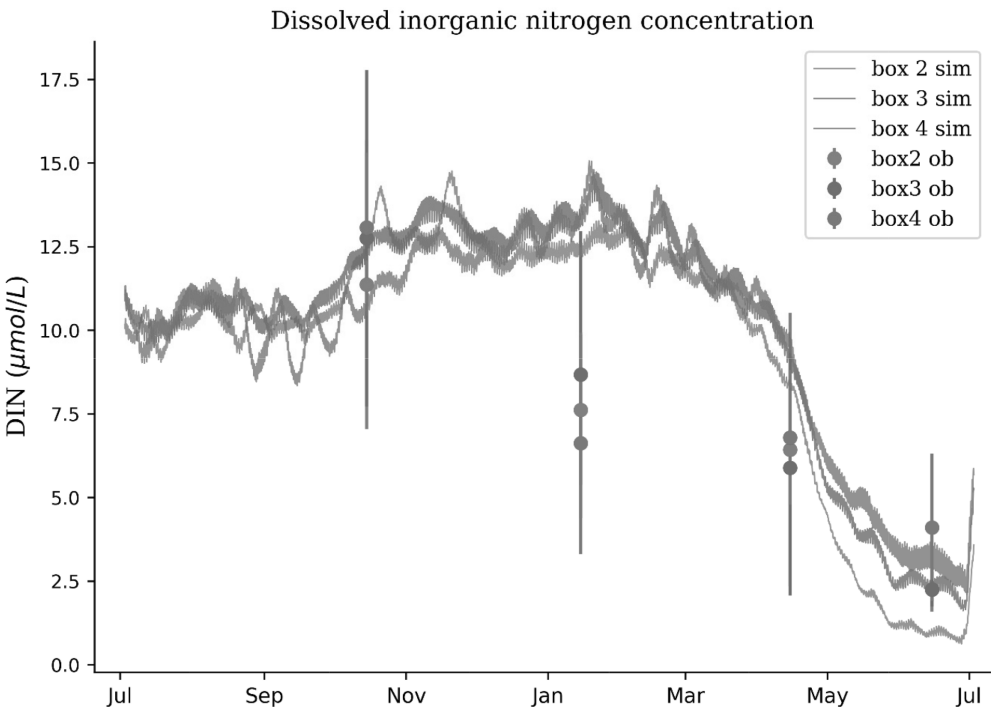

Fig. 6. Comparison of simulated DIN (lines) for Box 2 (red), Box 3 (blue) and Box 4(green) and the corresponding observed DIN (dots) during 2011–2012 in the same period of the year. The observed DIN is averaged for from the sample location within each box showed in Fig. 1. The standard deviation of observed dots is also shown in the figure.

The observed DIN for each box was averaged from water samples taken from cruises in 2011–2012 (Fig. 1). The standard deviation was large across each box.

With these limitations, the model properly reproduced the magnitude and seasonal cycle of the environmental variables.

3.2. Pacific oyster C. gigas

The individual oyster TWW growth under scenarios I~VI are shown in Fig. 7, and the corresponding phytoplankton biomass in Box 3 is also displayed. The simulation results illustrated that oyster growth decrease with increased seeding density. The individual TWW at the end of the culture period for scenarios II~VI are 7.81, 5.77, 4.63, 3.59, 2.64 g/ind., respectively, and such decrease is non-linear. For Scenario I, there is no oyster cultured. The presence of oyster imposed a feeding pressure on the phytoplankton, and a significant drop of phytoplankton concentration is observed for scenarios II, III, IV, V, and VI. The available phytoplankton (AP_n) for individual oyster under different scenarios can be defined as $\frac{\overline{CP_0}-\overline{CP_n}}{n}$, where $\overline{CP_n}$ is the mean Chlorophyll-a averaged from the culture period with the seeding density of n and $\overline{CP_0}$ is the mean Chlorophyll-a for no oyster situation. The values of available phytoplankton are 0.024, 0.017, 0.014, 0.011 and 0.008 μg Chl-a / (L ind.) for scenarios II~VI, respectively. Regression analysis of the final oyster TWW and the available phytoplankton for all seeding densities showed a significant linear correlation with the r-value of 0.99 and p-value of 7.6×10^{-7}. Increased oyster numbers have diminished the available phytoplankton resource for each individual, and lead to a declined expectancy of oyster growth.

The harvested oyster TWW, oyster production (kg WW/ha), phytoplankton depletion rate (%), and the production efficiency (-) for each seed density are shown in Fig. 8. The oyster production per ha is calculated as $P_n = W_n \times N$, where W_n is the oyster individual TWW, and N is the harvested oyster numbers for initial seeding density n. The phytoplankton depletion rate is calculated as DR. $= \frac{\overline{CP_0}-\overline{CP_n}}{\overline{CP_0}} \times 100\%$. The production efficiency (PE) is defined as the summed seed TWW divided by the final oyster production per ha. The simulated production after one year is 1627, 2002, 2247, 2292, and 2744 kg WW/ha for scenarios II-VI. Less culture density has led to better individual growth. However, the production is increasing with the culture density under the pre-defined constant mortality of 0.1%/day. The phytoplankton depletion increased as more oysters are cultured in the box. The values are 43.2%, 52.4%, 58.2%, 64.0% and 70.0% for scenarios II-VI. As the least seeding density simulated, 30 oysters cultured per m^2 still lead to more than 43% depletion of the phytoplankton. When seed density was increased by five times, the phytoplankton depletion increased to 70%. The production efficiencies are 8.8, 6.5, 5.2, 4.1 and 3.0 for scenarios II-VI.

3.3. Kelp S. japonica

The individual kelp tissue dry weight (TDW) growth under scenarios III for Box 2, Box 3 and Box 4 are shown in Fig. 9, and the corresponding DIN concentration is also displayed for each box. The kelp grows differently in each box under different environmental conditions. The maximum TDWs are 166.5, 210.8 and 229.2 g/ind. for Box 2, Box 3 and Box 4. Box 2 has less nutrients compared to the other two boxes; the supply of DIN is insufficient to maintain a high growth since May. The kelp in Box 3 and Box 4 maintain a relatively high growth until June, and as Box 4 has the most abundant DIN supply, the final TDW of kelp in Box 4 is higher than that in Box 3. Similar trends of kelp growth and DIN variation were observed for scenarios VII - X, the maximum

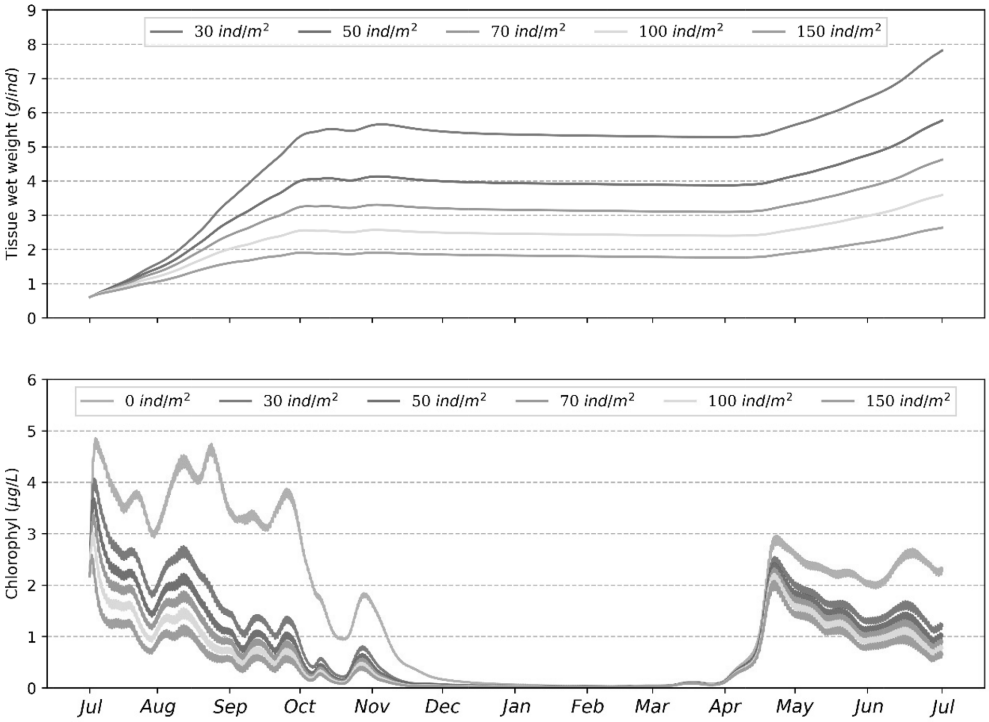

Fig. 7. Model results for different oyster culture scenarios within Box 3, totally 6 scenarios are set with no oyster culture, 30 ind./m^2, 50 ind./m^2, 70 ind./m^2, 100 ind./m^2 and 150 ind./m^2. Upper panel showed the individual tissue wet weight (g) time series of oysters for each scenario. The lower panel showed the corresponding phytoplankton variation and the situation with no oyster aquaculture in Box 3.

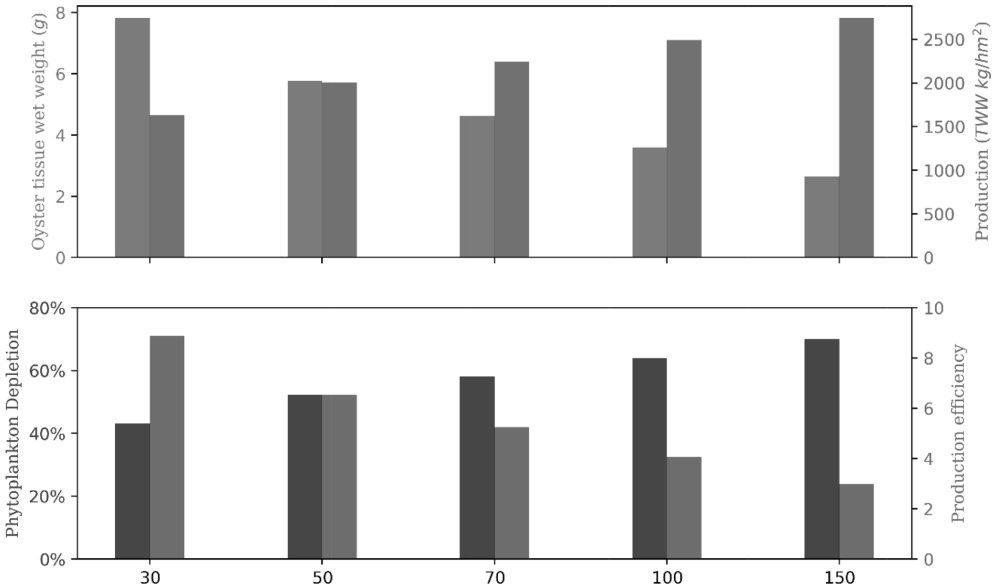

Fig. 8. Upper panel: the individual oyster tissue wet weight (blue) and the production (red) per ha for each oyster culture density. Lower panel: the phytoplankton depletion compared to no oyster scenario (dark red) and the production efficiency (green) for each oyster culture density.

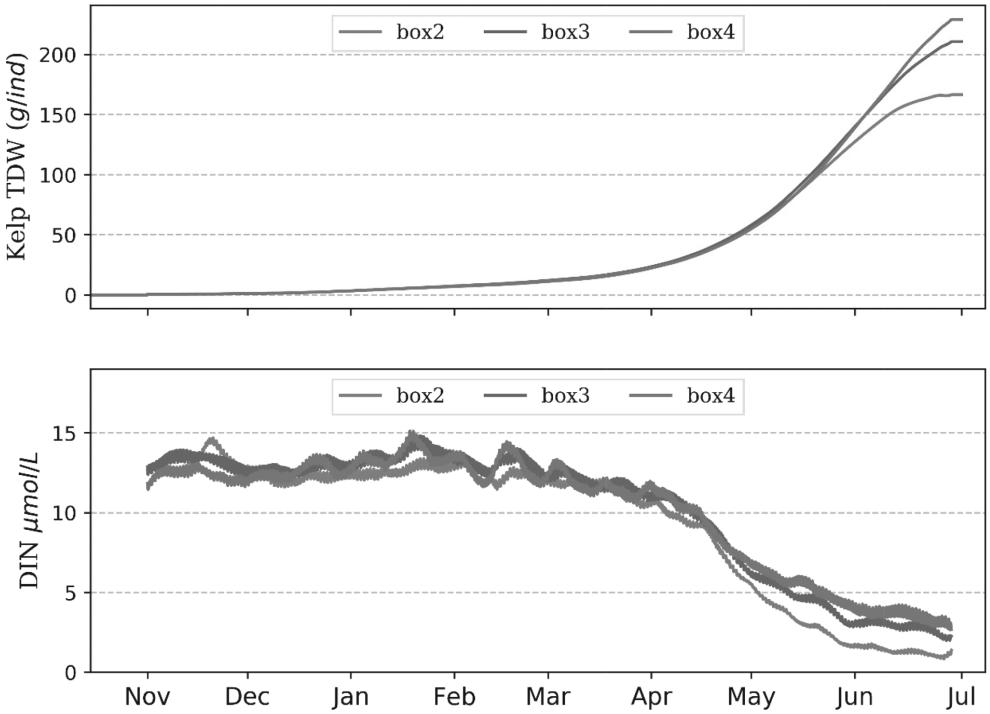

Fig. 9. Upper panel: individual tissue dry weight of kelp in each box from scenario III since November when the kelp is seeded. Lower panel: The corresponding DIN concentration during the simulation in each box for scenario III.

kelp TDW became smaller, and the mean DIN content level was lower with increased kelp seeding density.

The kelp TDW production (ton/ha) for each box and the expected individual TDW (g) at harvest for different seeding density are shown in Fig. 10. The kelp is harvested on the 15th of June, and the production is then calculated through multiplying the individual TDW by harvested numbers.

The kelp production overall showed an increase trend with densities. The increment is not uniform for each box. For Box 2, when 80,000 kelp were cultured per ha, the production increased to 6.39 ton/ha against 5.23 ton/ ha with half seeding density at 40,000/ ha, and the increase rate is 22.2%. The same operation in Box 3 lead to a 32.7% production increase from 6.63 ton/ha to 8.80 ton/ha, and for Box 4, this lead to a 43.8% increase from 7.2 ton/ha to 10.36 ton/ha.

3.4. DIN budget

The contribution of oyster, kelp, phytoplankton, and the current exchange to the DIN content in Box 3 for scenario III is illustrated in Fig. 11. The amount from each contributor is computed from the ecosystem model equation listed in Table 1 and then summed up for each month.

Fig. 11 shows that the kelp aquaculture plays a vital role in the simulated DIN budget cycle for Box 3. When the oyster is in the appropriate environment with exuberant physiological activties, the DIN excretion from oyster peaked in September at 16.5 mgN/(m^3 month). As the temperature decreases and phytoplankton biomass drops, the DIN output of oyster decreases to a negeligible level around 0.33 mgN/(m^3 month), and it starts to rise again when the environment becomes suitable. Similar behavior for DIN absorption is also presented for the phytoplankton, with a peak uptake in August at 43.6 mgN/(m^3 month), and decreases as the water cools later on. The DIN concentration diffference between adjacent boxes determines the DIN budget, which is induced by the water exchange. Before the kelp seeding, Box 3 can be a pool that export DIN to other boxes with lower DIN content. After the kelp aquaculture starts and the biomass increases rapidly, the imported DIN is taken up by the cultured kelp, and the amount increases like exponentially from December to June. Kelp is also aquacultured in Box 2 and Box 4, indicating that the additional DIN mainly comes from outside the bay. In June, the monthly uptake of DIN by kelp exceeds 0.5 g/m^3, suggesting that the cultured kelp absorbs a considerable amount of nutrients from adjacent seas.

4. Discussion

An ecosystem model, which consists of the individual-based models for Pacific oyster *C. gigas* and kelp *S. japonica*, has been implemented based on previous literature (Pouvrou et al., 2006; Ren et al., 2008; Wu et al., 2009; Ren et al., 2012; Zhang et al., 2016; Cai et al., 2018). The individual model were validated by observations and the results agree reasonably well. The simulated DIN and phytoplankton reproduced the observed values in magnitude and seasonal cycle. The model performed well for describing the ecosystem with aquaculture being a significant component, and can be used to study different aquaculture scenarios.

4.1. Performance of the ecosystem model

Ecosystem models are practical tools to study the dynamics and characteristics of a particular ecosystem, shown in several applications (Grant et al., 2007; Shi et al., 2011; Filgueira et al., 2014). Reid et al. (2018) reviewed the various models and their performance testing method for IMTA in open waters.Furthermore, they stated that the assessment of nutrient transfer and growth in IMTA systems requires careful consideration for many aspects, including environmental conditions, ecological transfer efficiencies, and timing of production cycles.

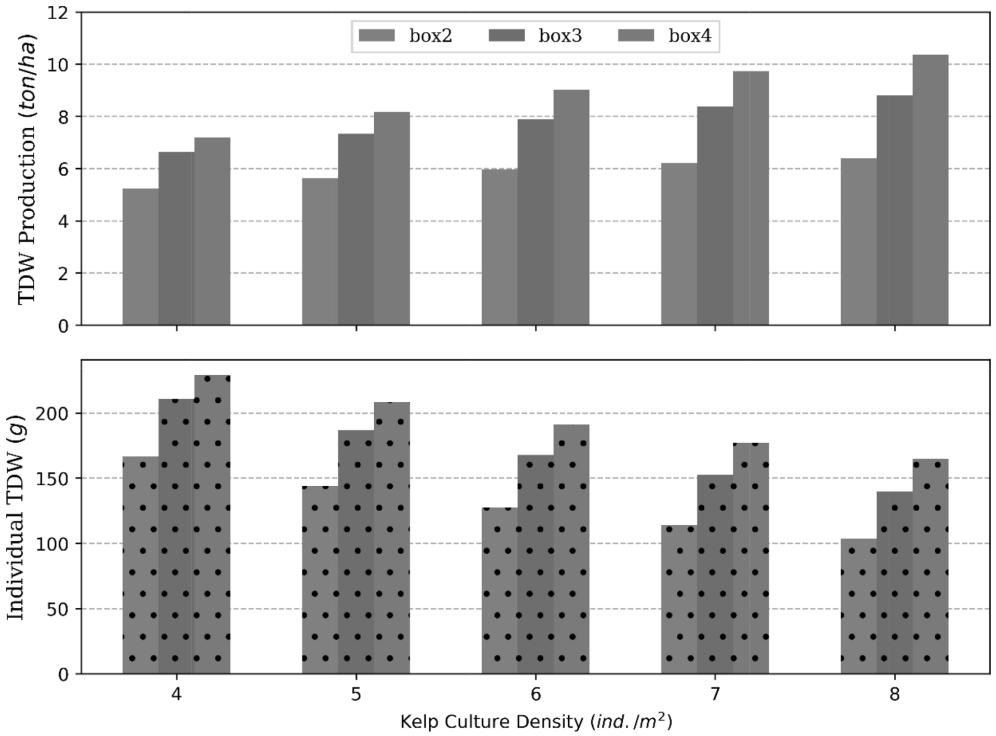

Fig. 10. Upper panel: the kelp harvest production in each box for different seeding densities. Lower panel: the individual TDW of kelp (with dots) when harvested in each box for different seeding densities.

We have used hourly hydrodynamic model results for the computation of the water exchange between each box. The tidal induced short-term environmental variation is introduced to the ecosystem model, and the enhanced temporal resolution helps to reconstruct the dynamic environment. Still, there are necessary assumptions on the physiological process, population dynamics, and environmental-organism interactions during the model operation, so the validation of model results to synchronous and systematical observations are required to optimize model performance. For our case, the spatial scale of the ecosystem model is tens of kilometers with complicated aquaculture activities. As there are numbers of aquaculture companies and self -employed households, the distribution of facilities and aquaculture management lacks uniformity. Due to the difficulties in obtaining synchronized observations, the accurate reproduction of past facts is extremely difficult.

The ecosystem model results for the seasonal phytoplankton and DIN (Fig. 5 and Fig. 6) have reproduced the general cycle and eligible magnitude from observations. This indicates the model's critical biological processes are sufficiently describing the major ecosystem characteristics. The phytoplankton biomass was underestimated during winter. An explanation is that temperature restriction omits low-temperature tolerant species, resulting in an extremely low phytoplankton reproduction during winter seasons. It is also possible that the observations were made near the outer boundary (Fig. 1), where the outer boundary condition does not capture the winter phytoplankton abundance in the Yellow Sea. The discrepancy of simulated DIN and phytoplankton probably resulted from a robust outer boundary constraint or the averaged spatial data. The model's assumptions may be insufficient to interpret the complicated natural variability.

Individual models are essential components of the ecosystem model, and reasonably parameterization of the physiological process of cultured organisms under different environmental conditions is of vital importance for the overall performance of the ecosystem model. The individual model we applied for oyster is implemented with the dynamic energy budget (DEB) theory (Kooijman, 2010), and the DEB model is apply well for bivalve (Duarte et al., 2003; Pouvreau et al., 2006; Ren et al., 2008). Indeed, the validation results (Fig. 3) prove that the model correctly described the growth of oysters in a given environment. The deviation between the observed and modeled oyster growth can be aroused from uncertainties in the environmental forcing.

The dynamic growth model for kelp was based on an exponential growth formula (Gregor et al., 2018), which requires a careful selection of parameters such as the basic daily growth rate. There are recent publications on the modeling of kelp in Sanggou Bay with different daily growth rates (Zhang et al., 2016; Cai et al., 2018). In our model, the daily growth rate was calibrated from the observations and set to be $\mu_{max} = 0.115$ / day. Different model parameterization for the specific species and region may be due to differences in the mathematical expressions, environmental data quality, or the sample quality. Pertinent environmental data with good quality (temporal and spatial) is required for further coupling of useful models for production prediction (Gregor et al., 2018). The individual kelp growth model showed good agreement with the observations in the given period, but whether it is sufficiently representative for Sanggou Bay still requires more data for validation and optimization.

4.2. Aquaculture management with the ecosystem model

Using the ecosystem model as a tool, we can investigate the carrying capacity of the cultured organism for each model box within Sanggou Bay. Currently, there are no unified criteria on how to define the carrying capacity for a specific environment. Filgueira et al. (2014)

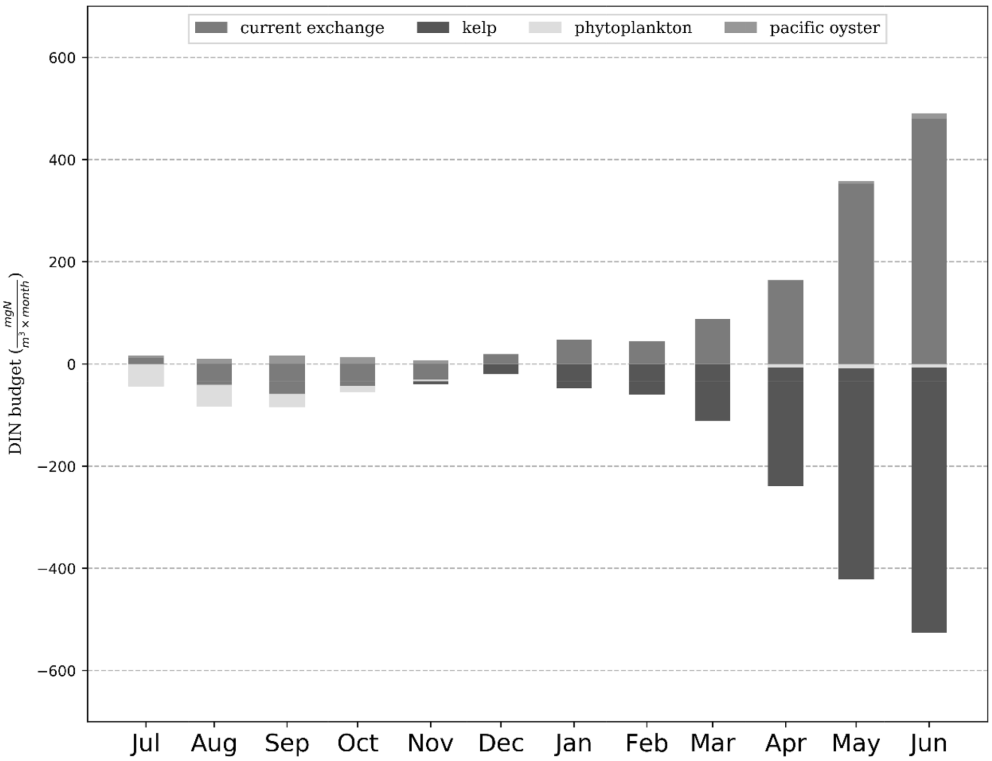

Fig. 11. The monthly DIN budget per m^3 computed for Box 3 under scenario III for current exchange, kelp absorption, phytoplankton absorption and oyster excretion.

implemented a fully spatial ecosystem model in Richibucto Estuary for oyster *Crassostrea virginica* aquaculture and used the phytoplankton depletion as an indicator for carrying capacity. Zhao et al. (2019) implemented a coupled SCAMOD for the bottom cultured scallop *Patinopecten yessoensis* and estimated the carrying capacity based on the economic benefit evaluation. For Pacific oyster aquaculture in Sanggou Bay (Fig. 8), the simulated production per ha increase as seeding density increases, indicating a higher available physical carrying capacity. The phytoplankton depletion increased proportionally with the oyster biomass growth, illustrating an enhanced transfer from phytoplankton biomass to the oyster. Equally, less cultured oyster leads to a higher production efficiency during the simulation period as individual oyster occupies more resource. For the practical aquaculture, there is a requirement for harvest size at the end of the year. The ecosystem model provides predictions for oyster growth and offers options for appropriate culture densities. Around 50 oysters cultured per m^2 based on the practical experience is close to the optimal solution under the current condition.

Kelp is the main seaweed cultured in Sanggou Bay, and the growth and culture carrying capacity are different from that of the oyster. From the kelp simulation scenarios, the kelp biomass increases slightly for each culture density in Box 2, indicating that the kelp biomass is getting close to the carrying capacity limited by the nutrient supply since May. In Box 3 and Box 4, the kelp production maintained a certain growth with increased culture numbers, with abundant DIN, and the increment is much higher with doubled kelp seed density. These results indicate there is still allowance to the carrying capacity. Nevertheless, under fixed mortality, increased kelp numbers in the aquaculture farms will lead to smaller individual sizes. When kelp grows to a certain extent, the effect of respiration, and erosion increases, and it starts to produce spores. Such a process, which is not fully resolved in the model, will affect the kelp quality. In actual aquaculture production, the limitation of kelp production is not only from physiological and ecological processes but also from the limitation of the physical living space. The current kelp aquaculture around 40,000 ind./ha based on decades of accumulated experience, is a balanced choice of production, individual quality, moderate management efforts, and less seed cost. The model results of predicted kelp growth and production could help farmers in make decisions based on environmental conditions, market demand, and policy requirements.

4.3. Model limitations and future improvements

Although our model followed the observations to a reasonable extent, it is based on a relatively crude spatial scale at tens of kilometers and several assumptions and simplifications. The model application requires uniform aquaculture layout covering a typical surface more than tens of kilometer square, which makes Sanggou Bay an ideal site due to its homogeneous and dense aquaculture distribution. A fully spatial-coupled ecosystem model (e.g., Filgueira et al., 2014) will better reproduce the spatial distribution and the impact of scattered aquaculture layout. However, such a model usually requires more stringent boundary conditions and validation data, and the model configuration is often specific to a localization and less general. It is reasonable to choose a more effective simulation method based on actual aquaculture and environment conditions.

The lack of synchronized and continuous observations during the ecosystem model simulation periods hinders the further calibration and

optimization of the model. However, to obtain continuous data is not easy, as this depends significantly on the sampling difficulty, measurement accuracy, and local aquaculture production processes. Sustaining data acquisition and continuous monitoring are required for model optimization. The improvement of the individual models relies on the progress of the physiological and ecological research describing the process of nutrient absorption kinetics, filter-feeding dynamics, and population dynamics.

5. Conclusion

The Sanggou Bay provides an excellent site to apply model study on the ecosystem controlled by commercial-scale aquaculture. The present ecosystem model generally reproduced seasonal variation of the dissolved inorganic nitrogen and phytoplankton concentrations. The predicted oyster and kelp growth validated well with observations. Scenario simulations showed that 50 cultured oysters per meter square is the optimal choice which comply with the current practical aquaculture. The model also concluded that the nutrient source for the kelp aquaculture in the bay was mainly from the adjacent sea. Moreover, in the region with inadequate nutrient supply, the kelp production was approaching the carrying capacity. The model can be a useful tool for integrated aquaculture management and spatial planning.

CRediT authorship contribution statement

L.I.N. Fan: Conceptualization, Methodology, Visualization, Writing - original draft, Writing - review & editing. **D.U. Meirong:** Investigation. **L.I.U. Hui:** Funding acquisition. **F.A.N.G. Jianguang:** Supervision. **ASPLIN Lars:** Writing - review & editing. **J.I.A.N.G. Zengjie:** Project administration, Investigation, Writing - review & editing.

Declaration of Competing Interest

The authors declare that they have no known competing financial interests or personal relationships that could have appeared to influence the work reported in this paper.

Acknowledgements

The authors would like to thank the two anonymous reviewers for their valuable suggestions. We appreciate Dr. XUAN Jiliang for providing the hydrodynamic and water quality model results. We thank Xunshan Co, Ltd. and Chudao Aquatic Food Co, Ltd. for help in the organism sampling and environmental monitoring. This study is supported by the Key Programme for International Cooperation on Scientific and Technological Innovation, Ministry of Science and Technology (2017YFE0118300), the Marine S&T Fund of Shandong Province for QNLM (No. 2018SDKJ0502), the Youth Talent Program from Laboratory for Marine Fisheries Science and Food Production Processes, QNLM(2018-MFS-T13), Modern Agro-industry Technology Research System (CARS-49) and Central Public-interest Scientific Institution Basal Research Fund, CAFS (NO. 2020TD50). This paper is also supported by the Environment and Aquaculture Governance project (MFA, CHN 2152) and the Horizon 2020 IMPAQT project (774109).

References

Bleck, R., 2002. An oceanic general circulation model framed in hybrid isopycnic-Cartesian coordinates Ocean. Model 4, 55–88. https://doi.org/10.1016/S1463-5003(01)00012-9.

Cai, B., Zhu, C., Liu, H., Chang, L., Xiao, L., Sun, Q., Lin, F., 2018. Model Simulated growth of kelp Saccharina japonica in Sanggou Bay. Progress in Fishery Science 40 (3). https://doi.org/10.19663/j.issn2095-9869.20180419001. in Chinese with English abstract.

Cao, L., Wang, W., Yang, Y., Yang, C., Yuan, Z., Xiong, S., Diana, J, 2007. Environmental impact of aquaculture and countermeasures to aquaculture pollution in China. Environmental Science and Pollution Research-International 14 (7), 452–462. https://doi.org/10.1065/espr2007.05.426.

Caperon, J., Meyer, J., 1972. Nitrogen-limited growth of marine phytoplankton—I. changes in population characteristics with steady-state growth rate. Deep Sea Research and Oceanographic Abstracts 19 (9), 601–618. https://doi.org/10.1016/0011-7471(72)90089-7.

Chen, C., Beardsley, R.C., Cowles, G., 2006. An unstructured grid, finite-volume coastal ocean model (FVCOM) system. Oceanography 19 (1), 78–89. https://doi.org/10.5670/oceanog.2006.92.

Chopin, T., Buschmann, A., Halling, C., Troell, M., Kautsky, N., Neori, A., Kraemer, G., Zertuche-González, J., Yarish, C., Neefus, C, 2001. Integrating Seaweeds into Marine Aquaculture Systems: a Key toward Sustainbility. J. Phycol. 37 (6), 975–986. https://doi.org/10.1046/j.1529-8817.2001.01137.x.

Duarte, P., Meneses, R., Hawkins, A., Zhu, M., Fang, J., Grant, J, 2003. Mathematical modelling to assess the carrying capacity for multi-species culture within coastal waters. Ecol Modell 168 (1–2). https://doi.org/10.1016/s0304-3800(03)00205-9. 109 143.

Egbert, G.D., Erofeeva, S.Y, 2002. Efficient inverse modeling of barotropic ocean tides. J. Atmos. Ocean. Tech. https://doi.org/10.1175/1520-0426(2002)019-3C0183:EIMOBO-3E2.0.CO;2. 19183–204.

EPA (Environmental Protection Agency, USA). Rates, constants, and kinetics. Formulations in surface water quality modeling: 2nd Edition, 1985:455.

FAO (2018). Fishery and Aquaculture Statistics 2016/FAO annuaire. Statistiques des pêches et de l'aquaculture 2016/ FAO anuario. Estadísticas de pesca y acuicultura 2016. Rome/Roma. 104pp.

Fang, J.-G., Sun, H.-L., Kuang, S.-H., 1996. Assessing the carrying capacity of Sanggou Bay for culture of kelp Laminaria japonica. Marine Fisheries Research 17, 7–17 in Chinese with English abstract.

Ferreira, J.G., Hawkins, A.J.S., Bricker, S.B, 2007. Management of productivity, environmental effects and profitability of shellfish aquaculture—The Farm Aquaculture Resource Management (FARM) model. Aquaculture 264 (1–4), 160–174. https://doi.org/10.1016/j.aquaculture.2006.12.017. Get rights and content.

Filgueira, R., Grant, J., Strand, Ø, 2014. Implementation of marine spatial planning in shellfish aquaculture management: modeling studies in a Norwegian fjord. Ecological Applications 24 (4), 832–843. https://doi.org/10.1890/13-0479.1.

Filgueira, R., Guyondet, T., Bacher, C., Comeau, L, 2015. Informing Marine Spatial Planning (MSP) with numerical modelling: a case-study on shellfish aquaculture in Malpeque Bay. (Eastern Canada) Marine Pollution Bulletin 100 (1), 200–216. https://doi.org/10.1016/j.marpolbul.2015.08.048.

Galparsoro, I., Murillas, Pinarbasi, A., Sequeira, K., Stelzenmüller, A.M., Borja, V., Á., Gimpel, A., 2020. Global stakeholder vision for ecosystem-based marine aquaculture expansion from coastal to offshore areas. Reviews in Aquaculture. https://doi.org/10.1111/raq.12422.

Grant, J., Bacher, C., 2001. A numerical model of flow modification induced by suspended aquaculture in a Chinese bay Canadian. Journal of Fisheries and Aquatic Sciences 58 (5), 1003–1011. https://doi.org/10.1139/f01-027.

Grant, J., Curran, K., Guyondet, T., Tita, G., Bacher, C., Koutitonsky, V., Dowd, M, 2007. A box model of carrying capacity for suspended mussel aquaculture in Lagune de la Grande-Entrée, Iles-de-la-Madeleine. Québec Ecological Modelling 200 (1–2), 193–206. https://doi.org/10.1016/j.ecolmodel.2006.07.026.

Guyondet, T., Roy, S., Koutitonsky, V., Grant, J., Tita, G, 2010. Integrating multiple spatial scales in the carrying capacity assessment of a coastal ecosystem for bivalve aquaculture. J. Sea Res. 64 (3), 341–359. https://doi.org/10.1016/j.seares.2010.05.003.

Holling, C.S., July 1959. **Some characteristics of simple types of predation and parasitism**. Can. Entomol. 91 (7), 385–398. https://doi.org/10.4039/Ent91385-7.

Jihong, J.H., Hansen, P.K., Fang, J.G., Wang, W., Jiang, Z.J., 2009. Assessment of the local environmental impact of intensive marine shellfish and seaweed farming—Application of the MOM system in the Sungo Bay. China Aquaculture 287 (3–4). https://doi.org/10.1016/j.aquaculture.2008.10.008. Issues.

Mao, Y.Z., Li, J.Q., Xue, S.Y., Lin, F., Jiang, Z.J., Fang, J.G., Tang, Q.S., 2018. Ecological functions of the kelp Saccharina japonicain integrated multi-trophic aquaculture, Sanggou Bay. China Acta Ecologica Sinica 38 (9), 1–8. https://doi.org/10.5846/stxb201703160444.

Milewski, I., 2001. Impacts of salmon aquaculture on the coastal environment: a review. In: Tlusty, MF, Bengston, DA, Halvorson, HO, Oktay, SD, Pearce, JB, Rheault JrRB (Eds.), Marine Aquaculture and the environment: A meeting For Stakeholders in the Northeast. Cape Cod Press, Falmouth, MA, pp. 166–197.

NACA. 1989. Integrated Fish Farming in China. NACA Technical Manual 7. A World Food Day Publication of the Network of Aquaculture Centres in Asia and the Pacific, Bangkok, Thailand. 278 pp.

Pouvreau, S., Bourles, Y., Lefebvre, S., Gangnery, A., Alunno-Bruscia, M, 2006. Application of a dynamic energy budget model to the Pacific oyster, Crassostrea gigas, reared under various environmental conditions. J. Sea Res. 56 (2), 156–167. https://doi.org/10.1016/j.seares.2006.03.007.

Radach, G., Moll, A, 1993. Estimation of the variability of production by simulating annual cycles of phytoplankton in the central North Sea. Prog. Oceanog 31, 339–419. https://doi.org/10.1016/0079-6611(93)90001-T.

Reid, G., Lefebvre, S., Filgueira, R., Robinson, S., Broch, O., Dumas, A., Chopin, T, 2018. Performance measures and models for open-water integrated multi-trophic aquaculture. Reviews in Aquaculture 293 (357). https://doi.org/10.1111/raq.12304. 211 30.

Ren, J., Stenton-Dozey, J., Plew, D., Fang, J., Gall, M, 2012. An ecosystem model for optimising production in integrated multitrophic aquaculture systems. Ecol Modell

246, 34–46. https://doi.org/10.1016/j.ecolmodel.2012.07.020.
Ren, J., Schiel, D., 2008. A dynamic energy budget model: parameterisation and application to the Pacific oyster Crassostrea gigas in New Zealand waters. J. Exp. Mar. Biol. Ecol. 361 (1), 42–48. https://doi.org/10.1016/j.jembe.2008.04.012.
Kooijman, S.A.L.M., 2010. Dynamic Energy Budget Theory For Metabolic Organisation. Cambridge University Presshttps://doi.org/10.1017/CBO9780511805400.
Shi, J., Wei, H., Zhao, L., Yuan, Y., Fang, J., Zhang, J., 2011. A physical–biological coupled aquaculture model for a suspended aquaculture area of China. Aquaculture 318 (3–4), 412–424. https://doi.org/10.1016/j.aquaculture.2011.05.048.
Steele, J.H., 1962. ENVIRONMENTAL CONTROL OF PHOTOSYNTHESIS IN THE SEA. Limnol. Oceanogr. 7 (2), 137–150. https://doi.org/10.4319/lo.1962.7.2.0137.
Whitmarsh D., Palmieri M.G. (2008) Aquaculture in the Coastal Zone: pressures, Interactions and Externalities. In: Holmer M., Black K., Duarte C.M., Marbà N., Karakassis I. (eds) Aquaculture in the Ecosystem. Springer, Dordrecht 10.1007/978-1-4020-6810-2-8.
Wu, R.J., Zhang, X.L., Zhu, M.Y., Zheng, Y.F., 2009. A model for the growth of haidai (laminaria japonica) in aquaculture. Marine Science Bulletin 28 (2), 34–40 in Chinese with English abstract.
Xuan, J., He, Y., Zhou, F., Tang, C., Zheng, X., Liu, H., Yu, L., Chen, J., 2019. Aquaculture-induced boundary circulation and its impact on coastal frontal circulation. Environmental Research Communications 1 (5), 051001. https://doi.org/10.1088/2515-7620/ab22cd.
Zhang, J., Wu, W., Ren, J., Lin, F, 2016. A model for the growth of mariculture kelp Saccharina japonica in Sanggou Bay. China Aquaculture Environment Interactions 8, 273–283. https://doi.org/10.3354/aei00171.
Zhao, J., Zhou, S.L., Fang, J.G., 1996. Research on Sanggou Bay aquaculture hydro-environment. Mar. Fish. Res 17, 68–79 in Chinese with English abstract.
Zhao, Y., Zhang, J., Lin, F., Ren, J., Sun, K., Liu, Y., Wu, W., Wang, W., 2019. An ecosystem model for estimating shellfish production carrying capacity in bottom culture systems. Ecol Modell 393, 1–11. https://doi.org/10.1016/j.ecolmodel.2018.12.005. Aquat. Living Resour. 16 1 2003.

Graphic design: Communication Division, UiB / Print: Skipnes Kommunikasjon AS

uib.no

ISBN: 9788230854723 (print)
9788230857274 (PDF)